ABSTRACT

Title of dissertation: RESPONSE OF THE COASTAL OCEAN AND ESTUARIES TO TROPICAL CYCLONES

Fan Zhang, Doctor of Philosophy, 2018

Dissertation directed by: Professor Ming Li

Marine Estuarine and Environmental Sciences Program

Landfalling tropical cyclones (TC) pose great threats to public safety. The recent decades have witnessed major advances of knowledge in TC dynamics and improvement in TC forecast models, however, occasionally inaccurate TC intensity and storm surge predictions remain a vital concern. Different representations of subgrid-scale physics by various atmospheric model parameterization schemes lead to uncertainty in predictions of TC's intensity and associated surges. In a case study for Hurricane Arthur (2014), local closure scheme for planetary boundary layer turbulence produces lower equivalent potential temperature than non-local closure schemes, leading to under-predicted TC intensity and surge heights. On the other hand, higher-class cloud microphysics schemes over-predict TC intensity and surge heights. Without cumulus parameterization for coarse-resolution grids, both TC intensity and surge heights are grossly under-predicted due to large precipitation decreases in the storm center. To avoid widespread predictions, the ensemble mean approach is shown to be effective. Another source of TC forecast error is inaccurate sea surface temperature (SST) prediction, and accurate SST prediction

necessitates a better understanding of mixing processes in the coastal ocean. Previously, the importance of TC-induced near-inertial currents (NICs) to mixing in the coastal ocean was overlooked. With high-frequency radar and autonomous glider, long-lasting NICs with amplitudes of ~0.4 m s^{-1} were observed on the shelf during Arthur. With an atmosphere-ocean model, we find the NICs were dominated by mode-1 vertical structure and were a major contributor to the shear spectrum. Therefore, NICs may be important in producing turbulent mixing and surface cooling during Arthur's passage. In the future, with warmer SST, sea level rise, and possible hard shorelines in estuaries, increased storm surge hazard is expected. Using Isabel (2003) as a case study, we find storm intensification under 2100 SST raises surge heights in Chesapeake Bay by 0.1-0.4 m given increased energy input. While sea level rise in 2100 reduces surge heights by 0-0.15 m through non-linear processes, it increases total water level by 0.4-1 m. Moreover, hard shoreline further increases surge heights by up to 0.5 m in the middle and upper Chesapeake Bay by prohibiting energy flux towards wetlands.

RESPONSE OF THE COASTAL OCEAN AND ESTUARIES TO TROPICAL CYCLONES

by

Fan Zhang

Dissertation submitted to the Faculty of the Graduate School of the
University of Maryland, College Park in partial fulfillment
of the requirements for the degree of
Doctor of Philosophy
2018

Advisory Committee:

Professor Ming Li, Chair
Professor William C. Boicourt
Professor Da-Lin Zhang
Professor Shenn-Yu Chao
Professor Greg Silsbe

ACKNOWLEDGEMENTS

I cannot express my gratitude enough to my advisor, Ming Li, for his guidance and support throughout my Ph.D. study in Horn Point Laboratory. When I lost in the details with frustration, discussions with Ming were always insightful and inspiring. As a junior, I struggled a lot on my first paper in terms of writing. Ming guided me through that hard time period with lots of patience and significant efforts. I am also very fortunate to have a committee that includes Da-Lin Zhang, Bill Boicourt, Shenn-Yu Chao, and Greg Silsbe. Da-Lin was always ready to answer my questions about hurricane dynamics and helped me a lot on Chapter 3. Bill and Shenn-Yu always gave me constructive suggestions during committee meetings and kept me on the right track. Greg was always there when I need help with my research and daily life. I would also like to thank Xiaohui Xie, my lab mate and an expert on internal waves. Discussions with Xiaohui were always delightful and helped pave the way for the near inertial wave study in Chapter 2. Finally, I would like to thank the students, faculty, and staff of Horn Point Laboratory, who made my graduate life a wonderful experience.

TABLE OF CONTENTS

LIST OF TABLES

Chapter 2

Chapter 4

Appendix A

LIST OF FIGURES

Chapter 2

Chapter 4

Appendix A

CHAPTER 1

INTRODUCTION

Coastal oceans and estuaries around the world harbor many densely populated metropolitan cities and support substantial economic activities. Landfalling tropical cyclones can generate strong currents and storm surges in the coastal oceans and estuaries, posing great threats to public safety and economy. Tropical cyclones are non-frontal synoptic scale low-pressure systems with organized convection and definite cyclonic surface wind circulations. These tropical cyclones generally form over tropical water. Sea surface temperature (SST) over 26.5^{o}C, weaker vertical wind shear, and higher relative humidity in the mid-atmosphere can facilitate their developments (e.g., Holland 1997). After they move poleward to higher latitudes, with a favorable synoptic scale steering force, they turn landward, march over the coastal ocean and finally hit an estuary or an open coast. Even though, only 1/5 of tropical cyclones make landfall as hurricanes (Woodruff 2013), coastal impacts by storms are largely due to this small subset of tropical cyclones.

1.1 Storm surge induced by tropical cyclones

Most damages related to tropical cyclones are caused by storm surge. Based on momentum equation, storm surge height is proportional to the pressure deficit and wind stress of tropical cyclones. While in an air-sea coupled context, on the atmospheric side, storm surge is sensitive to the track, intensity, radius of maximum wind and translation speed of tropical cyclones (Zhong et al. 2010; Weisberg and Zheng 2006; Irish et al. 2008; Rego and Li 2009); on the ocean side, it is sensitive to the geometry of coast and estuary, surface wave stress and bottom friction (Beardsley et al. 2013; Kerr et al. 2013).

To minimize the potential damage from surges, accurate forecasts for storm surges are required. One-way coupled air-sea model is widely used for regional storm surge forecast. In this regime, atmospheric model downscales synoptic features from global model and is then ran in a higher resolution to better capture important fine-scale tropical cyclone dynamics. The ocean model is driven by the wind stress and sea surface pressure from the atmospheric model. Since storm surge is mainly controlled by barotropic processes, it is relatively easy for an ocean model to capture the essential hydrodynamics. In contrast, the atmospheric modeling of the tropical cyclone dynamics is more challenging and is an active area of research. For example, parameterizations for sub-grid scale physical processes (planetary boundary layer dynamics, hydrometer phase changes, etc.), which play important roles in tropical cyclone development, are needed. Numerous schemes have been developed for each of these processes. As a result, tropical cyclone prediction can have significant divergences in intensities and tracks because of different choices of parameterization schemes. While a large body of literature has explored the sensitivity of tropical cyclone prediction to sub-grid parameterization schemes, few has examined the sensitivity of storm surge prediction to parameterization schemes in meso-scale atmospheric models.

1.2 Near inertial currents induced by tropical cyclones

As the primary energy source for tropical cyclones is the enthalpy flux from ocean surface to the atmosphere. A good understanding of the mixing process in the upper ocean during tropical cyclones, which affect SST, is essential for accurate tropical cyclone prediction. When tropical cyclones are in the open ocean, the forced stage response of the

upper ocean is characterized by rightward-biased mixed-layer currents. This asymmetry arises due to wind stress vectors of tropical cyclone rotate anticyclonic on the right side of the track and are parallel with near inertial currents (NICs; Price et al. 1994). These NICs are induced by the Rossby adjustment process of the surface mixed layer in response to the injected potential vorticity from cyclonic wind stresses (Gill 1984). In fact, most of the energy in this process goes into NICs and up to 2/3 of mixed layer kinetic energy is at near inertial frequencies in the power spectrum (Pollard 1980). These storm-induced NICs in the open ocean have been widely discussed in the literature (e.g., Pollard 1980; Price 1981; Shay and Elsberry 1987; Shay and Elsberry 1989; Shay et al. 1998). Generally, they are highly intermittently in both space and time; the horizontal scale can be up to hundreds of kilometers, albeit the strongest response is typically found just below the storm track.

These storm-induced NICs can persist for several days, while the horizontal and vertical scale decrease with time after storm has passed. This decay of local mixed-layer NICs energy is due to the combination of equatorward horizontal energy flux, downward vertical energy flux towards deeper ocean, and dissipation within the mixed layer.

D'Asaro et al. (1995) found the equatorward propagation of low-mode near inertial wave is responsible for the reduced depth-integrated near inertial energy in the mixed layer, based on a two-dimensional (2D) nearly inviscid, nonlinear layer model. Mooers (1975) introduced an effective Corilolis frequency concept, which was further elucidated by Kunze (1985), that near inertial wave frequency f_{eff} is modified by the local mean flow vorticity ζ: $f_{eff}=f+\zeta/2$. Therefore, negative mean flow vorticity can trap NICs energy and

affect the horizontal near inertial wave energy propagation. For example, Jamies and Shay (2010) found that the NICs energy induced by Hurricane Katrina and Rita was trapped by anticyclonic eddies related to Loop Current.

The vertical group velocity of near inertial wave is substantially smaller than horizontal group velocity. Price (1983) reported a 0.12 cm/s vertical group velocity near Hurricane Eloise's track, based on an inviscid, multi-layered model. Brooks (1983) estimated the vertical group velocity to be 0.07 cm/s during Hurricane Allen, based on observations. The horizontal group velocity is typically 2 or 3 orders of magnitudes larger (Price 1983; Brooks 1983; Shay and Elsberry 1987). Therefore, NICs are mostly surface intensified and the energy lost to the deeper ocean is relatively small.

As NICs energy propagates downward, their phase propagates upward. This phase difference within the mixed-layer can generate strong vertical shear and induce significant mixing. Based on cruise data, Cuypers et al. (2013) found that the total dissipation rate is 8 times larger with NICs-induced shear than without it. Therefore, a large proportion of NICs energy eventually contributes to turbulent mixing within the mixed-layer. Zhai et al. (2009) estimated that 70% of wind-induced NICs energy is dissipated in the surface layer using a realistic $1/12^{o}$ model of the north Atlantic Ocean. Cuypers et al. (2013) found only 10% of the tropical cyclone wind power input reaches the thermocline, indicative of strong dissipation within the mixed layer.

In addition, cold water from the deeper ocean can also penetrate into the mixed-layer due to NICs-induced shear. This mechanism accounts for most of the surface mixed-layer cooling and deepening during storm passage (Price 1981). The colder SST can reduce the enthalpy flux from ocean surface to tropical cyclones and provide negative feedbacks to storms and potentially reduce their intensities.

When tropical cyclones are closer to the coast, they can continue generating NICs on the shelf. These NICs share a lot of commonalities with those in the open ocean. However, due to the existence of coastal boundary, they possess some distinct characteristics. The most striking feature of shelf NICs is that they have opposite phases between surface and bottom layers, with a zero-crossing in the mid-column (Pettigrew 1981; Millot 1981; Shearman 2005; Mackinnon and Gregg 2005). This phase difference is due to an offshore barotropic wave excited by divergence at the coastal boundary (Millot 1981; Shearman 2005). This vertical structure of shelf NICs implies strong shear and shear-induced mixing which can cause surface cooling during storm passage and affect storm intensity during landfall stage. This has been barely discussed in the literature and needs further study.

1.3 Impact of climate change on storm surge

If we look into the future, storm surges can be worse under climate change, due to storm intensification over warmer ocean and sea level rise. Lowe et al. (2001) and Lowe and Gregory (2005) downscaled a global atmospheric model to a regional one; then they used the latter to force a hydrodynamic model of the UK shelf seas from pre-industrial era

to 2100. The global atmospheric model used greenhouse gas concentrations based on the Intergovernmental Panel on Climate Change (IPCC) Special Report on Emissions Scenarios (SRES) A2 and B2 emissions scenarios for the period from 1990 to 2100. In addition, global sea level rise estimated from the coupled global model was added to the hydrodynamic part. They found an increase in the present day 1%-occurrence flood level in the North Sea to a 50%-occurrence flood level by the end of the century. However, limited by computational power, in order to capture century-scale evolution of surges, they have to sacrifice the spatial resolutions in the models. The 50 km resolution regional atmospheric model was not sufficiently to resolve fine scale tropical cyclone dynamics, and 35 km resolution hydrodynamic model could barely capture estuary scale shoreline changes due to sea level rise.

By contrast, Mousavi et al. (2011) used a fine resolution hydrodynamic model (up to 70m in the channels) to study the impacts of sea level rise and warmer SST to surges at Corpus Christi Bay, Texas. They found the flood elevation can raise by up to 1.8 m during catastrophic-type hurricane surge events. To consider the impact of future warmer SST on storm intensity, they assumed linear decrease in tropical cyclone central pressure with SST increase, then fitted the higher intensity into a parametric wind model (Holland 1980) and used it to drive the hydrodynamic model. Nevertheless, this rather simple parametric wind approach is not convincing in resolving storm dynamics under climate change, as the SST–intensity empirical relationship was developed based on current climate and may fail in the future, considering changing mid-level humidity and upper-level wind shear with climate change. Therefore, to understand the impact of climate change on storm surges in the

estuary, a high resolution atmospheric model, which considers storm dynamics more comprehensively than a parametric one, and a high resolution hydrodynamic model, which can capture fine scale shoreline changes, are needed.

Moreover, in such study, the estuary-scale regional sea level rise should be accounted in the model instead of global sea level rise. Global sea level rise is mainly controlled by thermal expansion of seawater, melting of glaciers and polar ice caps, and ice loss from Greenland and Antarctica (Church et al. 2013). Regional sea level rise is more complicated. For example, in Southern Mid-Atlantic-Bight, at least three more factors can further enhance sea level rise in this region: the land subsidence associated with glacial isostatic adjustment (Engelhart et al. 2011; Miller et al. 2013); the weakening of the Gulf Stream (Ezer et al. 2013; Kopp 2013), and the weakening of the Atlantic Meridional Overturning Current (Yin et al. 2010; Yin and Goddard 2013; Rahmstorf et al. 2015).

Motivated by these gaps, we seek to better understand the response of the coastal ocean and estuaries to tropical cyclones. This dissertation is organized as follows: sensitivity analyses of storm surge simulations to atmospheric model parameterization schemes and model configurations is presented in Chapter 2, followed by study of NICs induced by tropical cyclones in the coastal ocean in Chapter 3; Chapter 4 investigates the impact of climate change on storm surge in the estuary; and the final chapter concludes.

CHAPTER 2

SENSITIVITY ANALYSIS OF STORM SURGE FORECASTS TO WRF PHYSICS PARAMETERIZATIONS AND MODEL CONFIGURATIONS

Preface

This chapter is a reproduction of work published in Weather and Forecasting with coauthors Ming Li, Andrew C. Ross, Serena Blyth Lee, and Da-Lin Zhang. The right to reuse this work was retained by the authors when publication rights and nonexclusive copyright were granted to the American Meteorological Society.

Zhang, F., M. Li, A. C. Ross, S. B. Lee, and D.-L. Zhang, (2017): Sensitivity Analysis of Hurricane Arthur (2014) Storm Surge Forecasts to WRF Physics Parameterizations and Model Configurations. Weather and Forecasting, 32(5), 1745-1764.

2.1 Introduction

Storm surge represents a major threat to coastal communities. Many efforts have been devoted to predicting storm surge. In a recent Coastal and Ocean Modeling Testbed (COMT) project, Kerr et al. (2013a) found that unstructured-grid coastal models Advanced Circulation (ADCIRC) model (Luettich et al. 1992), Finite Volume Community Ocean Model (FVCOM, Chen et al. 2003), and Semi-implicit Eulerian Lagrangian Finite Element (SELFE) model (Zhang and Baptista 2008) had better predictive skill than the official National Oceanic and Atmospheric Administration (NOAA)'s operational model SLOSH (Sea, Lake, and Overland Surges from Hurricanes), when used to hindcast storm surges generated by Hurricane Ike (2008) and Rita (2005) in the Gulf of Mexico. A parallel study by Chen et al. (2013) showed that the same three unstructured-grid models achieved similar skill to each other in hindcasting storm surges generated by extratropical storms when the same mesh, meteorological forcing, and initial/boundary conditions were used. These modeling studies typically focused on improving the hydrodynamic model prediction of tides, storm surge and waves. For example, Kerr et al. (2013b) found that the storm surge generated by Ike was sensitive to the bottom friction parameterization, especially in shelf waters where a strong shore-parallel coastal current was a key to the storm's geostrophic setup. In order to obtain accurate predictions of surge water levels overland and in inland waters, Bunya et al. (2010) and Dietrich et al. (2010) employed a spatially varying bottom friction coefficient to account for different types of land surfaces such as salt marshes. Furthermore, studies by Chen et al. (2013) and Beardsley et al. (2013) showed that wave-current interactions could change the direction of storm-induced currents and increase

onshore water transport and overland inundation even though they only had moderate effects on the peak surge height.

Storm surge prediction has also been shown to be sensitive to atmospheric forcing (Peng et al. 2004; Weisberg and Zheng 2006; Irish et al. 2008; Rego and Li 2009). Earlier studies used idealized wind models such as parametric surface winds that assume an idealized stationary, symmetric cyclone (Peng et al. 2004), or the planetary boundary layer (PBL) hurricane wind model (Scheffner and Fitzpatrick 1997). In a numerical study of storm surges in the Albemarle-Pamlico Sound for 10 hypothetical hurricanes, Peng et al. (2004) showed that the storm surge was sensitive to both the minimum sea-level pressure (MSLP) and the radius of maximum wind (RMW). Using a high-resolution FVCOM model of Tampa Bay, Florida, Weisberg and Zheng (2006) found that the storm surge height was highly dependent on the storm's track, intensity and forward propagation speed. Later, Irish et al. (2008) underlined the importance of the storm size, and showed that the peak surge height over mild sloping coastal regions could vary by 30% for a reasonable range of the storm size. In another study, Rego and Li (2009) noted the importance of the hurricane forward speed in storm surge prediction and found that resonance amplified the peak surge when the hurricane's forward speed was comparable to the shallow-water wave propagation speed. However, neither the parametric surface wind model nor the PBL wind model could capture mesoscale wind structures in hurricanes and provide realistic wind fields needed to predict storm surge along complex coastlines. Therefore, sensitivity analyses using the idealized hurricane models are of limited value for improving the storm

surge forecast for a specific storm, even though their computational efficiency makes them well suited for producing flood hazard maps in coastal areas.

To obtain accurate storm surge predictions, realistic meteorological forcing fields are needed to drive the hydrodynamic models. NOAA Hurricane Research Division used to generate real-time hurricane winds (H*WIND) from surface wind observations on buoys, automated observation platforms, ships, etc. (Powell et al. 1998), but the H*WIND winds were only available prior to landfall. Consequently, surface wind and air pressure predictions from mesoscale atmospheric models such as the fifth-generation Pennsylvania State University-National Center for Atmospheric Research mesoscale model (MM5) and Weather Research and Forecasting model (WRF) have been used to drive the storm surge models (Lin et al. 2010; Zhong et al. 2010; Di Liberto et al. 2011; Chen et al. 2013; Georgas et al. 2014; Wang et al. 2014; Zambon et al. 2014). Most of these models were run in hindcast mode. Typically, the meteorological forecast that provided the best storm surge prediction was used to drive the hydrodynamic model. Given the large number of parameterization schemes used in the mesoscale atmospheric models, however, it is not clear which parameterization schemes should be used when making forecasts for storm surge. Moreover, little is known how uncertainties in the atmospheric model prediction affect the hydrodynamic model prediction of storm surge.

The WRF model has emerged as a preferred mesoscale atmospheric model for hurricane prediction (e.g., Liu et al. 1997; Davis et al. 2008; Li and Pu 2008; Nolan et al. 2009a, b; Lin et al. 2010; Zambon et al. 2014). Many of the important physical processes

in tropical cyclones, however, cannot be resolved in WRF and must be parameterized. On the smallest scales, these include the transfer of heat, moisture, and momentum at the air–sea interface, and the microphysics of cloud formation and precipitation. Several schemes have been developed to calculate the surface fluxes and vertical mixing within the PBL, including the classic Mellor-Yamada scheme (Mellor and Yamada 1982; Janjic 1994) and non-local schemes (Zhang and Anthes 1982; Hong et al. 2006; Hong and Kim 2008). Each PBL scheme includes a surface layer scheme which parameterizes the momentum, moisture, and heat fluxes within the lowest 10% of the PBL (e.g., Pleim 2006; Jimenez et al. 2012). Various cloud microphysics (CM) schemes are used to simulate hydrometeor phase changes, differing in their complexity and hydrometeor species (Hong et al. 2004; Hong and Lim 2006). Braun and Tao (2000) found pronounced sensitivities of high-resolution intensity simulations of Hurricane Bob (1991) to four different PBL schemes. Nolan et al. (2009a, b) investigated how PBL schemes affected the prediction of Hurricane Isabel (2003)'s intensity and forward propagation speed, and suggested the modifications that significantly improved the intensity prediction. Using a diagnostic tropical cyclone PBL model, Kepert (2012) tested a number of PBL schemes and found that Louis and Mellor-Yamada schemes performed best. Li and Pu (2008) showed that numerical simulations of the early intensification of Hurricane Emily (2005) were very sensitive to the choice of CM and PBL schemes. Similarly, Zhu and Zhang (2006a) highlighted the possible sensitivity of inner-core structures to changes in CM. Other studies have shown that hurricane prediction is sensitive to the configurations of initial and boundary conditions in WRF (e.g., Davis et al. 2008; Lin et al. 2010). Kilic and Raible (2013) showed that hurricane tracks and intensities were affected by mesoscale differences in the sea

surface temperature (SST) used as the WRF bottom boundary condition. Recently, Glenn et al. (2016) and Seroka et al. (2016) demonstrated that resolving spatiotemporal changes in SST was the key to avoid the intensity over-prediction for Hurricane Irene (2011) over the Mid-Atlantic Bight. Glenn et al. (2016) further showed that ahead-of-eye-center cooling in the coastal ocean was an important factor influencing the intensity of landfalling hurricanes and tropical storms.

Most of the previous sensitivity analyses focused on the effects of physics parameterizations on hurricane simulation in the atmosphere (Kepert 2012; Zhu et al. 2014; Zhu and Zhu 2015; Zhang et al. 2015; Zhang and Marks 2015; Penny et al. 2016). Little research has been done to investigate how storm surge prediction depends on the physics parameterizations in the mesoscale atmospheric model. It remains unclear how uncertainties in the atmospheric model forecast propagate to the ocean model and produce uncertainties in the storm surge forecast. In this study we use an atmosphere-ocean model to conduct sensitivity analyses of the storm surge prediction. By running experiments with different physics parameterizations and different configurations of the initial and boundary conditions in the regional atmospheric model, we will examine how they affect the storm surge prediction. Hurricane Arthur, which made landfall in North Carolina as a Category 2 hurricane on 4 July 2014, is selected for this case study. Arthur produced substantial flooding in North Carolina and other Mid-Atlantic states. Before Arthur's landfall, a multi-institutional team of researchers from Woods Hole Oceanographic Institution, Rutgers University, University of Maryland Center for Environmental Science, University of Maine and Gulf of Maine Research Institute deployed an array of storm gliders and storm

data buoys in the Mid-Atlantic Bight, in order to investigate the impact of the shelf condition on the storm intensity. This paper is part of that larger group effort to evaluate the storm surge prediction for Hurricane Arthur.

This paper is organized as follows. Section 2 describes the regional atmosphere and ocean models as well as the design of the sensitivity analyses experiments. Section 3 presents the storm surge prediction from the control model run. Section 4 shows the sensitivity analyses of storm surge prediction to physics parameterizations in WRF, and Section 5 shows the sensitivity analyses of storm surge prediction to initial and boundary conditions in WRF. Section 6 presents discussion and conclusion.

2.2 Description of atmosphere-ocean models and numerical experiment

To predict the storm surge generated by Hurricane Arthur, we use the Advanced Research WRF model version 3.8 (Skamarock et al. 2008) to simulate the hurricane dynamics in the atmosphere, and FVCOM to simulate the oceanic response to the hurricane forcing. In this atmosphere-ocean model system, hourly outputs of surface wind and air pressure fields from WRF are used to force FVCOM.

We have configured triple-nested model domains for WRF (Figure 2.1a). The outermost domain has a coarse resolution of 12 km, and covers the western Atlantic such that WRF simulates most of the storm's life cycle, starting from its initial formation off southeastern Florida to its eventual transition to an extratropical storm off the Gulf of Maine. The middle domain covers the south and middle Atlantic regions at a resolution of

4 km. The innermost domain uses a fine resolution of 1.33 km to resolve the region most affected by the storm surge, extending from the Outer Banks, North Carolina to Chesapeake Bay, Virginia-Maryland. WRF hourly outputs of surface wind and air pressure from all the three domains are used to force FVCOM, but the analysis of storm dynamics is based on the results from WRF's outermost domain. After testing 35, 40, and 50 vertical sigma levels in WRF, 40-levels was chosen because it had the best agreement with the National Hurricane Center (NHC) best track storm intensity. At the lateral boundaries of its outermost domain, WRF is forced by the 0.5° Global Forecast System (GFS) products (http://www.emc.ncep.noaa.gov/GFS/.php) issued at 1900 LST 1 July with updates at 3-hour intervals for the 5-day forecast period (i.e. a single cycle). At the ocean surface, WRF is forced by outputs from 0.5° real-time global SST (http://polar.ncep.noaa.gov/sst/) at 1-day intervals. GFS is used to initialize WRF at 1900 LST 1 July 2014, approximately 48 hours prior to Arthur's landfall at the Outer Banks, North Carolina. This provides sufficient time for Hurricane Arthur to spin up from its initial vortex state downscaled from GFS.

FVCOM is used to configure a coupled estuary-shelf model that includes Albemarle-Pamlico Sound, Chesapeake Bay, Delaware Bay and the eastern U.S. continental shelf (Figure 2.1b). The eastern boundary is placed several hundred kilometers from the coast while the southern and northern boundaries are roughly perpendicular to the coast, located at 34°N and 41°N, respectively. The horizontal resolution ranges from ~1 km in the inner shelf to ~10 km near the open boundaries. Three sub-model domains extending from the western boundary resolve Albemarle-Pamlico Sound, Chesapeake Bay and Delaware Bay at a resolution of 0.2-1.0 km. The model is run in a two-dimensional

barotropic mode in which temperature and salinity are kept constant. At the offshore open boundary, the sea level is prescribed using ten tidal constituents according to the Oregon State University global tidal model TOPEX/POSEIDON (TPXO) 7.1 (Egbert and Erofeeva 2002). River discharges in the upper tributaries of the two estuaries are prescribed using data from U.S. Geological Survey water gauge stations. A quadratic stress is exerted at the bed, with the drag coefficient calculated from a spatially-uniform Manning coefficient of 0.02 (Arcement and Schneider 1989). FVCOM is hot-started at 1900 LST 1 July 2014 from a hindcast simulation that began from 0000 LST 1 May 2014, in order to allow tides to ramp up before the arrival of Hurricane Arthur and produce sufficiently long sea level time series that can be used for the tidal harmonic analysis later.

A series of numerical experiments has been conducted to investigate how the physics parameterizations and model configurations in WRF affect the storm surge prediction. Table 2.1 lists the physics parameterization schemes and initial and boundary condition configurations in the control run. The sensitivity analysis runs explore three PBL schemes, four CM parameterizations, three options of CPs, five SST products, and three different large-scale atmospheric forecasting products for prescribing the initial and lateral boundary conditions of WRF (Table 2.2). In each sensitivity analysis run, only one parameterization scheme or one model configuration is changed from the control run while everything else remains unchanged. No changes are made to the FVCOM configuration.

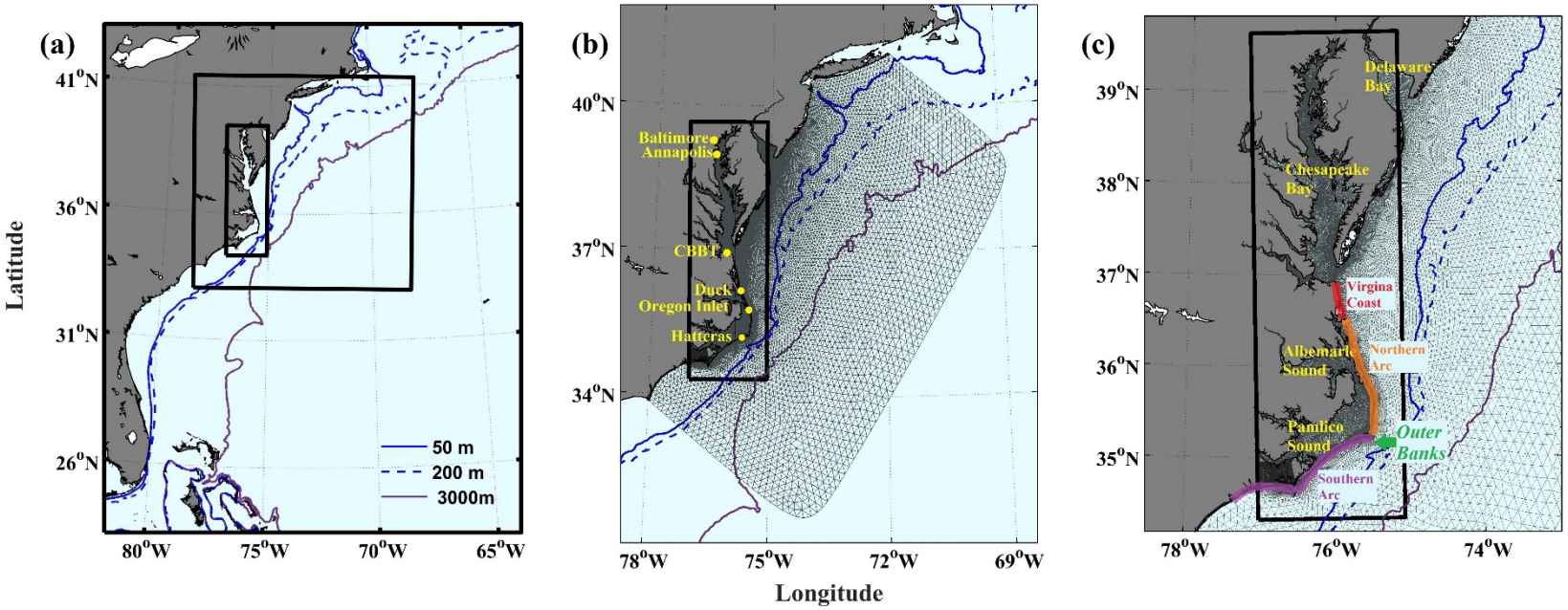

Figure 2.1 (a) WRF's triple-nested domains (thick black rectangles) at resolutions of 12, 4 and 1.33 km. (b) FVCOM's model domain covering the eastern U.S. continental shelf and adjacent estuaries. Yellow dots mark the tidal stations used for the model-data comparison. (c) Map of the study area showing geographical locations such as Albemarle-Pamlico Sound, Outer Banks, Chesapeake Bay and Delaware Bay. The contours represent isobaths at depths of 50, 200 and 3000 m. The outer limits in (b) give a subdomain of the WRF 4 km domain. The thick black rectangles in (b) and (c) indicate the WRF 1.33 km domain.

Table 2.1 The WRF physics parameterization schemes and the initial and boundary conditions selected for the control run.

Model Configuration	**Option**
Grid resolution	12 km – 4 km – 1.33 km
Vertical levels	40 levels
PBL (planetary boundary layer)	Yonsei-University scheme
CM (cloud microphysics)	WRF single-moment 3 class scheme
Longwave radiation	Rapid radiative transfer model
Shortwave radiation	Dudhia scheme
CP (cumulus parameterization)	Kain-Fritsch scheme for 12 km domain only
Initial/lateral boundary condition	Global Forecast System 0.5° product
SST (sea surface temperature)	Real-time global SST low resolution
Land physics scheme	Unified Noah land-surface model

Table 2.2 A list of sensitivity-analysis numerical experiments for different physics parameterizations and different configurations of the initial and boundary conditions for the WRF model.

Experiments	Option	Run Name	Option	Run Name
PBL	Yonsei-University scheme	PBL-YSU	Asymmetric Convective Model scheme	PBL-ACM2
	Mellor-Yamada-Janjic scheme	PBL-MYJ		
CM	WRF single-moment 3 class scheme	CM-WSM3	WRF single-moment 5 class scheme	CM-WSM5
	WRF single-moment 6 class scheme	CM-WSM6	WRF double-moment 6 class scheme	CM-WDM6
CP	On for 12 km domain and off for 4 km domain	CP-ON12_OFF4	Off for 12 km domain and off for 4 km domain	CP-OFF12_OFF4
	On for 12 km domain and on for 4 km domain	CP-ON12_ON4		
SST	Real-time global SST low resolution	SST-RTG_low	Skin temperature from Global Forecast System	SST-GFS
	Real-time global SST high resolution	SST-RTG_high	Hybrid Coordinate Ocean Model SST	SST-HYCOM
	Advanced very high resolution radiometer SST	SST-AVHRR		
IBC	Global Forecast System	IBC-GFS	North American Mesoscale model	IBC-NAM
	ERA-Interim	IBC-ERA		

2.3 Storm surge prediction

Results from the control run are presented and compared against the atmospheric and oceanic observations. The predicted track compares well to the best track provided by NHC (Figure 2.2a). Hurricane Arthur moved northeastward in the South Atlantic Bight on 2-3 July. It made landfall near Beaufort on the Outer Banks of North Carolina around 2200 LST 3 July, and exited Albemarle-Pamlico Sound several hours later. Arthur continued on its northeastward path over the Mid-Atlantic Bight on 4 July but moved at a much faster speed. WRF accurately predicts Arthur's track and forward propagation speed. The root-mean-square error (RMSE) between the predicted and observed tracks is 63.9 km, which is mainly due to a westward bias originating from the westward shift of the large-scale atmospheric circulation in GFS. Although the westward bias could affect the intensity prediction by increasing the time the storm spends over land, Figure 2.2b shows that the predicted MSLP closely matches the observation. The observed MSLP dropped from 995 mb on 2 July to about 970 mb on 4 July, indicating a rapid intensification of the storm intensity over this period. WRF essentially captures this intensification process. It also reproduces Arthur's subsequent weakening over the Mid-Atlantic Bight as it encountered colder water. Arthur attained a maximum sustained wind (MSW) of 45 m s^{-1} at 10 m above the sea surface. This is well simulated by WRF, although the predicted peak speed of MSW lags the observed peak wind by several hours (Figure 2.2b). The RMSE for MSLP and MSW are 4.7 mb and 4.8 m s^{-1}, respectively, while the correlation coefficients are 0.97 and 0.88.

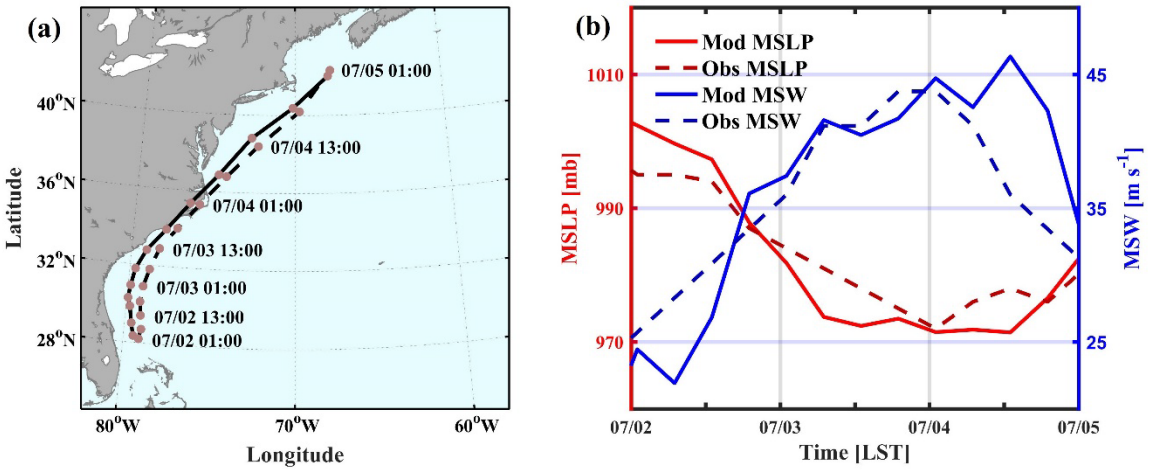

Figure 2.2 (a) A comparison between the predicted (solid) and observed (NHC best track, dashed) track of Hurricane Arthur (2014). Time stamps (in LST) are marked by solid dots on the tracks. (b) Time series of the predicted (solid) and observed (dashed) minimum sea level pressure (MSLP, blue lines) and maximum sustained winds (MSW, red lines) at 10 m height.

Additional model-data comparisons are made using the measurements of surface pressure and wind speed at six tidal stations (Figures 2.3a and 2.3b). These stations are selected because the Outer Banks of North Carolina and Virginia Coast encountered the highest storm surges whereas the mid-to-upper Chesapeake Bay experienced the largest sea level drop (Berg 2015). WRF generally captures the observed rapid drop of surface air pressure at Hatteras, Oregon Inlet, Duck and CBBT, although it over-predicts the air pressure drop at Duck and under-predicts the air pressure drops at Oregon Inlet and Hatteras. Since Hurricane Arthur's path cut through Albemarle-Pamlico Sound, winds blew northeastward at Hatteras and Oregon Inlet but southwestward at Duck and CBBT (Figure 2.3b). WRF reproduces this regional difference in the wind direction. Farther north in Chesapeake Bay (e.g., Baltimore and Annapolis), the surface air pressure slowly increased as Arthur moved away toward the northeast. The lower than observed pressure

at Baltimore and Annapolis, as well as the offsets in surface air pressure at Duck, Oregon Inlet, and Hatteras, are related to WRF's westward bias in the track prediction. Winds at the northern Chesapeake Bay locations primarily blew in the southward direction, and their magnitudes and directions are well predicted by WRF.

To examine how well WRF-FVCOM forecasts the storm surge generated by Hurricane Arthur, we compare the time series of the total and subtidal sea levels at the six tidal gauge stations (Figures 2.3c and 2.3d). Stations Hatteras and Oregon Inlet are located just inside the Pamlico Sound and have weak tides. Thus the storm surge dominated the sea level response at these sites. In contrast, sea level at Duck and CBBT included both tidal and storm surge components. The southward winds blowing down Chesapeake Bay drove water level down at Baltimore and Annapolis. FVCOM captures these diverse sea level responses. Figure 2.3d compares the predicted and observed storm surge after tidal signals are removed through harmonic analysis. Hurricane Arthur caused a storm surge of about 1.5 m at Oregon Inlet and a sea-level drop of 0.5 m at Baltimore. The RMSE averaged for the total and subtidal sea levels at the six tidal gauge stations are 0.15 m and 0.14 m, respectively, and the averaged correlation coefficients are 0.89 and 0.83.

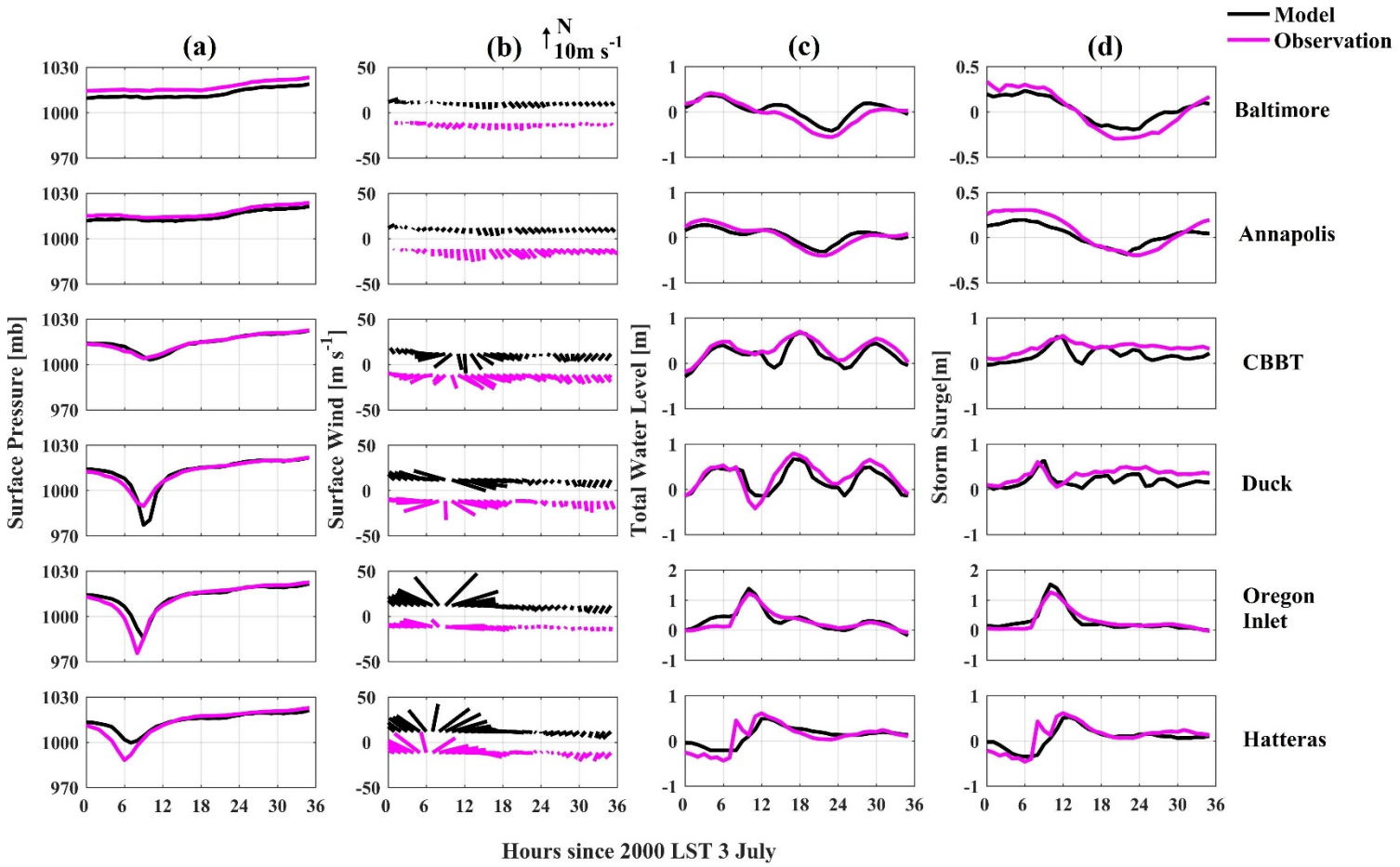

Figure 2.3 Time series of the predicted (black) and observed (magenta) (a) surface air pressure, (b) wind speed vector at 2-m height, the (c) total and (d) subtidal water level at six tidal gauge stations whose locations are marked in Figure 3.1b.

2.4 Sensitivity of storm surge prediction to WRF physics parameterizations

Now we explore the sensitivity of the storm surge prediction to the physics parameterization schemes in WRF.

2.4.1 The planetary boundary layer

Three widely used PBL schemes in WRF are tested in this study: (i) the Yonsei University (YSU) scheme in Run PBL-YSU (i.e. the control run) (Hong et al. 2006); (ii) the Asymmetric Convective Model version 2 (ACM2) scheme in Run PBL-ACM2 (Pleim 2007); and (iii) the Mellor-Yamada-Janjic 1.5 order (MYJ) scheme in Run PBL-MYJ (Janjic 1994). MYJ is a local closure scheme. In contrast, YSU and ACM2 are non-local closure schemes. YSU parameterizes the non-local fluxes implicitly via a parameterized non-local term, while ACM2 treats the non-local fluxes explicitly.

The predicted storm tracks are very similar to each other among the three model runs, all exhibiting a slight westward bias from the observed track (Figure 2.4a). However, the predicted storm intensities are quite different. Runs PBL-YSU and PBL-ACM2 predict significantly lower values of MSLP on 3-4 July than Run PBL-MYJ (Figure 2.4b). Similarly, MSW reaches ~44 m s^{-1} at the peak intensity of the storm in Runs PBL-YSU and PBL-ACM2 versus ~36 m s^{-1} in Run PBL-MYJ (Figure 2.4c). MSLP in Run PBL-MYJ increases between 1200 LST and 2200 LST 3 July, indicating a weakening of the storm, whereas MSLP in the other two runs remains the same. To understand this intensity difference between Run PBL-YSU/PBL-ACM2 and Run PBL-MYJ, we calculate the equivalent potential temperature θ_e inside the PBL because the moist entropy flux was

previously shown to affect storm intensity (Malkus and Riehl 1960; Holland 1997). We choose a cross-section through the storm's center and average θ_e between 1200 LST and 2200 LST 3 July. The cross-section is chosen to be in the southwest-to-northeast direction to capture the left-right and the front-back asymmetries in the hurricane field. As shown in Figures 2.4d-f, θ_e in Run PBL-MYJ is about 4 K lower than that in the other two runs. This result is consistent with that of Zhang and Zheng (2004), who showed that the MYJ PBL scheme tends to produce colder PBL than that produced by the Blackadar (Zhang and Anthes 1982) and the Medium-Range Forecast (MRF; Hong and Pan 1996) PBL schemes, on which the ACM2 and the YSU PBL schemes are based, respectively. The colder PBL with the MYJ scheme may be attributed partly to less upward transfer of the net surface heat fluxes (Figure 2.4g), possibly through the paired Eta similarity surface layer scheme, and partly to the lack of countergradient heat fluxes from the capped inversion in the MYJ scheme (Zhang and Zheng 2004). Starting from late 4 July, a rapid weakening process was initiated in all three model runs as Arthur encountered colder SST at higher latitudes over the North Atlantic.

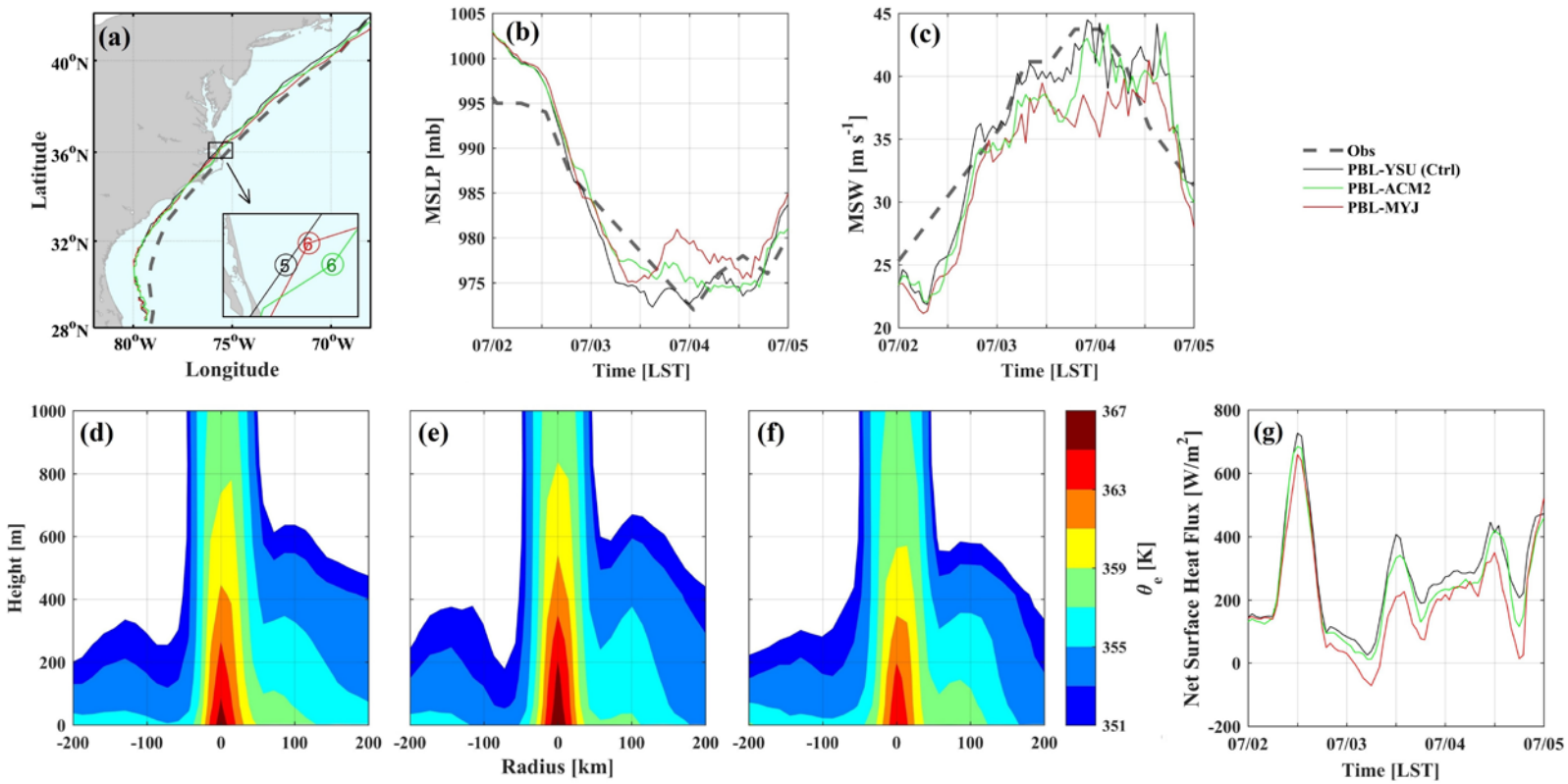

Figure 2.4 Sensitivity analysis of PBL (planetary boundary layer) parameterizations. (a) Storm track, (b) MSLP, and (c) MSW at 10 m height from Runs PBL-YSU (black), PBL-ACM2 (green), and PBL-MYJ (red). NHC best track data are marked as "Obs" (dashed). The insert in (a) shows a zoomed-in view of the storm track near the northern arc of the Outer Banks and the numbers mark hours on 4 July. Southwest to northeast cross-sectional distributions of the averaged equivalent potential temperature through the storm's center from Runs (d) PBL-YSU, (e) PBL-ACM2, and (f) PBL-MYJ. (g) The area-averaged net surface heat flux within 150 km radius of the storm center.

As a result of the intensity difference, the surge heights are different between the runs with the local and non-local PBL closure schemes. The storm surge predicted by Run PBL-ACM2 is similar to that in Run PBL-YSU and will not be discussed further. Figure 2.5 compares two snapshots of the wind field and non-tidal sea level distribution between Run PBL-YSU and Run PBL-MYJ. Due to a slight difference in the forward propagation speed, the storm position in Run PBL-MYJ lags behind that in Run PBL-YSU by about 1 hour (see the insert in Figure 2.4a). The snapshots in Figure 2.5 are taken when the storm simulated in the two model runs was at roughly the same geographic location rather than at an identical clock time. In the first snapshot taken around 0500 LST 4 July (Figures 2.5a,b,e,f), Hurricane Arthur had just moved out of Albemarle-Pamlico Sound through the northern arc of the Outer Banks. Run PBL-YSU predicts strong onshore winds ahead of the storm's center, thus producing high sea levels along the Virginia coast and its adjacent shelf (Figures 2.5a and 2.5b). The onshore winds predicted by Run PBL-MYJ are weaker and the resulting storm surges are weaker (Figures 2.5e and 2.5f). On the back of the storm, the winds and storm surge between the two model runs have relatively smaller differences than those ahead of the storm's center.

In the second snapshot taken around 1500 LST 4 July, Hurricane Arthur moved past 39°N, at the same latitude as the northern end of Chesapeake Bay (Figures 2.5c,d,g,h). The southward winds to the left of the storm drove water away from the upper part of the estuary. Large differences in the wind speed magnitude (up to 6 m s^{-1}) are found between Runs PBL-YSU and PBL-MYJ, particularly in the middle and lower parts of the estuary

(Figures 2.5c and 2.5g). This results in larger sea-level depression in the upper Chesapeake Bay in Run PBL-YSU than in Run PBL-MYJ (Figures 2.5d and 2.5h).

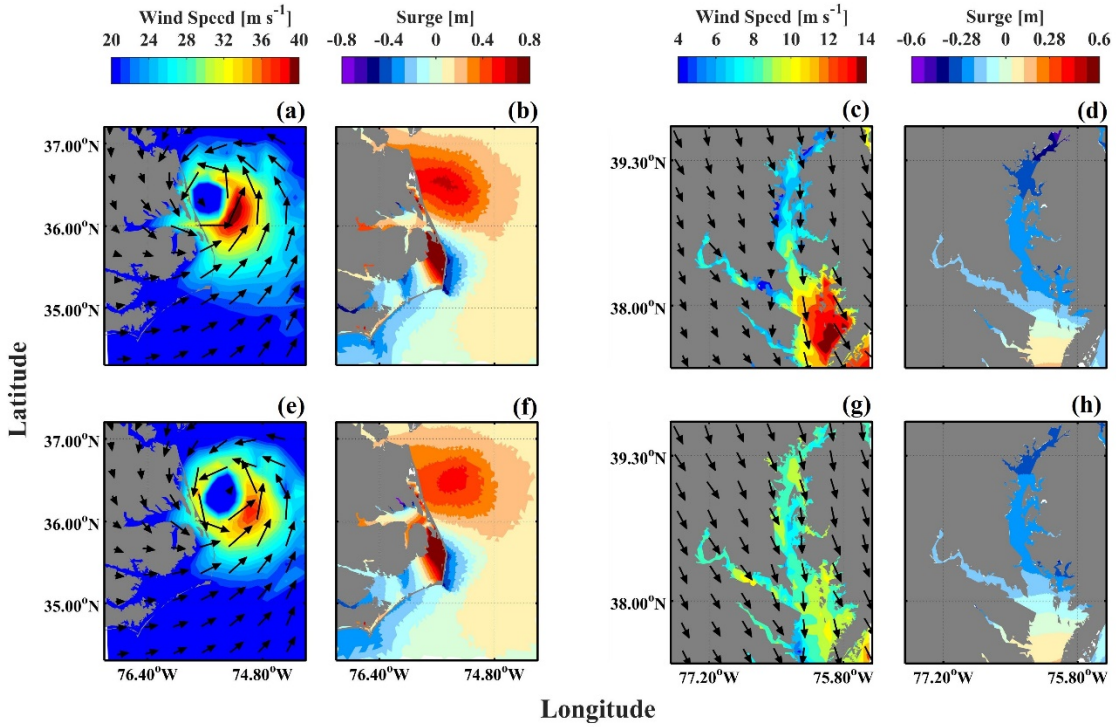

Figure 2.5 A comparison of wind speed and storm surge predictions between Runs PBL-YSU (top row) and PBL-MYJ (bottom row). (a)/(e) Wind speed magnitude (color) and vectors (arrow) and (b)/(f) subtidal sea level around the Outer Banks at 0500 LST 4 July (PBL-YSU) or 0600 LST 4 July (PBL-MYJ). (c)/(g) Wind speed (color) and vectors (arrow) and (d)/(h) subtidal sea level over Chesapeake Bay at 1500 LST 4 July (PBL-YSU) or 1600 LST 4 July (PBL-MYJ).

In WRF, the PBL schemes are paired with specific surface physics parameterizations. YSU and ACM2 are paired with the revised MM5 similarity surface layer scheme (Jimenez et al. 2012), while MYJ is paired with the Eta similarity surface layer scheme (Janjic 1996). It is possible that the surface layer parameterization may have contributed to the differences in the Arthur simulations between Runs PBL-YSU/PBL-ACM2 and PBL-MYJ. As a step towards discerning the effect of the surface physics parameterization, we explored two surface layer parameterization schemes in PBL-YSU: the revised MM5 similarity scheme and the old MM5 similarity scheme (Grell et al. 1994).

There were virtually no differences in storm track and MSLP between the two model runs. The differences in the storm surge heights were within a few cm.

2.4.2 Cloud microphysics

The four CM schemes used for the sensitivity analysis are WRF single-moment 3 class (WSM3) scheme in Run CM-WSM3 (i.e. the control run), WRF single-moment 5 class (WSM5) scheme in Run CM-WSM5, WRF single-moment 6 class (WSM6) scheme in Run CM-WSM6, and WRF double-moment 6 class (WDM6) scheme in Run CM-WDM6. WSM3 considers three categories of hydrometeors: vapor, cloud water/rain, and ice/snow. In WSM3, cloud water/rain turns into ice/snow instantly at 0°C, prohibiting the formation of super-cooled water (Hong et al. 2004). WSM5 is a mixed-phase scheme, including vapor, cloud water, rain, ice, and snow (Hong et al. 2004). WSM6 extends WSM5 by including graupel (Hong and Lim 2006). Both WSM5 and WSM6 account for the behavior of super-cooled water. In addition to predicting the mixing ratios of the six hydrometeors as in WSM6, WDM6 includes prognostic number concentrations of cloud, rain water, and cloud condensation nuclei (double moment) to improve the representation of warm-phase processes (Lim and Hong 2010).

All four CM sensitivity runs produce nearly identical storm tracks (not shown). Overall, the higher-class CM schemes produce a stronger hurricane, but the MSLP and MSW predicted by Run CM-WSM3 are in better agreement with the observations (Figures 2.6a and 2.6b). The minimum MSLP is 963 mb in Run CM-WSM6, 964 mb in Run CM-WSM5, 966 mb in Run CM-WDM6, and 974 mb in Run CM-WSM3 while the observed

minimum MSLP is 972 mb. The MSW is 45 m s^{-1} in Run CM-WSM3 versus 50 m s^{-1} in Run CM-WSM6, amounting to 11% difference. To understand what caused these different intensity predictions, we compare the cross-sectional distribution (in the southwest-to-northeast direction) of temperature anomaly among Runs CM-WSM3, CM-WSM5, CM-WSM6 and CM-WDM6 across the troposphere, up to 200 mb (Figures 2.6e-h). The temperature anomaly is calculated by removing the mean temperature at each pressure level and averaging between 1200 LST 2 July and 1200 LST 3 July. The warm core at the storm's center is located around 400 mb or roughly 7.5 km. It is smaller and colder in Run CM-WSM3 than in the other runs. The maximum temperature anomaly is 10 K in Runs CM-WSM5, CM-WSM6, and CM-WDM6, but less than 9 K in Run CM-WSM3. The 8 K anomaly contour extends from 600 to 200 mb in Runs CM-WSM5, CM-WSM6, and CM-WDM6, but is limited between 520 and 320 mb in Run CM-WSM3. The weak temperature anomaly is an indication that less latent heat is released in the storm simulated with the CM-WSM3 scheme (e.g. Li and Pu 2008). Due to its relatively simple representation of cloud physics, WSM3 predicts less precipitation, less snow production, and hence less latent heat release to fuel the storm. In contrast, the higher-class CM schemes (Runs CM-WSM5, CM-WSM6, and CM-WDM6) predict a much faster rate of intensification and a lower minimum value of MSLP (Figure 2.6a). Compared to Run CM-WSM6, Run CM-WDM6 has more realistic simulation of the storm intensity and MSW after 1200 LST 3 July. To understand this difference, we calculate the vertical distribution of the temperature anomaly through the storm's center and average it over two periods: one between 1200 LST 2 July and 1200 LST 3 July (before the lowest MSLP) and one between 1200 LST 3 July and 1200 LST 4 July (after the lowest MSLP). Although the temperature anomaly

predicted in Run CM-WDM6 is nearly the same as in Run CM-WSM6 during the former period (Figure 2.6c), it lies halfway between the temperature anomalies in Run CM-WSM6 and Run CM-WSM3 during the later period (Figure 2.6d). This explains why the MSLP and MSW predicted in Run CM-WDM6 are in better agreement with the observations than Run CM-WSM6 during the decelerating phase of the storm.

The over-prediction of the storm intensity in Run CM-WSM6 leads to the over-prediction of the storm surge (Figure 2.7). The storm surge produced in Run CM-WSM5 is the nearly the same to that in Run CM-WSM6 and not shown. At 0500 LST 4 July when Arthur just left Albemarle-Pamlico Sound through the northern arc of the Outer Banks, Run CM-WSM6 predicts a larger storm size and stronger winds than Run CM-WSM3 (Figures 2.7a and 2.7b). Compared to Run CM-WSM6, winds in Run CM-WDM6 are weaker, a result of the rapid weakening that started from 1200 LST 3 July. The winds in the southeast and northwest quadrants of the storm are up to 10 m s^{-1} stronger in Run CM-WSM6 than in Runs CM-WSM3 and CM-WDM6. Consequently, the storm surges at the Virginia Coast and northern Outer Banks are much higher in Run CM-WSM6 (Figures 2.7d-f). For example, the peak surge height at Duck, North Carolina is 0.65 m in Run CM-WSM3, 0.88 m in Run CM-WDM6 and 0.97 m in Run CM-WSM6 while the observed surge height was 0.61 m. Hence, Run CM-WSM6 over-predicts the surge height at Duck by ~60%. Inside Albemarle-Pamlico Sound and around the southern arc of the Outer Banks, the predicted sea level heights show smaller differences among the three model runs. The peak surge height at Oregon Inlet, North Carolina is 1.52 m in Run CM-WSM3, 1.48 m in Run CM-WDM6 and 1.68 m in Run CM-WSM6 while the observed surge height was 1.26 m.

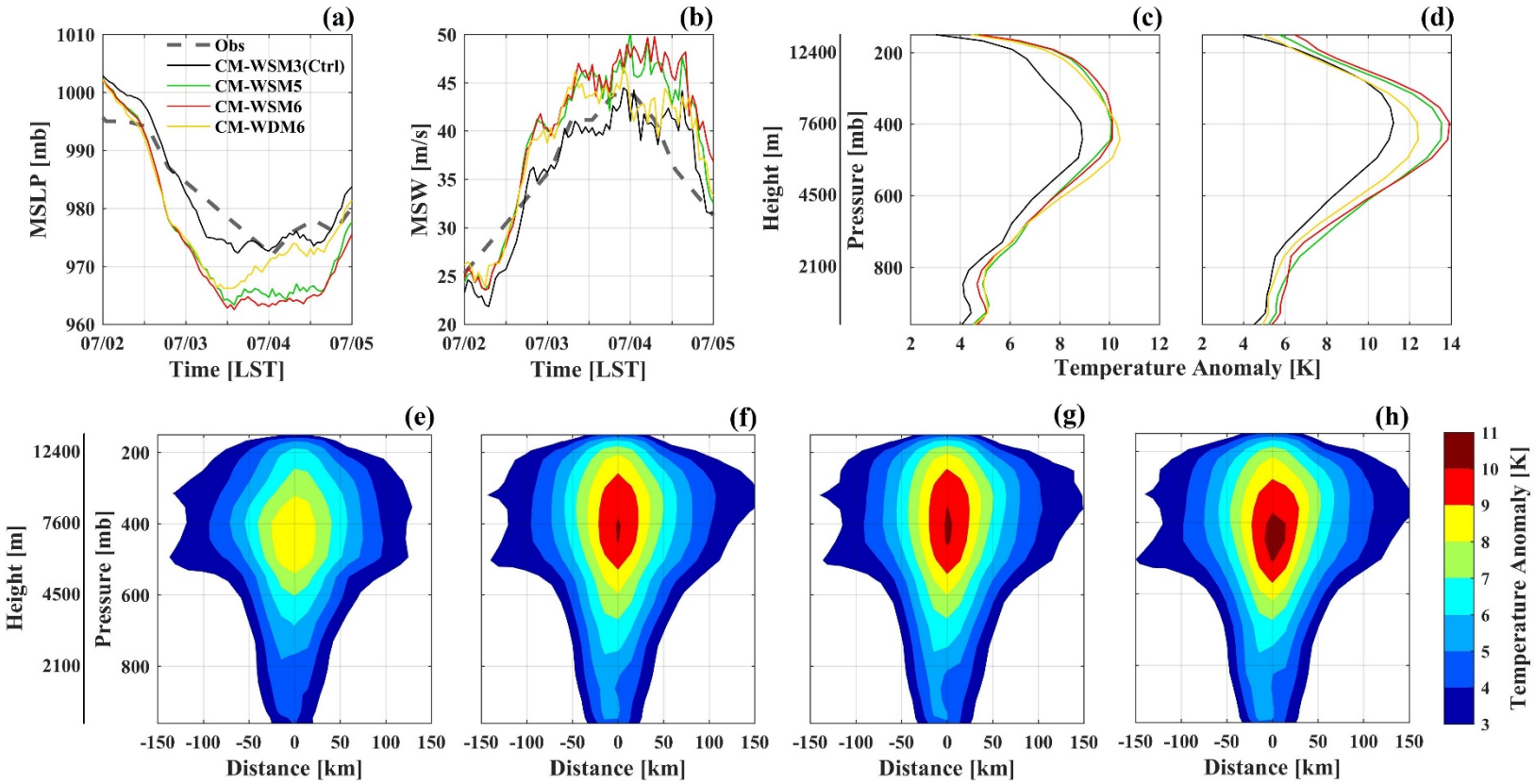

Figure 2.6 Sensitivity analysis of CM (cloud microphysics) parameterizations. (a) MSLP and (b) MSW at 10 m height from Runs CM-WSM3 (black), CM-WSM5 (green), CM-WSM6 (red), and CM-WDM6 (yellow). The black dashed lines represent the observations. The vertical distribution of temperature anomaly at the storm's center averaged over two periods: (c) 1200 LST 2 July to 1200 LST 3 July; (d) 1200 LST 3 July to 1200 4 July. Cross-sectional distributions of temperature anomaly through the storm center, averaged between 1200 LST 2 July and 1200 LST 3 July: (e) Runs CM-WSM3, (f) CM-WSM5, (g) CM-WSM6, and (h) CM-WDM6.

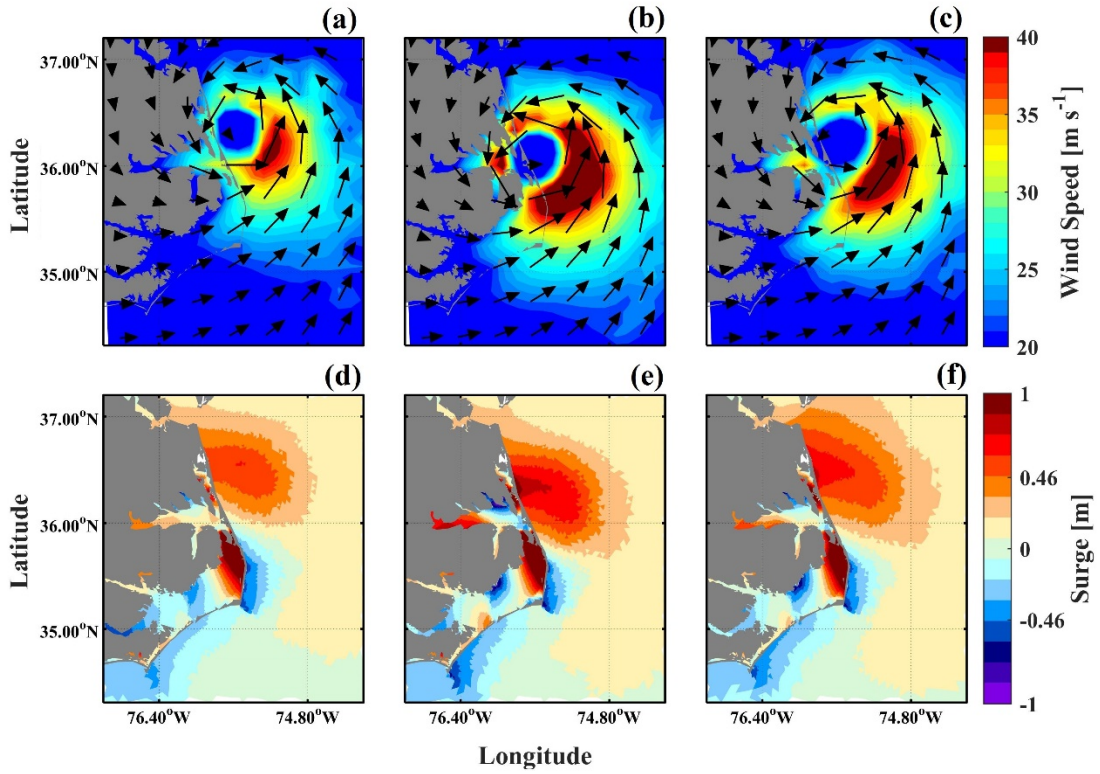

Figure 2.7 A comparison of (a-c) wind speed magnitude (color) and vectors (arrows) and (d-f) storm surge between Runs CM-WSM3 (left column), CM-WSM6 (mid-column), and CM-WDM6 (right column) around 0500 LST 4 July.

2.4.3 Cumulus parameterization

A cumulus parameterization scheme assumes the generation of sub-grid scale clouds that transport vertically heat and water vapor without requiring the presence of grid-box saturation (Zhang et al. 1988; Molinari and Dudek 1992). It is one of the key parameters controlling the storm intensification process, especially when grid spacing is several kilometers or larger (Smith 2000). In the control run (Run CP-ON12_OFF4), WRF employs the Kain-Fritsch CP scheme (Kain 2004) for the 12 km WRF domain because it assumes that the model is unable to resolve cumulus convection at this coarse spatial scale (Weisman et al. 1997), but CP is not activated in the 4 km WRF domain. To examine if CP affects the storm and storm surge prediction, we conduct two model runs: Run CP-

OFF12_OFF4 in which CP is turned off in all domains; Run CP-ON12-ON4 in which CP is turned on in both 12 km and 4 km WRF domains. No CP is applied to 1.33 km WRF domain in either of these runs.

All CP sensitivity analysis runs produce nearly identical storm tracks (not shown). Switching off CP in the 12 km domain results in a dramatic reduction in the storm intensity: the minimum MSLP increases from 972 to 990 mb while the maximum MSW decreases from 44 to 32 m s^{-1} (29% reduction) (Figures 2.8a and 2.8b). This large reduction in the storm intensity can be attributed to the decreased or delayed latent heat release associated with rainbands in the outer regions. Specifically, the activation of a CM scheme requires the presence of grid-box saturation. On the other hand, the Kain-Fritsch scheme would be activated in atmospheric columns where both conditional instability and reasonable upward lifting of the PBL are present (Kain 2004). Once activated, it would facilitate organized mass and moist convergence, leading to the formation of grid-box saturation and the activation of a CM scheme. In fact, the total precipitation within the 200 km radius of the storm center decreases by approximately 30% in Run CP-OFF12_OFF4 between 1200 LST 2 July and 1700 LST 4 July (Figure 2.8c). Suppressed latent heat release causes this significant reduction in precipitation as well as resulting storm intensity. On the other hand, switching on or off CP in the 4 km domain has a minor effect on the storm intensity (Figures 2.8a and 2.8b). The response of the storm surge to CP in the 12 km domain is strong, with the surge off the Virginia Coast and the Outer Banks significantly weakened in Run CP-OFF12_OFF4 (Figures 2.8d-f). At Duck, North Carolina, the peak surge height is 0.65 m in Run CP-ON12_OFF4 versus 0.45 m in Run CP-OFF12_OFF4, while at Oregon Inlet,

North Carolina, the peak surge height is 1.52 m in Run CP-ON12_OFF4 versus 1.31 m in Run CP-OFF12_OFF4. Hence, switching off CP in the 12 km WRF domain reduces the surge heights by 13%-31%. In contrast, the surge response to CP in the 4 km domain is weak, with the sea-level differences less than 0.02 m at the two sites.

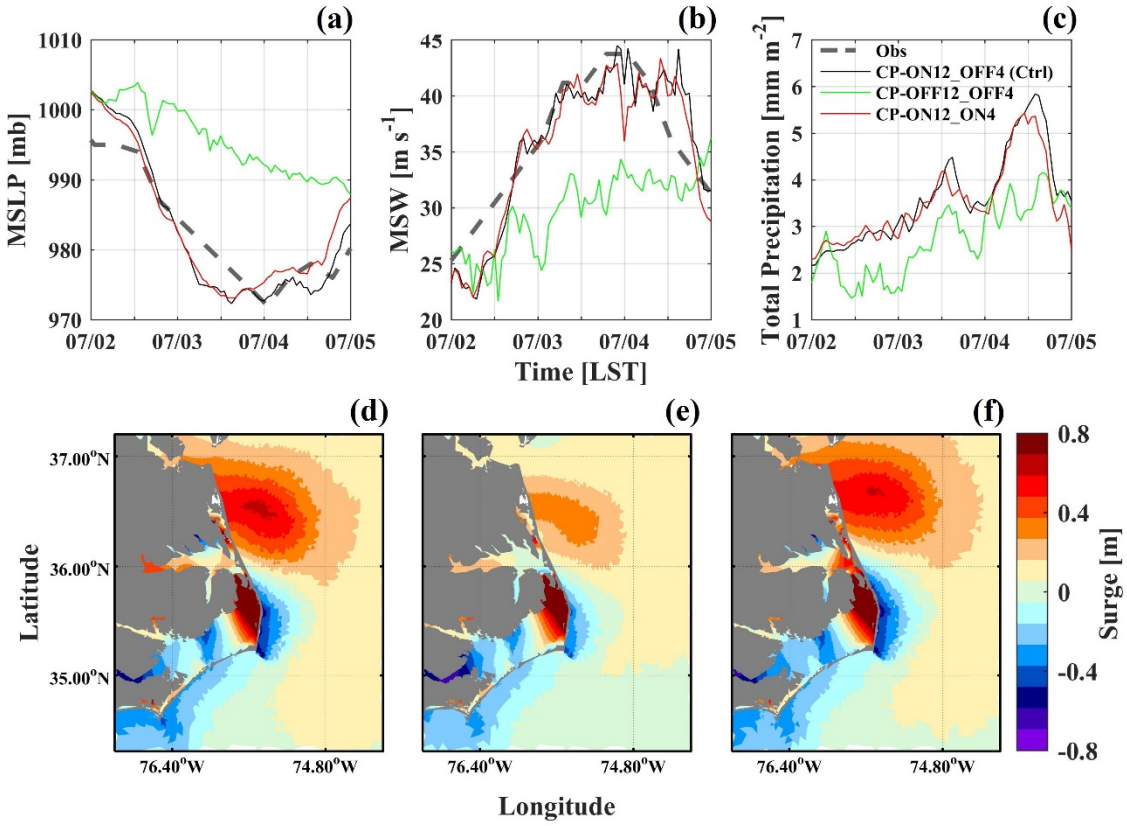

Figure 2.8 Sensitivity analysis of CP (cumulus parameterization). Time series of (a) MSLP, (b) MSW at 10 m height, and (c) the averaged total precipitation within 200 km radius of the storm center from Runs CP-ON12_OFF4 (black), CP-OFF12_OFF4 (green), and CP-ON12_ON4 (red). A comparison of storm surge between Runs (d) CP-ON12_OFF4, (e) CP-OFF12_OFF4, and (f) CP-ON12_ON4 at 0500 LST 4 July.

2.5 Sensitivity of storm surge prediction to WRF initial and boundary conditions

Next we explore if and to what extent the configurations of the initial and boundary conditions for WRF affect the storm surge prediction.

2.5.1 Sea Surface Temperature

Previous studies have highlighted the crucial roles of SST in determining the storm intensity (Emanuel 1999; Zhu and Zhang 2006b). Several SST products are routinely available and have been used to provide the oceanic boundary condition to WRF: (i) daily updated real-time global SST used in Run SST-RTG_low (i.e. the control run) at 0.5° resolution (approximately 45 km in mid-latitudes); (ii) weekly updated GFS skin temperature (Run SST-GFS) produced by GFS using optimum interpolation of satellite measurements of SST at 1° resolution (90 km); (iii) daily updated 0.083° resolution (7.5 km) real-time global SST used in Run SST-RTG_high; (iv) daily updated global analysis of SST obtained from Hybrid Coordinate Ocean Model (HYCOM) and Navy Coupled Ocean Data Assimilation (NCODA) systems (Run SST-HYCOM) at 0.08° resolution (7.2 km); and (v) daily updated advanced very high resolution radiometer (AVHRR) SST (Run SST-AVHRR) at 0.018° resolution (1.6 km), acquired using the 'coldest-dark-pixel' composite technique (Glenn et al. 2016). We conduct five model runs to examine the effects of SST on the storm surge prediction. SST data are updated daily in Runs SST-RTG_low, SST-RTG_high, SST-HYCOM, and SST-AVHRR, whereas SST is held constant in Run SST-GFS. They are used as static SST conditions to WRF and no oceanic feedback is considered. Figure 2.9 shows a snapshot of these SST products in the path of Hurricane Arthur on 3 July. As expected, higher-resolution products from SST-HYCOM and SST-AVHRR depict fine-scale temperature structures that are not captured in SST-RTG_low and SST-GFS.

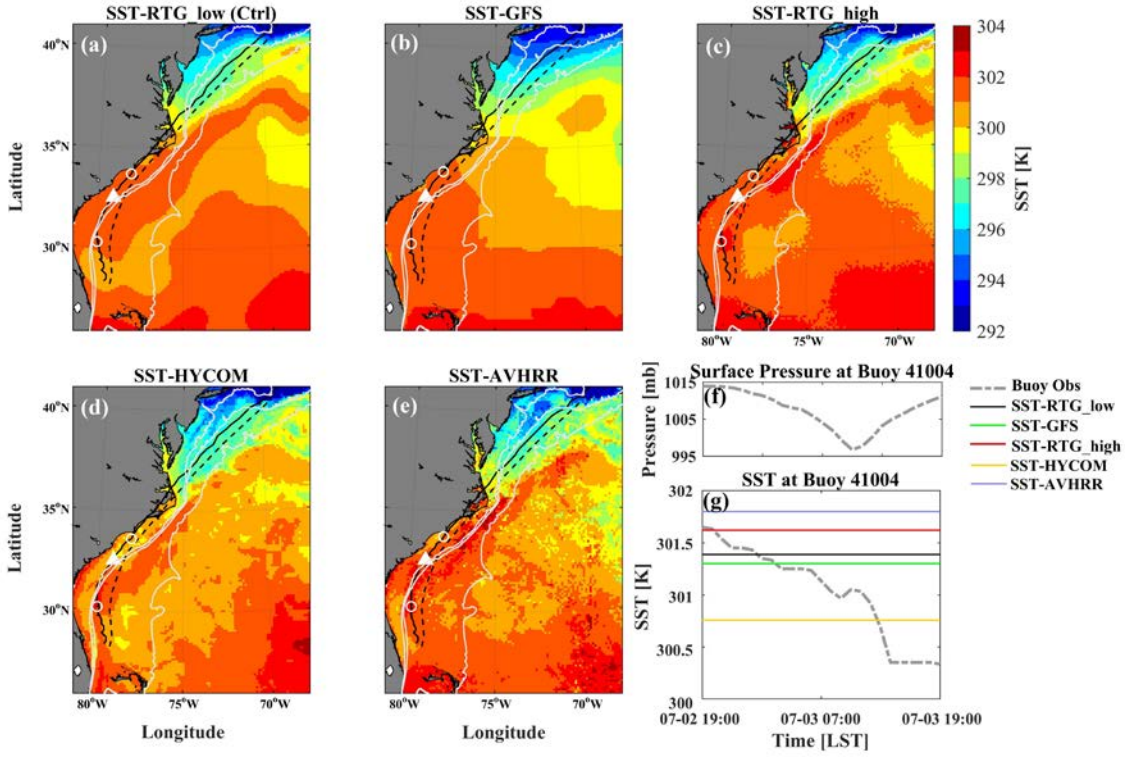

Figure 2.9 (a)-(e) SST (sea surface temperature) distribution on 3 July 2014 from the five model runs used for examining the sensitivity to SST products. (f) Surface pressure time series at Buoy 41004 from National Data Buoy Center. (g) SST observed at the Buoy 41004 and obtained from the five SST products. The open circles in (a)-(e) mark the positions of the storm center at 1900 LST 2 July and 1900 LST 3 July while the white triangle marks the buoy's location.

Runs SST-RTG_low and SST-GFS, which have the coarse spatial resolutions, produce similar predictions for the MSLP and MSW. Run SST-AVHRR predicts stronger MSLP and MSW while Run SST-HYCOM predicts weaker MSLP and MSW (Figures 2.10a and 2.10b). Larger differences are found on 3 July when Arthur was over the Southern Atlantic Bight and the five SST products display large differences in SST. After Arthur's landfall on 4 July, the intensity predictions among the five runs are similar. Because the high resolution AVHRR SST produced a less accurate prediction of storm intensity than the coarse resolution SST products, further investigations were performed, revealing that the AVHRR SST used to force WRF on 3 July was mostly obtained from a

satellite scan at 1354 LST 2 July. AVHRR SST is a multi-channel SST product and consists of the coldest pixels from several satellite scans within a 3-day time window after cloud shields are removed (Glenn et al. 2016). The ocean surface cooled by ~1 K between the time of the satellite scan and the time when Arthur reached a buoy off South Carolina coast (its location shown in Figure 2.9a). Hence AVHRR SST was warmer than the observed SST on 3 July (Figure 2.9g), resulting in a stronger storm in Run SST-AVHRR.

The divergence in the intensity prediction among the five model runs is consistent with the divergence in the surface latent heat flux (Figure 2.10c). When the storm moved over the ocean (on 3 July), the latent heat flux within a radius of 200 km of the storm center is on average 50 W m^{-2} higher in Run SST-AVHRR than that in Run SST-HYCOM. During the storm's transit over Albemarle-Pamlico Sound, however, the differences in the latent heat flux are much smaller. The widening divergence of MSLP and the surface latent flux on 4 July are a manifestation of Arthur's re-entry to the North Atlantic at higher latitudes, owing to differences in SST products over this region. Figure 2.10d shows small differences in the storm track among the five model runs.

Due to the relatively small differences in the intensity prediction around the time of Arthur's landfall, the surge heights predicted by the five models have minor differences (Figures 2.10e and 2.10f). At Oregon Inlet, North Carolina on the southern arc of the Outer Banks, the peak surge heights between Runs SST-RTG and SST-HYCOM are almost identical while the differences in the peak surge heights between Runs SST-AVHRR and SST-GFS are less than 0.2 m. At Duck, North Carolina on the northern arc of the Outer

Banks, the differences in the peak surge heights are even smaller. All five models predict a peak surge height of around 0.7 m. However, the peak surge height arrives 1 hour later in Runs SST-HYCOM, SST-RTG_low and SST-RTG_high than in Runs SST-GFS and SST-AVHRR due to differences in the storm's forward propagation speed (Figure 2.10d).

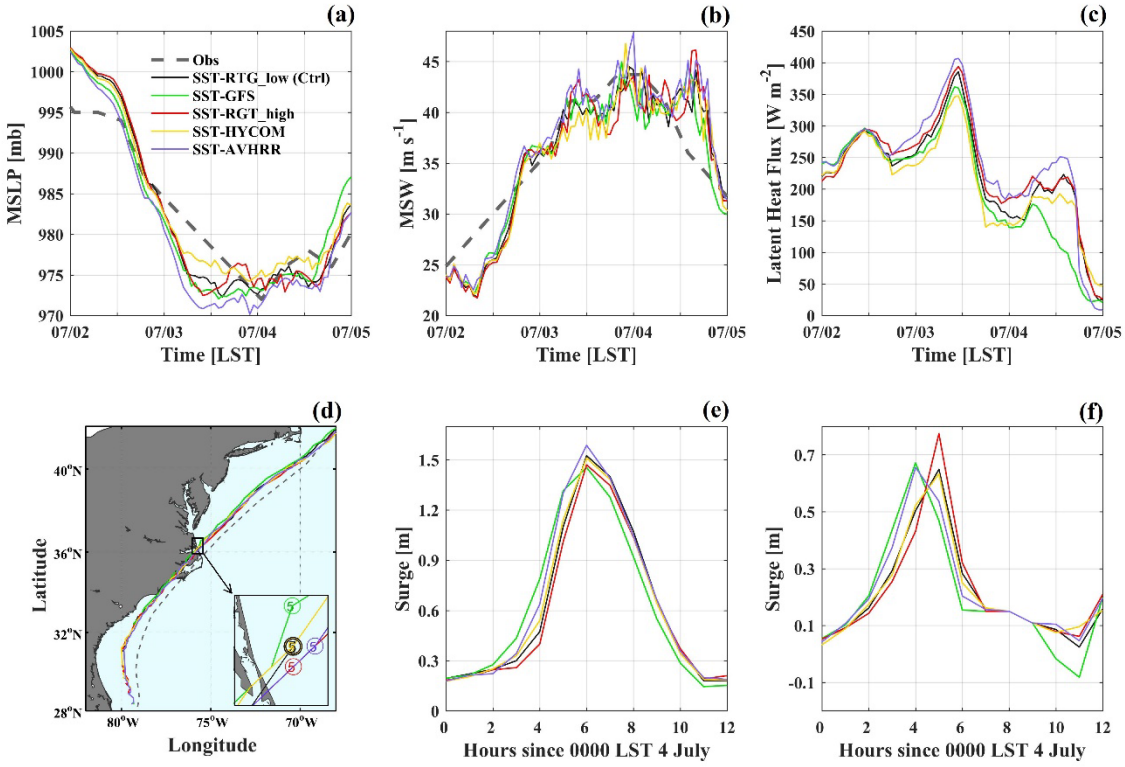

Figure 2.10 Sensitivity analysis to SST products. Time series of (a) MSLP, (b) MSW at 10 m height, (c) the averaged surface latent heat flux within 200 km radius of the storm center, (d) storm track, and the subtidal water level at (e) Oregon Inlet and (f) Duck, North Carolina from Runs SST-RTG_low (black), SST-GFS (green), SST-RTG_high (red), SST-HYCOM (yellow), and SST-AVHRR (purple).

2.5.2 Initial and lateral boundary conditions

Large-scale atmospheric models, which provide the initial and lateral boundary conditions (IBC) to regional WRF models, are not always in good agreement due to their different algorithms and grid resolutions. It is of interest to examine how the discrepancies

in the large scale model predictions propagate to the regional WRF predictions, and eventually to the storm surge predictions. Three commonly used synoptic scale atmospheric models are tested here: (i) the GFS data used in Run IBC-GFS; (ii) the data from the North American Mesoscale model (NAM) used in Run IBC-NAM; and (iii) the data from ERA-Interim used in Run IBC-ERA. GFS has a resolution of 0.5°, which is approximately 45 km in mid-latitudes. NAM has a grid resolution of 12 km and is based on the WRF Non-hydrostatic Mesoscale Model (WRF-NMM). ERA is based on the reanalysis of European Centre for Medium-Range Weather Forecasts model (ECMWF), with 0.7° resolution (63 km). Preliminary numerical experiments showed that the GFS and NAM simulations generated initial conditions similar to those observed but the ERA simulation poorly resolved the initial vortex. To circumvent this initialization problem, the initial vortex from the GFS is superimposed on the ERA field to initialize Run IBC-ERA. The 0.5° resolution real-time global SST is used in this group of model runs.

Unlike the previous model runs which show negligible differences in the storm track, the tracks predicted in Runs IBC-GFS, IBC-NAM and IBC-ERA begin to diverge north of 30°N, reflecting the influence of the synoptic scale weather patterns on the storm's trajectory (Figure 2.11a). The track in Run IBC-ERA shifts eastward from the other two tracks early on 3 July. This is likely related to the longitudinal position of the subtropical ridge, as indicated by the 511 mb pressure contour. This pressure ridge in Run IBC-ERA lies over 100 km to the east of the same ridge in Runs IBC-GFS and IBC-NAM (Figures 2.11g-i). After Arthur's exit from Albemarle-Pamlico Sound and its re-entry into the North Atlantic, the track in Run IBC-NAM shifts eastward off the track in Run IBC-GFS, for the

same reason that the large-scale atmospheric circulation fields diverge between the two runs.

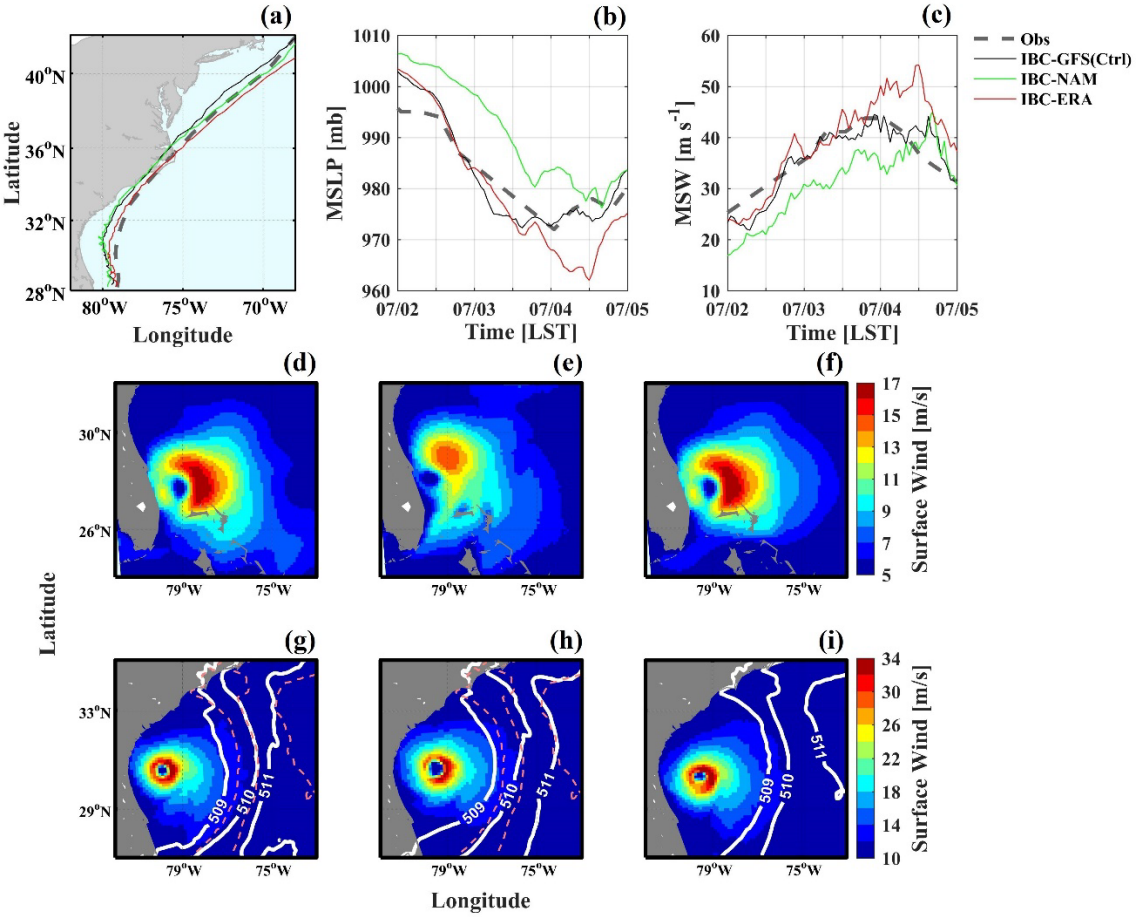

Figure 2.11 Sensitive analysis to IBC (initial and boundary conditions) of WRF. (a) Storm track, (b) MSLP, and (c) MSW at 10 m height from Runs IBC-GFS (black), IBC-NAM (green), and IBC-ERA (red). Surface winds at (d-f) 1900 LST 1 July and (g-i) 2200 LST 2 July from Runs IBC-GFS (d, g), IBC-NAM (e, h) and IBC-ERA (f, i). The white lines in (g-i) mark the ambient pressure field at the height of 500 mb level (unit of mb). The ambient pressure from Run IBC-ERA is shown as the pink-dashed lines in (g)/(f) for comparison.

There are also notable differences in the intensity prediction among the three runs (Figures 2.11b and 2.11c). The storm in Run IBC-NAM has a much slower rate of intensification prior to landfall and is probably related to its initial conditions displaying a weaker and distorted storm vortex (Figure 2.11e). On the other hand, Runs IBC-GFS and IBC-ERA are initialized with the same fully developed vortex (Figure 2.11d, f) and predict

similar storm intensity prior to landfall. During this pre-landfall period, Runs IBC-GFS and IBC-ERA predict almost identical MSWs while Run IBC-NAM predicts lower MSW. After exiting Albemarle-Pamlico Sound and re-entering the North Atlantic, the storm in Run IBC-ERA propagates over the warm water west of the Gulf Stream and experiences further intensification absent in the other two runs (Figure 2.11b). The MSW in Run IBC-ERA becomes 10 m s^{-1} stronger while Runs IBC-GFS and IBC-NAM predict similar values (Figure 2.11c).

The storm surge generated in Run IBC-NAM is somewhat weaker than that in Run IBC-GFS (Figure 2.12). Run IBC-NAM predicts a slower forward propagation speed and exits the northern arc of the Outer Banks at 0700 LST 4 July, 2 hours later than that in Run IBC-GFS. The predicted wind speeds in Run IBC-NAM are only moderately weaker than those in Run IBC-GFS, so only minor differences are seen in the storm surge between the two model runs. Due to its easterly track, the storm surge predicted in Run IBC-ERA is very different from the other two runs (Figures 2.12a-c). The maximum surge region along the northern arc of the Outer Banks shifts southward. The sea-level depression along the southern arc of the Outer Banks is also much larger, as strong eastward winds on the back of the storm drive the water offshore. Moreover, the water-level distribution inside Albemarle-Pamlico Sound is very different between Run IBC-ERA and the other two runs. The winds are predominately northeastward in Runs IBC-GFS and IBC-NAM such that surges are highest in the northeast corner of the Pamlico Sound. The winds are mostly eastward in Run IBC-ERA so that the surges are higher along most of the eastern boundary of the Pamlico Sound.

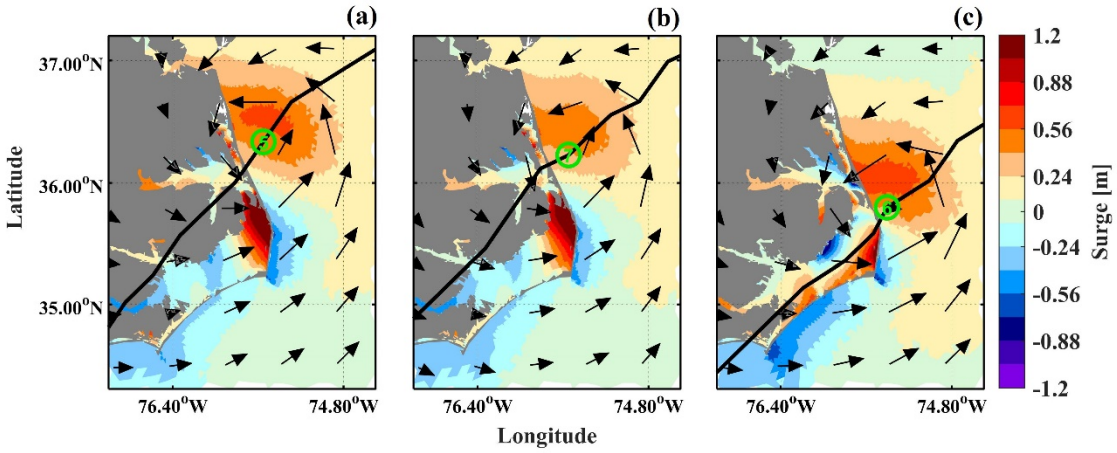

Figure 2.12 A comparison of wind stress vector (arrows), surge heights (color) and storm's track (thick black line) between Runs (a) IBC-GFS (0500 LST 4 July), (b) IBC-NAM (0700 LST 4 July), and (c) IBC-ERA (0600 LST 4 July).

2.6 Discussion and conclusion

In this study we have systematically investigated the sensitivity of storm surge prediction to physics parameterizations and configurations of the initial and boundary conditions in the WRF model. These sensitivity analyses provide useful guidance for selecting certain WRF physics parameterization schemes in storm surge forecasts. For example, the local closure scheme MYJ produces lower equivalent potential temperature than the non-local schemes YSU and ACM2, leading to significant under-prediction of wind speeds and surge heights. Another result of this study is the demonstrated need for cumulus parameterization in the outermost 12-km domain. Without it, the storm intensity is grossly underestimated, leading to significant under-prediction of storm surge. On the other hand, cumulus parameterization does not make much difference in the 4-km WRF domain. It is also interesting to note that none of the choices for the WRF parameterization schemes significantly affect the prediction of Arthur's track.

Other results from the sensitivity analyses are somewhat counter-intuitive and do not lead to obvious recommendations for a specific parameterization scheme or a particular choice for the SST, lateral boundary and initial conditions. Higher-class cloud microphysics schemes WSM5 and WSM6 provide more sophisticated representations of cloud processes but over-predict the wind speed in Hurricane Arthur and result in large over-prediction of storm surge at some coastal locations. In contrast, the lower-class WSM3 produces a more accurate prediction of the storm intensity and storm surge. As demonstrated in the comparison between Runs CM-WSM6 and CM-WDM6, the storm prediction can be quite different even in the same class of microphysics schemes, depending on whether single moment is used to predict the mixing ratio for each species or multiple moments are used to predict additional quantities such as number concentration. Another lesson that has been learned from this study is that high resolution SST products do not necessarily lead to improved predictions of the storm intensity and storm surge. In particular, we need to examine if these SST products capture the pre-storm cooling which has been shown to be a key factor in determining storm intensity on the continental shelf (Glenn et al. 2016; Seroka et al. 2016). It is also worth pointing out that the sensitivity analyses may be different for different storms. Previous sensitivity analyses of hurricane simulations did not yield a unique optimal choice for the physics parameterization schemes (e.g. Li and Pu 2008; Kepert 2012; Zhu and Zhu 2015, Penny et al. 2016).

This leads to our recommendation for using an ensemble approach in storm surge forecasts. Although the ensemble approach is widely used in weather forecasts, it has been rarely used in storm surge modeling. Zou et al. (2013) presented a general modeling

framework to predict coastal flood risk due to wave overtopping by linking meteorological forecasts, wave–tide–surge predictions, nearshore wave models and surf zone models. Colle et al. (2015) used 11-members from an atmospheric Ensemble Kalman Filter system to drive the ADCIRC model and found that the storm surge generated by Hurricane Sandy (2012) in the Metropolitan New York (NYC) area was sensitive to moderate changes in storm track and wind speed. Figure 2.13 summarizes the WRF-FVCOM's skill in predicting the storm surge generated by Hurricane Arthur. Our skill assessment focuses on six tidal gauge stations shown in Figure 2.1b. The pink symbols represent the fifteen individual model runs for different choices of physics parameterization schemes and model configurations. The black symbols represent the ensemble mean prediction for the storm surge. In the Taylor diagram, the correlation coefficient r, the centered-RMSE, and the ratio σ_n of the standard deviations of the model-predicted field (i.e., the test field) and the observed field (i.e., the reference field) are displayed by the location of one point (representing the model field) in relation to the reference point (representing the observed field) (Taylor 2001). Figure 2.13a shows a wide spread in r and σ_n among the individual model runs: r varies between 0.2 and 0.95 and σ_n varies between 0.6 and 1.25. The ensemble mean prediction varies between different tidal stations but falls within much narrow ranges of r=(0.8, 0.95) and σ_n=(0.7, 1.05). The Target diagram provides summary information about the pattern statistics as well as the bias, thus allowing for an assessment of their respective contributions to the total RMSE (Jolliff et al. 2009). Although the normalized biases and center-RMSE in the individual model runs extend to a circle of radius of 1, the ensemble mean prediction falls within a circle of radius of 0.65. Therefore, the ensemble mean prediction substantially improves the prediction of storm surge

generated by Hurricane Arthur. In future studies, it might be interesting to use a larger number of member runs in the model ensemble, including different surface layer parameterization schemes, different numbers of vertical levels, different grid resolutions in WRF, and using 3-dimensional baroclinic FVCOM.

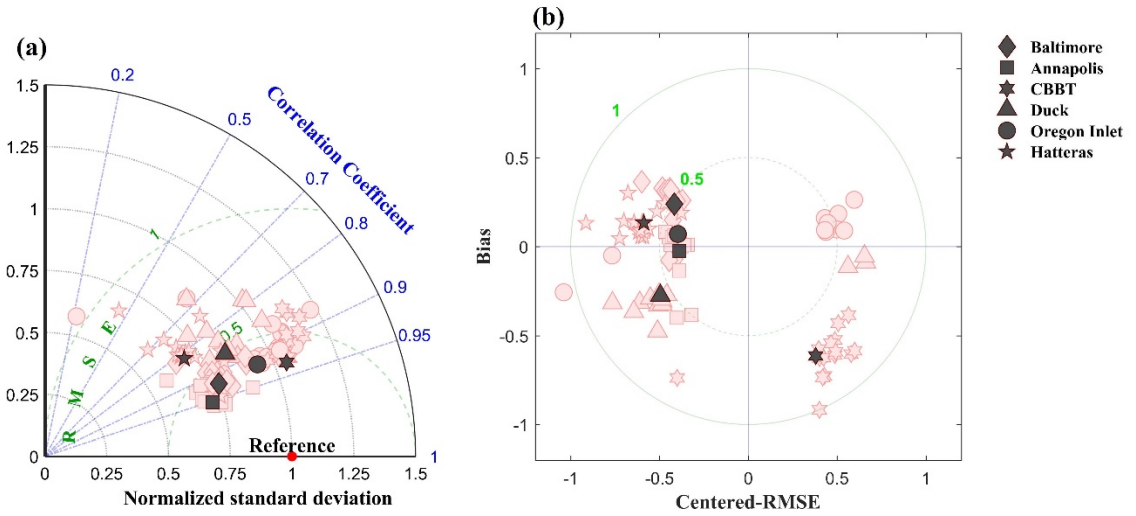

Figure 2.13 (a) Taylor and (b) Target diagrams for the storm surge at six tidal stations. The black symbols represent the ensemble mean predictions and the pink symbols represent results from 15 individual model runs.

The modeling experiments in this study do not consider the oceanic feedback. Chen et al. (2007) showed that high-resolution coupled atmosphere-wave-ocean models were able to capture the complex hurricane structure and intensity change observed in Hurricane Frances (2004). Zambon et al. (2014) used the uncoupled atmospheric model forced by static SST, two-way coupled atmosphere and ocean models and three-way coupled atmosphere, wave and ocean models to simulate Hurricane Sandy (2012) but found relatively minor differences in the predicted track and intensity between the uncoupled and coupled models. Future modeling studies of storm surge should consider using fully

coupled atmosphere and ocean models because they can directly simulate the air-sea fluxes and may provide more accurate predictions of storm intensity and storm surge.

Another factor to consider in storm surge models is the possible effect of baroclinicity on the storm surge prediction. Although several previous studies found minor differences in the sea-level prediction between 3D barotropic and 3D baroclinic ocean models (e.g. Zhong and Li 2006; Ma et al. 2015), Staneva et al. (2016) found up to 20% differences in the surge heights between a 2D barotropic model and a 3D baroclinic model that is coupled to a surface wave model. Some of these differences could be attributed to the effect of wave-current interactions on storm surge (Beardsley et al. 2013). However, the vertical stratification may affect vertical current shear and possibly bottom friction which could indirectly affect the storm surge prediction.

2.7 Acknowledgements

We are grateful to NOAA (NA13OAR4830233) and Maryland Sea Grant (NA14OAR4170090, SA75281450-H) for the financial support. The first author is supported by Maryland Sea Grant Fellowship. We thank Dr. Jun Zhang and two anonymous reviewers for their insightful comments which have significantly improved this paper. Suggestions from Greg Seroka are greatly appreciated. The AVHRR SST data were provided by Travis Miles and Laura Palamara at the Department of Marine and Coastal Sciences, Rutgers University. Model output is available upon request. This is UMCES contribution number 5388.

CHAPTER 3

GENERATION OF NEAR-INERTIAL CURRENTS ON THE MID-ATLANTIC BIGHT BY TROPICAL CYCLONES

Preface

This chapter is a reproduction of work published in the Journal of Geophysical Research: Oceans with coauthors Ming Li and Travis Miles. The right to reuse this work was retained by the authors when publication rights and nonexclusive copyright were granted to the American Geophysical Union.

Zhang, F., M. Li, and T. Miles, (minor revision): Generation of Near-Inertial Currents on the Mid-Atlantic Bight by Hurricane Arthur (2014). Journal of Geophysical Research: Oceans.

3.1 Introduction

When a tropical or an extratropical storm moves over the deep ocean, wind stress fluctuations at frequencies in the near-inertial band can resonantly force inertial currents in the surface mixed layer. Pollard and Millard (1970) and Pollard (1980) found that up to two-thirds of the kinetic energy in the mixed layer is contained within the near-inertial band during storms. The ocean response to a hurricane can be separated into two stages. The "forced" stage response during the storm passage includes strong mixed-layer currents and rapid cooling of the sea surface temperature (D'Asaro et al. 2007; Sanford et al. 2007; Sanford et al. 2011; Cuypers et al. 2013). Price et al. (1994) used a three-dimensional model to simulate the forced stage response to three hurricanes and found that the near-inertial currents (NICs) have a rightward bias due to the coupling between the clockwise-rotating wind stress and mixed-layer currents on the right side of the track. The "relaxation stage" response after the storm passage involves the dispersion of near-inertial frequency internal waves into the stratified interior of the ocean (Price 1983; Gill 1984). Gill (1984) developed a modal model to describe the excitation of sub-mixed-layer motions by a passing storm and found that the energy projects predominantly on the lowest modes. The horizontal scale of the near-inertial waves is initially set by the scales of wind stress in the storm (Price 1983; Gill 1984). Several processes act to decrease the horizontal scales of the mixed-layer motions, generating shorter waves that can propagate into the stratified interior (Alford et al. 2016). In particular, D'Asaro et al. (1995) and D'Asaro (1995a, b) demonstrated the role of the latitude-dependent Coriolis parameter or the β effect in reducing the horizontal scales of the near-inertial waves.

When a storm moves over the continental shelf, however, its wind stress and wind stress curl may excite several different modes of oceanic variability besides the near-inertial waves. Longshore winds could generate upwelling or downwelling along the coast. Onshore winds may drive onshore surface currents and offshore bottom currents, and the resulting shear-induced mixing could lead to rapid ahead-of-eye center cooling of the surface mixed layer (Glenn et al. 2016; Seroka et al. 2016; 2017). Nevertheless, Chen et al. (1996) and Chant (2001) reported observations of low-mode near-inertial internal waves that are consistent with local wind forcing. Shearman (2005) analyzed one-year long observations from the Coastal Mixing and Optics moored array on the New England shelf, and found that a mode-1 baroclinic structure was coherent across the entire shelf, with a magnitude that decreased onshore. This onshore decrease of NICs is consistent with the theoretical prediction of a two-dimensional, linear, flat-bottom, two-layer, coastal wall model by Pettigrew (1981). The presence of a coastal boundary causes divergence in the surface mixed layer, generating NICs below it and leading to low modal wave structure. Shearman (2005) also observed that the near-inertial waves were stronger in the summer and weaker in the winter, following the seasonal cycle in vertical stratification but opposite to the seasonal change in wind stress. MacKinnon and Gregg (2005) analyzed the mooring data collected during the spring stratification period and tracked the generation, evolution and decay of the near-inertial waves. They found that the wave evolution was controlled by the balance among wind stress, bottom drag and turbulent dissipation. Moreover, they observed a switch from mode-1 to mode-2 waves as the stratification evolved, and attributed the switch to nonlinear coupling of the waves through bottom stress.

Although these previous studies have yielded important insights into the structure and dynamics of near-inertial waves on the continental shelf, the coastal ocean response to a passing storm is not completely understood. The mooring observations described above provided detailed time series at a few sites but could not provide a synoptic picture of the shelf-wide response to a storm. It is not clear if the NICs, which dominate the ocean response to storms in the deep ocean, remain to be an important part of the storm-induced currents on the shelf. Neither is it clear if the shear associated with NICs contributes to turbulent mixing and the cooling of the surface mixed layer that may reduce the storm intensity.

Hurricane Arthur (2014) provides a unique opportunity to document and analyze the coastal ocean response to a tropical storm. Arthur moved over the Mid-Atlantic Bight (MAB) on July 4 of 2014, after making landfall in North Carolina and re-entering the North Atlantic (Figure 3.1). Arthur attained a maximum sustained wind (MSW) of over 40 m s-1 at 10 m above the sea surface just before its reentry to MAB (Figure 3.1b). Strong cyclonic winds blew across the entire MAB and the adjacent deep ocean (Figure 3.1c). MSW decreased to about 32 m/s when the center of the storm reached the New England shelf. A network of High-frequency (HF) radars recorded the surface currents generated by Arthur as it propagated northeastward from the Outer Banks of North Carolina to the New England Shelf. A Slocum glider was deployed off the New Jersey Coast prior to the arrival of Hurricane Arthur. It obtained vertical profiles of temperature, salinity and currents in the water column during Arthur's passage over the MAB. These observations, along with hindcast simulations from a three-dimensional numerical model, can be pieced

together to produce a detailed three-dimensional view of the MAB's response to Hurricane Arthur. The numerical model, once validated against the observations, can be used to probe mechanisms driving the spatial and temporal variabilities of the NICs on the shelf.

This paper is organized as follows. Section 2 reports observations of the NICs generated by Hurricane Arthur. Section 3 describes the numerical model. Section 4 shows the model results and the analysis of the near-inertial wave dynamics. Finally, conclusions are made in Section 5.

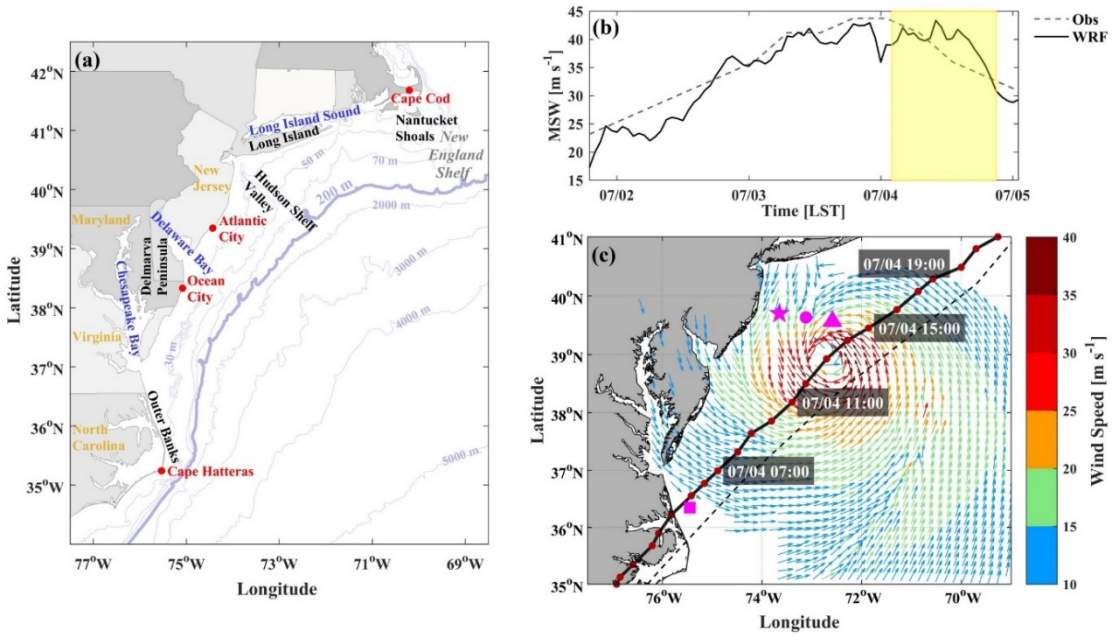

Figure 3.1 (a) Map and bathymetry of the MAB. Water depth drops sharply beyond the 200-m isobath. (b) Time series of the WRF predicted (solid) and observed (dashed) maximum sustained winds (MSW) at 10 m height during the passage of Hurricane Arthur. The shaded area indicates the time period of Arthur's passage over the MAB. (c) Predicted surface winds at 1300 LST 4 July. Wind speeds lower than 10 m s^{-1} are not shown. The black solid line with timestamps (red dots spaced at the interval of 1 hour) represents the predicted storm track, and the black dashed line represents the observed track. The magenta triangle marks Buoy 44066, the magenta star marks the approximate location of the glider, and magenta dot and square mark the third and fourth location used for the rotary spectrum analysis in Figure 3.3, respectively.

3.2 Observations of near-inertial currents

3.2.1 Surface currents from High Frequency Radars

HF radar surface currents were mapped using a network of CODAR SeaSonde stations distributed across the MAB. HF radar measures the radial component of ocean surface currents using the Doppler shift of backscattered radio frequencies from surface waves (Barrick 1971a, 1971b; Teague 1971). Total surface current vectors are determined by combining overlapping radials using an optimal interpolation method to produce hourly surface current maps (Kohut et al. 2012). Kohut et al. (2012) conducted a detailed analysis on the uncertainty of HF radar velocity measurements. They compared the HF radar velocities against the velocities measured by Acoustic Doppler Current Profilers (ADCPs). The root-mean-square differences between the two measurement techniques were typically below 10 cm/s, on the same order of magnitude as the differences between the spatially separated ADCPs themselves. The measurement discrepancies were attributed to differences in the spatial sampling resolution (~6 km resolution in the 5 Mhz HF radar versus point measurements in ADCP) as well as possible mismatches in the measurement depth for the ocean surface layer (~2.4 m for HF radar versus the upper bin width of the ADCP). The HF radar network used in this study sampled across the continental shelf from the shore out to the shelf-break in ideal wave conditions (Roarty et al. 2010). This system is operated by the Mid Atlantic Regional Association Coastal Ocean Observing System (MARACOOS https://maracoos.org/) and was recently repaired and hardened for tropical cyclone impacts based on damages sustained during Hurricane Sandy.

The HF radars produced a sequence of maps of the surface currents as Hurricane Arthur made its way northeastward from Outer Banks of North Carolina to New England Shelf (Figures 3.2a-d). To focus on the currents generated by the storm, harmonic analysis was applied to extract and remove tidal signals from the HF radar data. At 0700 LST 4 July (Figure 3.2a), Arthur's center was off the mouth of Chesapeake Bay. A cyclonic current pattern developed in southern MAB, mirroring the wind stress curl generated by the storm (Figure 3.6a). The currents were much stronger (over 1 m s^{-1}) on the right-hand-side of the storm track than those on the left-hand-side (~ 0.5 m s^{-1}). Farther north, the surface currents were weak (~0.2 m s^{-1}) and mostly directed onshore, likely driven by the easterly winds in the front quadrants of the storm. As Arthur moved northward and further offshore (Figure 3.2b), southward currents occupied the southern and middle parts of the MAB shelf (New Jersey Coast to Outer Banks of North Carolina) while the currents off Cape Hatteras were offshore. At 1500 LST 4 July when the storm center was located off the New Jersey Coast (Figure 3.2c), the southward currents spread across the entire MAB shelf. Noticeably, the surface currents in the middle part of MAB (off New Jersey Coast and Long Island Coast) increased from ~0.2 m s^{-1} to ~0.7 m s^{-1}, while the currents on the southern MAB decreased slightly. At 1900 LST 4 July (Figure 3.2d), Arthur was located over the shelf-break south of Cape Cod. Cyclonic currents developed there, with southward currents on the rest of the MAB shelf.

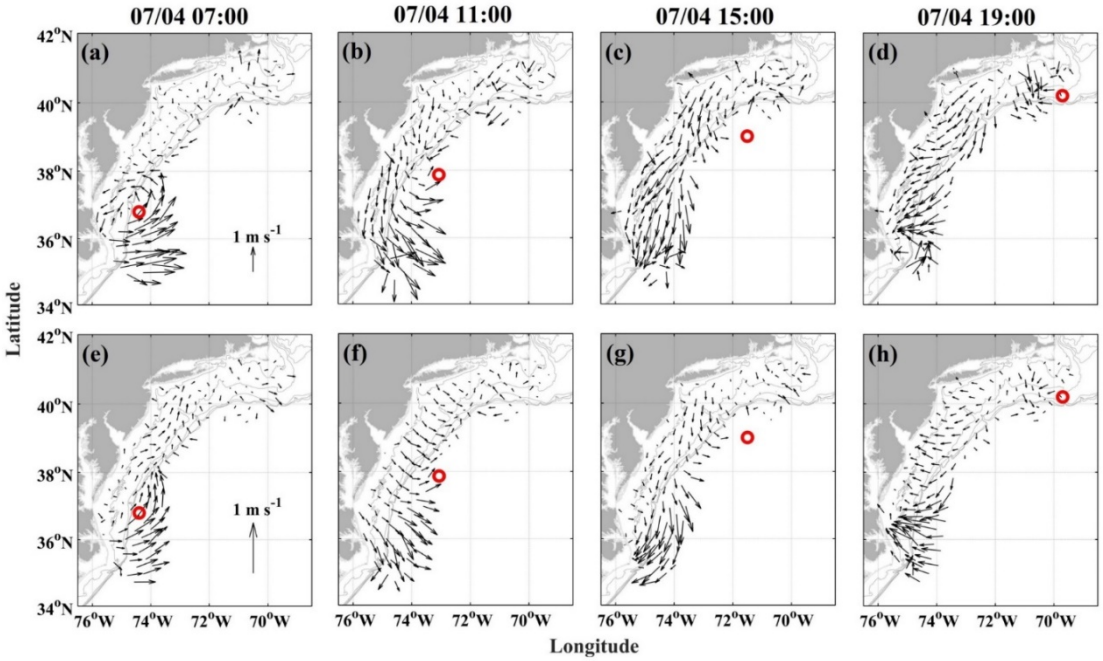

Figure 3.2 Surface subtidal currents observed by HF radar at (a) 0700 LST 4 July, (b) 1100 LST 4 July, (c) 1500 LST 4 July, and (d) 1900 LST 4 July. (e)-(h) Surface NICs at the same times as (a)-(d). The red circle marks the storm center in each snapshot.

NICs were a major component of the storm-driven currents and were extracted from the detided currents using a 6th-order bandpass Butterworth filter set at (0.8 – 1.2) *f* (local inertial frequency). HF radar data with less than 90% temporal coverage were excluded from the analysis, and other smaller data gaps were patched using linear interpolation. At 0700 LST 4 July the surface NICs showed strong cyclonic currents (>0.5 m s^{-1}) on the right side of the storm's center but weak currents (<0.2 m s^{-1}) on the inner shelf (Figure 3.2e). As Arthur continued its path northward and off to the deep ocean, the HF radar could only provide a partial view of the surface currents up to the shelf-break (Figures 3.2f-h). Nonetheless, NICs, rotating clockwise in time with a velocity magnitude of 0.1-0.3 m s^{-1}, were observed throughout the MAB shelf. At 1900 LST 4 July, strongest NICs were still

seen in southern MAB even though the storm's center had already moved to the New England Shelf (Figure 3.2h).

When a hurricane moves over the deep ocean, the dominant oceanic response is the NICs (Price 1983; Price et al. 1994; Sanford et al. 2007; Sanford et al. 2011). When a hurricane moves over the continental shelf, however, other types of currents could be generated (Glenn et al. 2016). To discern the role of NICs on the shelf, we calculated the rotary spectra using the HF radar total velocity time series between 2 and 12 July at four locations: an inshore location (~30 m isobath, near the glider track), a mid-shore location (~50 m isobath, mid-point between the glider and buoy) and an offshore location (~80 m isobath, Buoy 44066) along a cross-shelf section off New Jersey Coast; a location off the Virginia Coast (Figure 3.3). At the inshore location with strong semi-diurnal tides, the NICs only had less than one half of the M2 tidal energy, although it was still higher than K1 tide (Figures 3.3a and 3.3b). At the mid-shore and offshore locations (Figures 3.3c-f), however, NICs had much higher energy content than the tidal components and dominated the energy spectrum. At the southern station off the Outer Banks, the spectrum had a peak at 1 day-1 frequency, but diurnal tides are weak there (Lentz et al. 2001). The peak probably represented the wind-driven longshore currents in this region (see Figures 3.2a-d). Figure 3.2 clearly shows large differences between the total subtidal currents and the NICs in the southern MAB (compare the top and bottom panels). Overall, NICs were a major component of the shelf currents on the MAB during the passage of Hurricane Arthur.

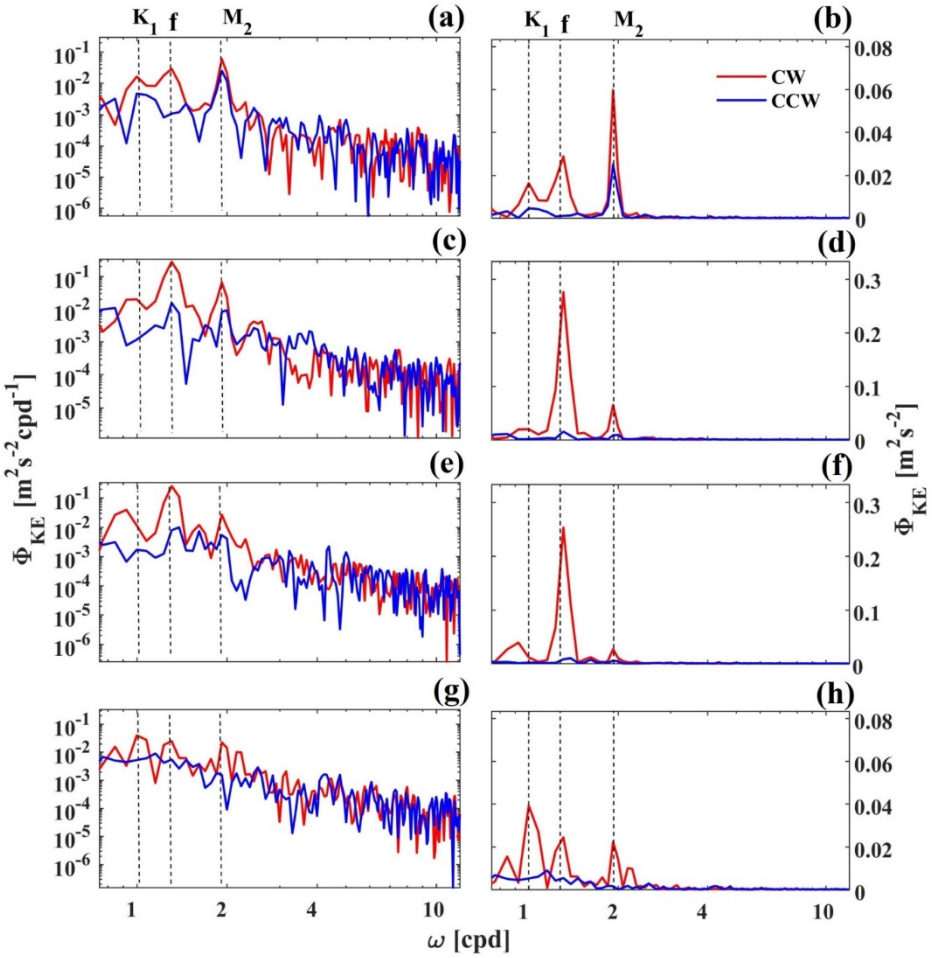

Figure 3.3 (a)/(c)/(e)/(g) Rotary spectra and (b)/(d)/(f)/(h) variance preserving spectra for the surface currents at three locations in a northern MAB section and one location in southern MAB (their locations marked by large magenta symbols in Figure 3.1c). The spectra are calculated from the HF radar time series between 2 and 12 July.

3.2.2 Glider observations

Autonomous underwater gliders have become reliable storm sampling platforms (Miles et al. 2013, 2015, 2017; Glenn et al. 2016) capable of obtaining high vertical resolution data at ~2 Hz with fall speeds on the order of 0.1 m s^{-1}. The glider uses a combination of adjustable buoyancy and a set pitch angle to achieve forward motion at nearly 20 km day^{-1}. The data used in this study was collected by a Slocum glider, RU30,

operated by Rutgers University. This system was equipped with a suite of oceanographic sensors, including (1) a Seabird Scientific pumped conductivity-temperature-depth (CTD) sensor, (2) a Wetlabs Inc. eco-triplet measuring chlorophyll fluorescence (chl), colored dissolved organic matter (CDOM), and optical backscatter at 700 nm wavelength (bb700), (3) an Aandera oxygen optode in the aft section measuring oxygen concentration and saturation, and (4) an externally mounted upward looking Nortek 1 Mhz Aquadopp current profiler. The Aquadopp was designed to collect data on downcasts at a nominal pitch angle of 26.5°, which oriented the three-beam transducers vertically upward. The Aquadopp was configured to collect data at 1 Hz with 10 bins. Compass calibration was performed prior to deployment, including a 24-point check with a hand compass to provide post-deployment corrections for known elliptical biases exaggerated in the eastward and westward direction. Absolute current velocities were calculated following standard LADCP procedures that had been adapted to use on shallow Slocum glider platforms (Miles et al. 2017).

The glider was deployed off the New Jersey Coast prior to the arrival of Hurricane Arthur. The glider moved around (73.6ºW, 39.7ºN) between 4 and 8 July and trespassed an area no larger than 60 km^2 (Figure 3.4a). Figure 3.4b showed the time series of the wind speed vector measured at a buoy further offshore (Buoy 44066 of the National Data Buoy Center). The winds there rotated counter-clockwise during Arthur's passage, switching from northeasterly on July 4 to southwesterly on July 7. The peak wind speed reached over 20 m s^{-1} on July 4. The glider observed strong stratification on the shelf, with a sharp thermocline separating the warm surface water from the cold bottom water as shown in

Figure 3.4c (the density field displays essentially the same vertical structure). On the MAB a band of cold bottom water occupies the shelf from spring to fall (Houghton et al. 1982; Castelao et al. 2010; Lentz 2017). Prior to the arrival of Arthur, temperature in the surface layer was nearly uniform and at 24ºC whereas temperature in the bottom Cold Pool was around 11ºC. These compare with the long-term averaged surface layer temperature of ~22ºC and bottom water temperature of ~11ºC in July (Castelao et al. 2010; Fleming 2016), indicating that the stratification on the MAB prior to Arthur's arrival was slightly stronger than the average. In addition, the thermocline depth was at ~13 m, shallower than the ~17 m found in the monthly climatology for July. Wind-induced mixing caused the surface mixed layer to deepen from ~13 m to ~18 m. In the mean time, temperature in the surface mixed layer decreased from 24ºC to 20ºC. After Arthur's departure surface layer temperature bounced back to 22ºC.

The glider made repeated profiling of currents in the water column over the four-day deployment period. After the depth-averaged current was removed, both the zonal and meridional velocities displayed a mode-1 baroclinic structure, reminiscent of the mode-1 near-inertial waves as observed by MacKinnon and Gregg (2005) and Shearman (2005) on the New England shelf (Figures 3.4e and 3.4g). These baroclinic currents oscillated at a period of about 18 hours and were essentially the NICs. The surface and bottom NICs had a similar velocity magnitude (~0.2 m s^{-1}).

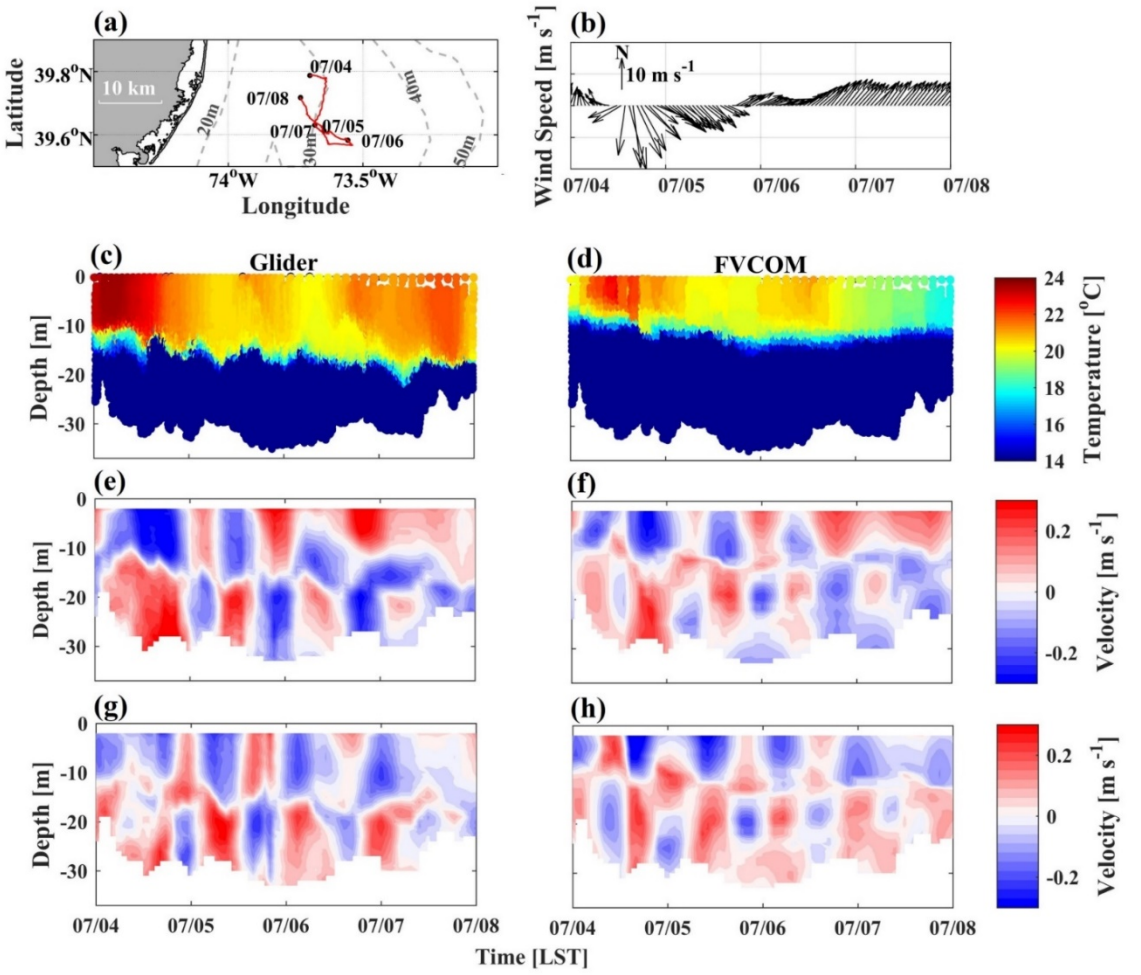

Figure 3.4 (a) Zoomed-in view of the glider track (red line). (b) Time series of the wind speed vector measured at the Buoy 44066. Time-depth distributions of (c)/(d) temperature, (e)/(f) zonal and (g)/(h) meridional baroclinic velocity components obtained from the glider measurements (left column) and from the FVCOM model (right column).

3.3 Model description

To interpret the observed spatial and temporal variabilities of NICs, a 3-dimensional hydrodynamic model based on the unstructured-grid Finite Volume Coastal Ocean Model (FVCOM) (Chen et al. 2003) was configured for the MAB and adjacent estuaries including Chesapeake Bay, Delaware Bay and Long Island Sound (Figure 3.5a). The eastern boundary is placed about 300 km from the coast while the southern and northern boundaries are roughly perpendicular to the coast, located at 34°N and 42°N,

respectively. The model domain covers the entire MAB shelf from Cape Hatteras, North Carolina, to Cape Cod, Massachusetts with a horizontal resolution of ~5 km. The bathymetry data were extracted from the 1 arc-minute ETOPO1 Global Relief Model (Amante and Eakins 2009). In the vertical direction, a hybrid coordinate system is used. The water column is evenly divided into 30 levels when water depth is less than 150 m. When water depth exceeds 150 m, however, both the surface mixed layer and bottom boundary layer are discretized into 5 layers with a thickness of 5 m in each layer while the rest of the water column is evenly divided into 20 levels. The horizontal eddy viscosity and diffusivity are set to 0.1 $m^2 s^{-1}$ and 1 $m^2 s^{-1}$, respectively. The vertical eddy viscosity and diffusivity are computed using the $k - \varepsilon$ turbulence closure scheme incorporated into the General Ocean Turbulent Model (Burchard 2002; Warner et al. 2005), and the background diffusivity and viscosity are 10^{-5} m^2 s^{-1} and 5×10^{-6} m^2 s^{-1}, respectively. A quadratic stress is applied at the sea bed, assuming that the bottom boundary layer is logarithmic with a roughness height of 2 cm (Churchill et al. 1994), same as that used in Experimental System for Predicting Shelf and Slope Optics (ESPreSSO, http://www.myroms.org/espresso/). A barotropic version of this model was used to study tides and storm surge in Lee et al. (2017) and Zhang et al. (2017).

For the baroclinic version used in this study, the FVCOM model is initialized on 1 January 2014 with fine-resolution predictions of temperature, salinity and sea level from the ESPreSSO. At the offshore open boundary, the tidal variation of sea level is prescribed using five tidal constitutes (M_2, S_2, N2, K1, and O_1) from the Oregon State University global tidal model TPXO 7.1 (Egbert and Erofeeva 2002). In order to simulate the effects

of the Gulf Stream and large-scale currents on the MAB shelf, the regional FVCOM model is nested into Hybrid Coordinate Ocean Model and Navy Coupled Ocean Data Assimilation systems (HYCOM-NCODA, http://hycom.org) using one-way nesting, for which the inner model receives its boundary values from the outer model at the inner model open boundaries. This is consistent with the configuration of the initial condition since ESPreSSO is also forced by HYCOM-NCODA at its open boundaries. The daily data of sea surface height, salinity, temperature, and current velocities are extracted from the HYCOM-NCODA database and interpolated to the open boundary nodes of the regional FVCOM model. They provide the subtidal component of the open boundary conditions while the tidal component is obtained by running the regional model with tidal forcing only. The two components are then added together to prescribe the open boundary conditions for the regional FVCOM model. The surface momentum and heat fluxes are prescribed using hourly outputs from the Weather Research and Forecasting (WRF) model that was developed to predict Hurricane Arthur between 2 and 6 July (Zhang et al. 2017), and using the outputs from the North American Regional Reanalysis (NARR, https://www.esrl.noaa.gov/psd/data/gridded/data.narr.html) at 3-hour intervals during other times of the model integration. The freshwater flows from Susquehanna River, Delaware River, Hudson River and other small tributaries are prescribed according to measurements at the U.S. Geological Survey water gauge stations.

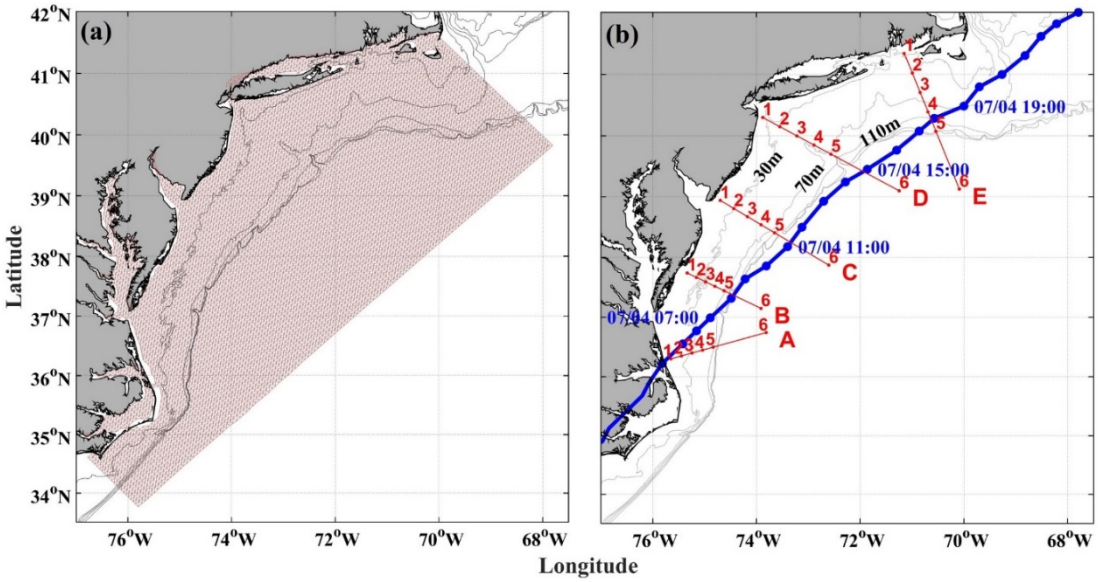

Figure 3.5 (a) FVCOM model grids over MAB. (b) Five representative cross-shelf sections (marked as A-E, red lines) used to investigate the spatial variability of NICs over MAB. In each section, six points (numbered 1-6) are selected for detailed analysis in Figures 3.7 and 3.11. The blue line with solid dots marks the storm's track and the bathymetry is shown as gray contour lines.

3.4 Model results

3.4.1 Spatial and temporal variabilities of NICs

Since its range was limited to the shelf-break, HF radars only provided a partial view of the surface currents generated by Hurricane Arthur. On the other hand, the regional FVCOM model provided a complete view of the current field (Figure 3.6). To help understand the storm-driven currents, surface winds from the WRF model are shown in Figures 3.6a-d. The FVCOM model did a good job in capturing the dominant current patterns observed during Arthur's passage over the MAB shelf (compare Figures 3.2a-d and Figures 3.6e-h): cyclonic currents around the storm's center at 0700 LST 4 July and strong southward currents over the entire shelf over the next 12 hours. The model also showed that strong cyclonic currents continued to develop underneath the storm's center as Arthur moved northeastward, and tracked the patterns of wind stress curl produced by

the storm (Figures 3.6a-d). The currents had strong left-to-right asymmetry across the storm's track: the currents on the right side of the storm's center were over twice stronger than those on the left side. The currents in the near-inertial frequency range (0.8 – 1.2 *f*), namely NICs, also displayed the strong left-to-right asymmetry (Figures 3.6i-l). However, NICs did not show strong cyclonic currents underneath the storm's center. The NICs at any particular location were initially generated by the strong winds in the right front quadrant and then rotated clockwise due to the action of the Coriolis force. One can clearly see the stronger NICs in the deep ocean to the right of the shelf-break (Figures 3.6i-l). On the MAB shelf the NICs were considerably weaker.

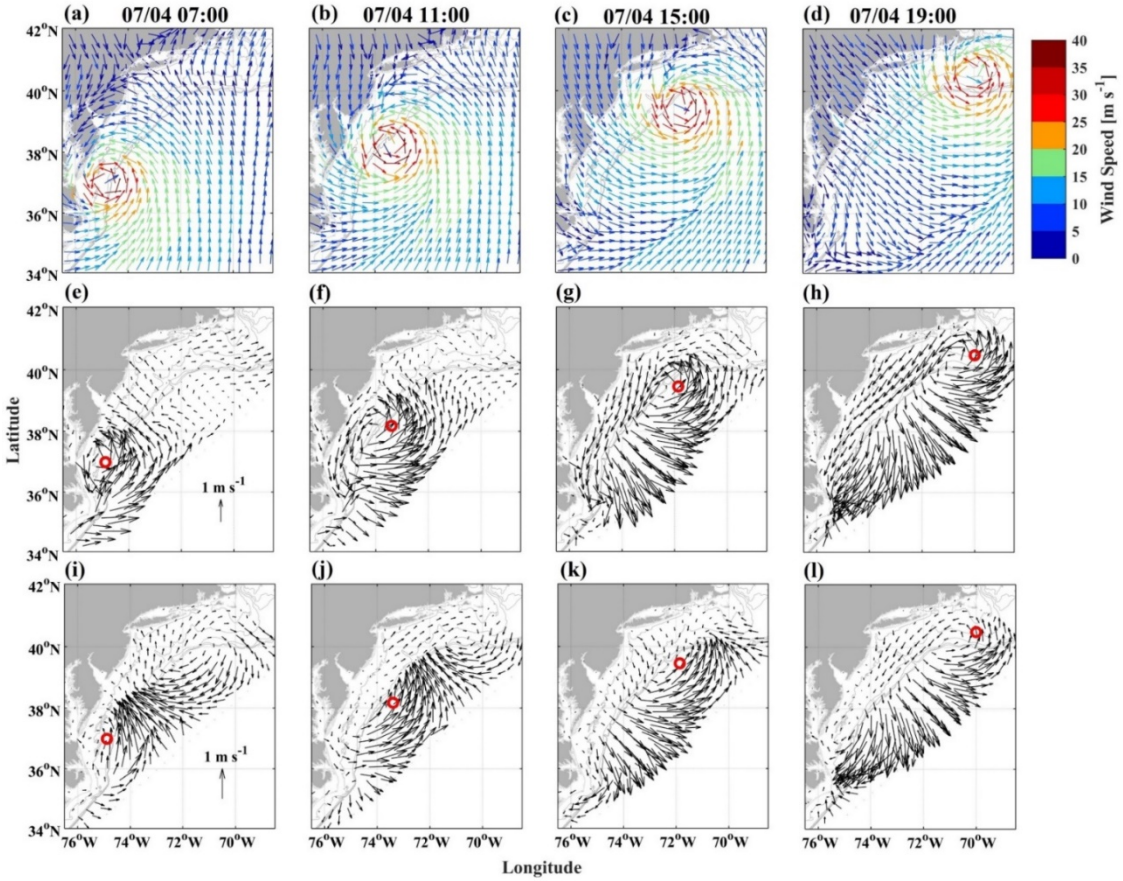

Figure 3.6 WRF-predicted wind speed vectors at 10-m height at (a) 0700 LST, (b) 1100 LST, (c) 1500 LST, and (d) 1900 LST 4 July. FVCOM-predicted (e)-(h) surface subtidal currents and (i)-(l) surface NICs at the same times as (a)-(d).

The above snapshots describe the spatial variations of NICs at four different times during Arthur's transit over MAB. To further investigate the temporal evolution of NICs, we plot 14-day time series of NICs at a number of virtual sampling stations (Figure 3.7). Five cross-shelf sections are selected to represent the southern, middle and northern regions of MAB (Figure 3.5b): Section A extends offshore from the Outer Banks of North Carolina where Arthur re-entered the North Atlantic; Section B extends offshore from the Delmarva Peninsula (mid-point between the mouths of Chesapeake and Delaware Bays); Section C is placed off the southern New Jersey Coast (north of Delaware Bay); Section D is located in the Hudson Shelf Valley which has the deepest bathymetry on the MAB; and Section E is positioned east of Long Island Sound to cover the New England Shelf. Along each cross-shelf section, five stations are evenly spaced out on the shelf and one station is located offshore of the shelf-break. The time series of NICs were extracted from both the HF radar observations and the FVCOM model outputs using harmonic analysis and bandpass filter described in Section 2. Velocities in the zonal and meridional directions were rotated to the cross-shelf and along-shelf directions. Since the cross-shelf and along-channel velocities showed similar temporal variabilities and were of similar magnitude, our analysis focuses on the cross-shelf velocity in Figure 3.7.

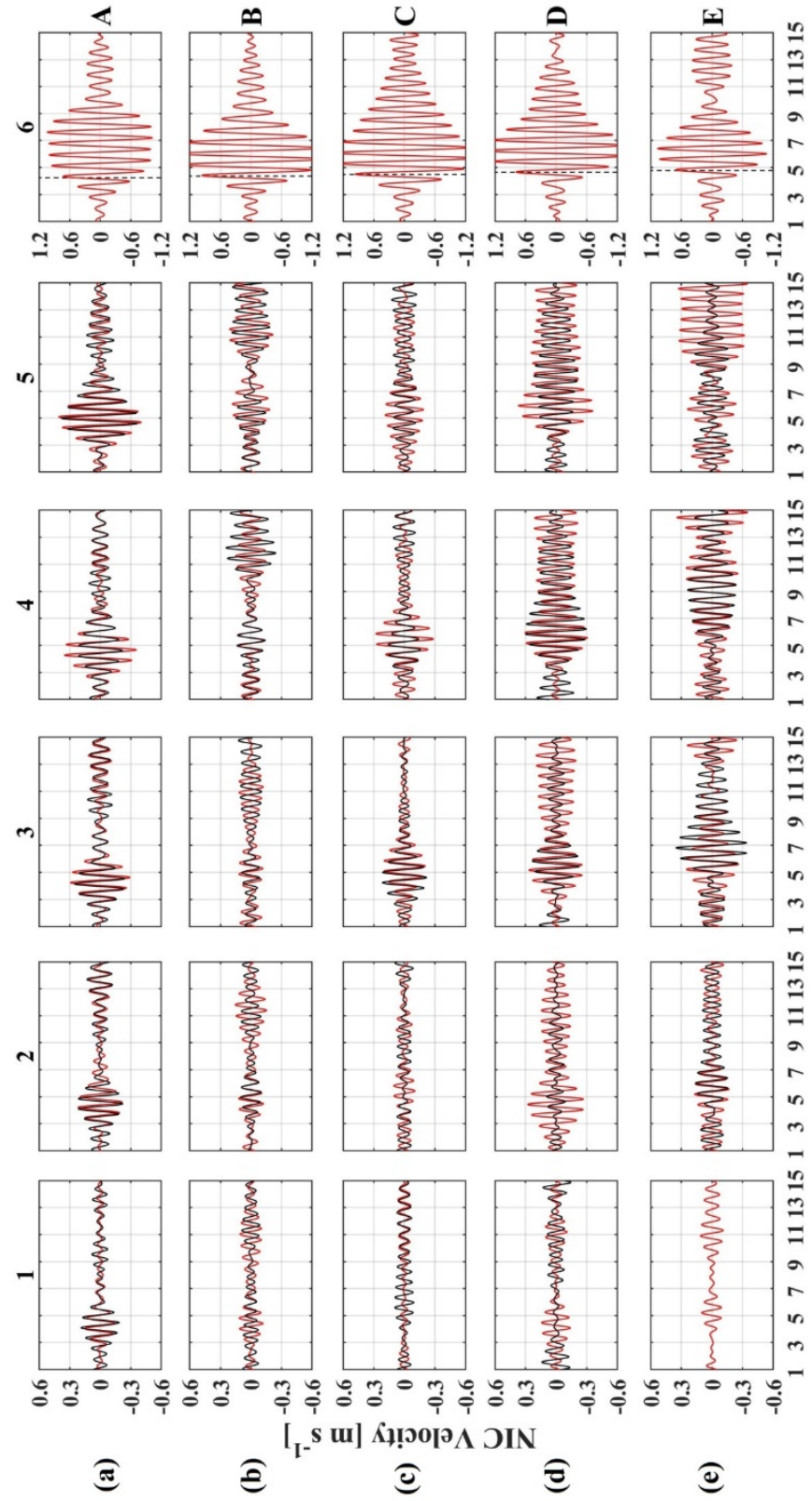

Figure 3.7 Time series of the cross-shelf component of the surface NICs at six virtual sampling stations (numbered 1-6) along the cross-shelf sections A-E over MAB: HF radar observations (black) and FVCOM model result (red). The dashed black lines in Column 6 indicate the times when Arthur was closest to each section.

At each cross-shelf section, the NICs on the shelf were about one fourth to one third of those (about 1.2 m s^{-1}) in the deep ocean and decreased from the shelf-break to the inner shelf (Figure 3.7). The NICs had a peak magnitude of 0.3 m s^{-1} in southern MAB (Section A) but decreased to 0.2 m s^{-1} in the middle part of MAB (Sections B and C). They rebounded to 0.3 m s^{-1} in northern MAB (Sections D and E), even though the maximum surface winds decreased from ~40 m s^{-1} in southern MAB to ~30 m s^{-1} in the northern MAB (Figure 3.1b). One also notices interesting differences in the temporal evolution of the NICs between the southern and northern parts of MAB. The NICs in the southern MAB shelf attenuated quickly and lasted for 3-4 days (Figure 3.7a). In contrast, the NICs in the northern MAB shelf persisted for ~10 days. They are in general good agreements on the spatial and temporal variabilities of NICs between the model predictions and HF radar observations. Averaged over all stations, the correlation coefficient between the predicted and observed NICs is 0.48 and the root-mean-square error is 0.09 m s^{-1}. One exception is E5 where the observed NICs displayed a rapid decay after July 11 but the predicted NICs persisted. A possible cause for the discrepancy is that E5 was the farthest station from the coast (at the shelf-break) and the HF radar measurements there may be inaccurate. Observations at nearby stations such as E4, D5 and D4 showed sustained NICs consistent with the model results. The observed and predicted NICs show phase differences at some locations such as C5 and D5. Given their close proximity to the storm track, a small difference between the predicted and observed tracks (about 50 km, see Figure 3.1c and Zhang et al., 2017) could cause these phase differences.

3.4.2 Energy budget analysis

As a step towards understanding the spatial variability of the NICs generated by Hurricane Arthur, we mapped out the spatial distribution of the depth-integrated kinetic energy (*KE*) of the near-inertial waves and compared it with the wind energy input to the near-inertial frequency band. The depth-integrated *KE* is given by

$$KE = \int_{-H}^{0} \frac{1}{2}\rho\left|\overrightarrow{U'}\right|^2 dz \tag{3.1}$$

where H is the water depth, ρ is the density, and $\overrightarrow{U'}$ is the horizontal velocity vector in the near-inertial frequency bands. *KE* is averaged over the 10-day period (2 to 12 July) when the NICs were affected by Arthur. *KE* was much larger in the deep ocean than on the shelf, and was low near the coast but increased in the offshore direction (Figure 3.8a). There was a band of relatively high *KE* in the mid-shelf region between the Nantucket Shoals and Atlantic City, New Jersey. In contrast, *KE* was considerably lower in the mid part of MAB (Section B and C) between Ocean City, Maryland and Atlantic City, New Jersey (see Figure 3.1a for a map of these geographic locations).

Much of the *KE* differences between the MAB shelf and the deep ocean may be explained by the asymmetry in the wind energy input to the near-inertial waves,

$$W_{\tau s} = \overrightarrow{\tau_s} \cdot \overrightarrow{U_s'} \tag{3.2}$$

where $\overrightarrow{\tau_s}$ is the surface wind stress vector and $\overrightarrow{U_s'}$ is the surface NICs velocity vector, following the approach of D'Asaro (1985). $W_{\tau s}$ was averaged over the same 10-day period as for *KE*. The wind energy input showed strong left to right asymmetry with respect to the storm's track (Figure 3.8b). Therefore, a large part of the *KE* differences between the shelf and the deep ocean was simply due to the left to right asymmetry in $W_{\tau s}$. On the MAB shelf

itself, the band of relatively high *KE* in the mid-shelf region between the Nantucket Shoals and Atlantic City was also associated with higher wind energy input into the near-inertial waves. However, there was no one-to-one correspondence between *KE* and $W_{\tau s}$. In southern MAB (including the cross-shelf section A), the time averaged *KE* was low but $W_{\tau s}$ was high there (compare Figures 3.8a and 3.8b).

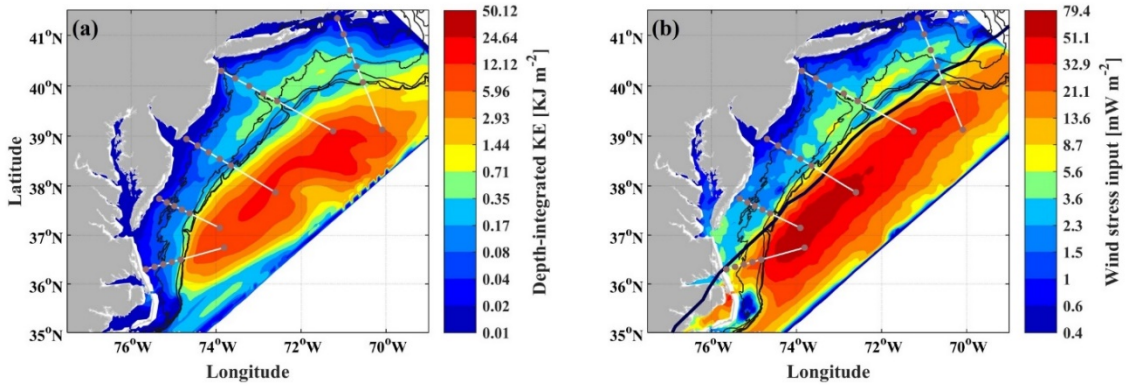

Figure 3.8 (a) Depth-integrated kinetic energy of the near-inertial waves and (b) wind energy input into the near-inertial waves. Both are averaged between 2 and 12 July. The five cross-shelf sections as well as the virtual sampling points used in Figure 3.7 are shown. The thick black line in (b) represents the predicted storm's track. Color-bars are in logarithmic scale.

Further insights into the wind generation of NICs can be obtained by comparing the time series of the wind energy input at different locations. At station D6 in the deep ocean, which lay on the right side of the storm's track, the wind stress vector rotated clockwise and remained nearly parallel with the clockwise-rotating NICs (Figures 3.9a and 3.9b). This resulted in a large flux (a maximum of ~3 W m^{-2}) of wind energy to the NICs (Figure 3.9c) and rapid increase of surface NICs from 0.3 m s^{-1} on early 4 July to 1.2 m s^{-1} on 5 July (Figure 3.9b). At the shelf station D5 on the left side of the track, the wind stress was 50% smaller and rotated counter-clockwise (Figure 3.9d) while the NICs rotated clockwise (Figure 3.9e). Consequently, the coupling between the wind stress and inertial currents was much less efficient and produced an energy flux (a maximum of ~0.3 Wm^{-2})

that was only 10% of that at station D6 (Figure 3.9f). The surface NICs at D5 only reached about 0.2-0.3 m s^{-1}, approximately one-fourth of the NICs speed at D6. At the shelf station B5 further south, which was located closer to the storm's center, the magnitude of the wind stress was larger than that at D5 (compare Figures 3.9g and 3.9d). Initially the northwestward wind stress coincided with the northwestward NICs, producing a pulse of wind energy to NICs. Later on, however, the wind direction shifted by 180° and became southwestward while the NICs were still directed in the northwest directions (Figures 3.9g-h). This resulted in negative wind work because the wind stress vector and the NICs vector varied out of the phase (Figures 3.9i). When integrated over time, the net wind energy input to NICs was much lower at B5. This explains the low *KE* level in the middle part of MAB (between Ocean City, Maryland and Atlantic City, New Jersey).

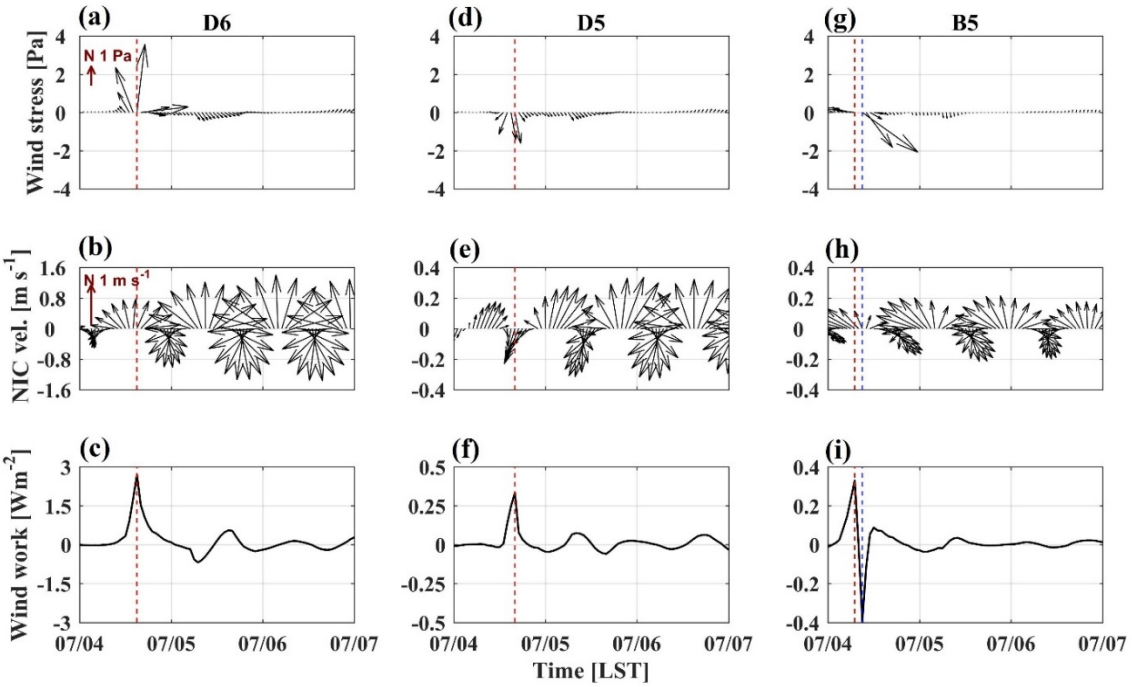

Figure 3.9 (a)/(d)/(g) Surface wind stress, (b)/(e)/(h) surface NICs, and (c)/(f)/(i) wind energy input obtained from the WRF-FVCOM models: D6 (left column), D5 (middle column); B5 (right column). In the right column the red-dashed lines indicate the time of peak positive wind work, and the blue-dashed lines indicate the time for peak negative wind work.

An understanding of the discrepancy between *KE* and $W_{\tau s}$ in southern MAB requires us to examine other terms in the energy budget for the near-inertial waves (e.g., Chant 2001; Zhai et al. 2009):

$$\frac{\partial KE}{\partial t} = W_{\tau s} - W_{\tau b} - \varepsilon - \int_{-H}^{0} PEC\ dz - \int_{-H}^{0} \nabla \cdot KE_{adv}\ dz - \int_{-H}^{0} \nabla \cdot F\ dz + others \quad (3.3)$$

where $W_{\tau b}$ is the bottom friction work, ε is the depth-integrated dissipation of *KE* associated with vertical viscosity, *PEC* is the conversion rate of *KE* into potential energy of near-inertial waves, KE_{adv} is the advection of *KE*, *F* is the near-inertial wave energy flux, and *others* include non-linear energy transfer to other frequency band and the depth-integrated dissipation of *KE* associated with horizontal viscosity. The bottom friction work can be written as

$$W_{\tau b} = \overrightarrow{\tau_b} \cdot \overrightarrow{U_b'} \quad (3.4)$$

where $\overrightarrow{\tau_b}$ is the bottom stress and $\overrightarrow{U_b'}$ is the bottom NICs velocity. The depth-integrated dissipation of *KE* due to vertical viscosity is calculated by

$$\varepsilon = \int_{-H}^{0} \rho K_v \left(\frac{\partial^2 u'}{\partial z^2} + \frac{\partial^2 v'}{\partial z^2}\right) \quad (3.5)$$

where K_v is the vertical eddy viscosity and *u'* and *v'* are zonal and meridional NICs velocity components, respectively.

We compared the energy budget balance at two locations on the MAB shelf: station A4 where NICs were strong initially but damped out quickly (Figure 3.7a) such that the time-averaged KE was low (Figure 3.8a); station D4 where NICs were strong and persisted for ~10 days (Figures 3.7d and 3.8a). Figure 3.10 shows that the primary balance in the kinetic energy budget was between the wind energy input and energy dissipation. At station A4 in the southern MAB, the wind energy input was high due to its closeness to the storm's

center and strong winds. It was counter-balanced by strong energy dissipation. In contrast, both the wind energy input and dissipation were much smaller at D4 in the northern MAB. Therefore, in the southern MAB the strong energy dissipation constrained the growth of NICs energy even though the wind work was larger there. The frictional dissipation in the bottom log layer was less than 10% of ε. The energy dissipation ramped up quickly at the southern station A4 to balance the wind work such that *dKE/dt* switched from positive sign to negative sign in early July 5 (Figure 3.10c). This explains the rapid damping of NICs seen in Figure 3.7 (first row). On the other hand, there was a delay for the dissipation to catch up with the wind input at the northern station D4 such that *dKE/dt>0* until 7 July (Figure 3.10d). Hence the NICs at D4 persisted for up to 10 days.

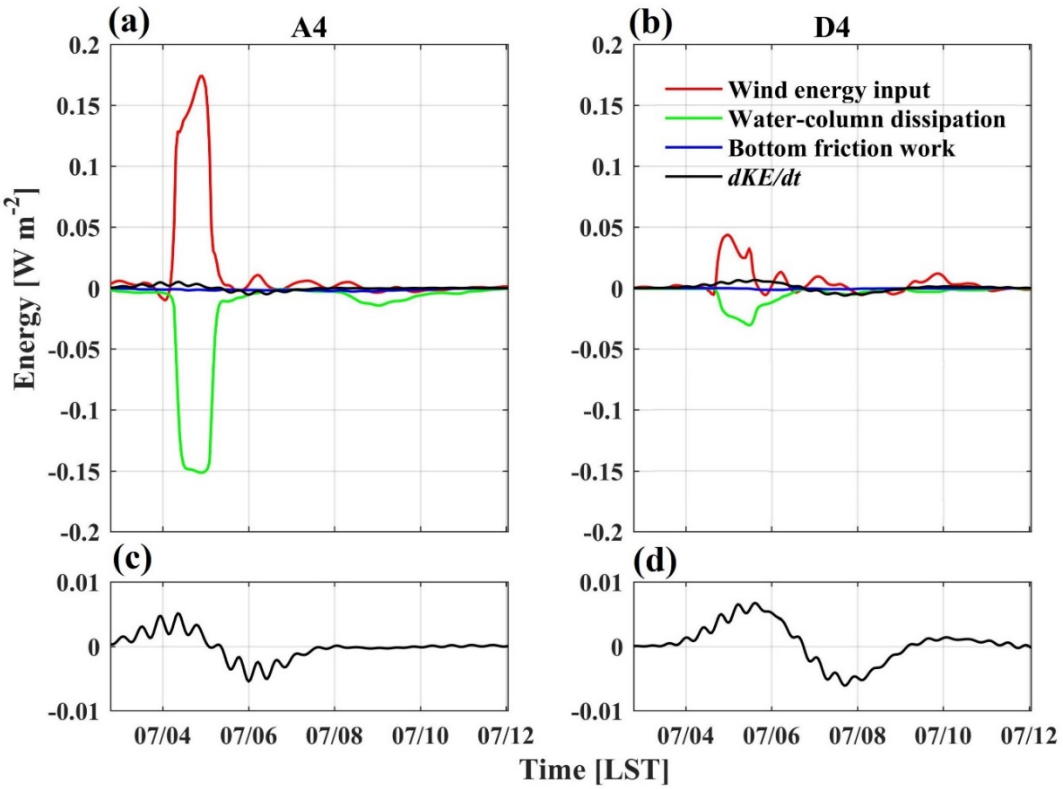

Figure 3.10 Wind energy input (red), the depth-integrated water-column dissipation of NICs kinetic energy (ε, green), bottom friction work (blue), and depth-integrated d*KE*/d*t* averaged over the inertial period for (a) A4 and (b) D4. Zoomed-in view of *dKE/dt* for (c) A4 and (d) D4.

3.4.3 Vertical modal structure

The glider deployed in the inner shelf off the New Jersey Coast observed two-layer baroclinic currents during the passage of Hurricane Arthur (Figures 3.4e and 3.4g). The FVCOM model reproduced this two-layer current structure that oscillated at the local inertial frequency (~ 19 hours) (Figures 3.4f and 3.4h). Both the amplitude and phase of the observed current fluctuations were reasonably simulated. The model also captured the observed two-layer stratification, with the warm surface water separated from the cold pool water by a sharp thermocline (compare Figures 3.4c-d). However, there were model-data discrepancies. The predicted surface mixed-layer depth prior to Arthur's arrival was about ~8 m, and was shallower than the observed depth of ~13 m. Turbulent closure schemes (such as the k-□ model used in this study) do not fully account for the mixing processes in the surface mixed layer such as Langmuir circulation and breaking waves, and tend to under-predict the mixed-layer depth (e.g., Mellor 2001; Burchard and Bolding 2001; Belcher et al. 2012). Our model was initialized using the outputs from ESPreSSO. While data assimilation in EsPreSSO should significantly reduce the model-data misfit, it is possible that part of our model discrepancies with the observations may have originated from possible misfit in the initial condition. Nevertheless, the model and glider showed similar rates of the mixed-layer deepening and temperature decrease due to the storm-induced entrainment: the mixed layer deepened by 6 m in the model and by 5 m in the glider observations.

To investigate the vertical structure of NICs over the entire MAB shelf, we plot the time-depth distribution of NICs at the stations spaced along the five cross-shelf sections

(Figure 3.11) as indicated in Figure 3.5b. The pycnocline, defined to be the location of maximum density gradient, is added, in order to highlight the connection between the stratification and vertical modal structure of the NICs. A comparison of the current structure between the deep ocean and shelf stations showed a marked difference. Strong NICs in the deep ocean penetrated down to ~100 m and exhibited a vertical profile typical of the NICs observed in deep water (e.g., Sanford et al. 2011). The currents were strongest near the ocean surface and decayed with depth. In contrast, the NICs on the shelf displayed a two-layer baroclinic structure. The upper- and lower-layer currents were separated at the pycnocline depth, indicating a mode-1 wave structure.

The NICs were weakest near the coast and got stronger in the offshore direction. This result is in agreement with Pettigrew's (1981) theoretical prediction based on a linear, two-layer, flat bottom, cross-sectional model with a coastal wall boundary. He showed that a mode-1 current structure developed on the shelf and the current magnitude increased away from the coast. In addition to this strong cross-shelf variation, the detailed vertical structure of NICs varied among the stations and appeared to be set mainly by the vertical stratification profile. At the shallow sites such as C3-E3 and C4-D4, the surface and bottom layers were of similar depths such that the currents in the two layers were of comparable magnitude even though they always varied out of the phase. At the deeper shelf sites such as B5-E5 and E4, the surface mixed layer was much thinner than the bottom layer. Consequently, the currents were much stronger in the surface layer. Such differences are expected since the ratio of surface to bottom NICs was shown to be inversely proportional to the ratio of the layer depths (Millot and Crepon 1981).

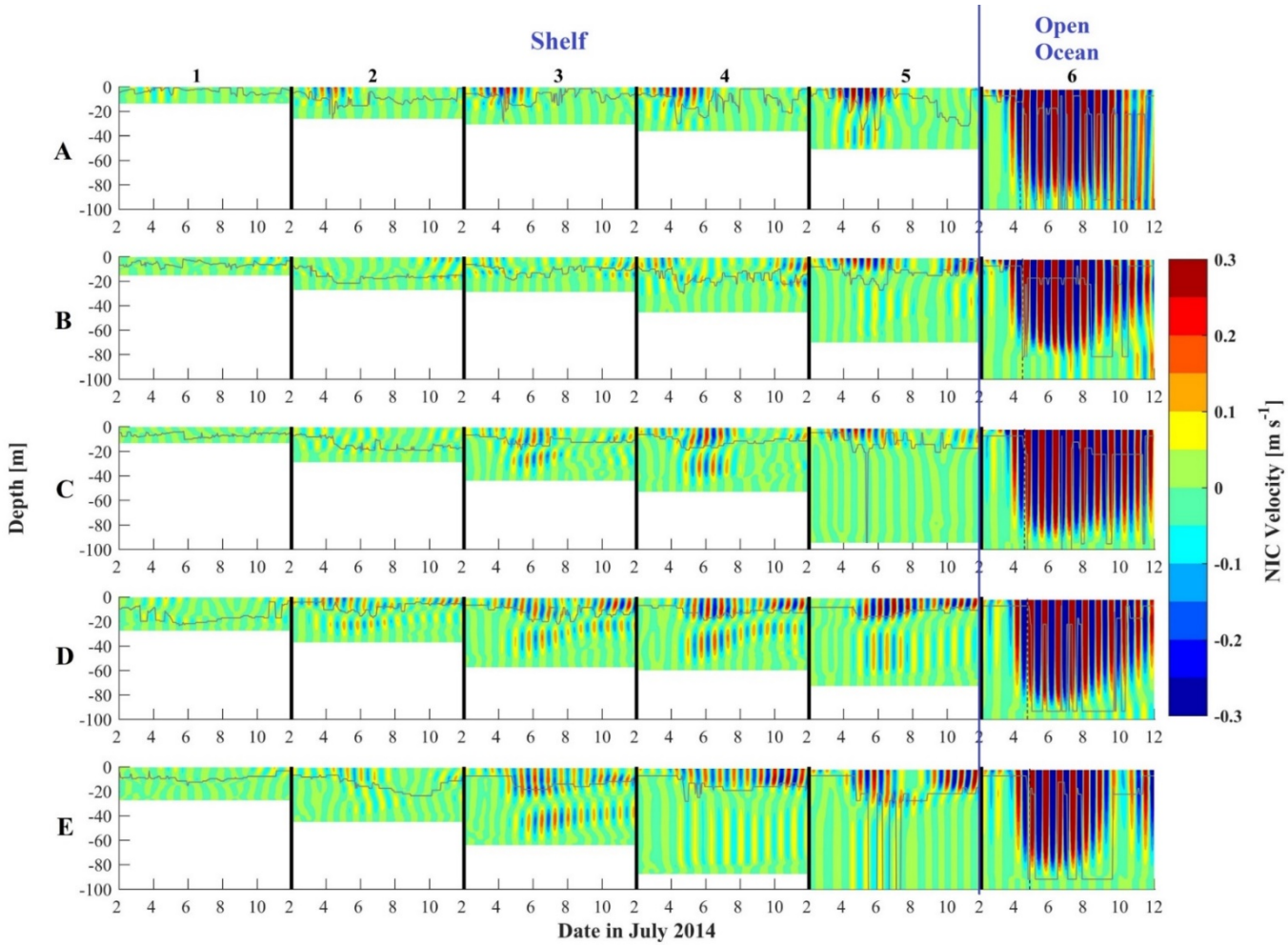

Figure 3.11 Time-depth distributions of NICs (cross-shelf component) along the 5 cross-shelf sections. The black dashed lines in column 6 indicate the passage of the storm's center, and the thin gray lines indicate the depth of maximum density gradient (the pycnocline separating the

Figures 3.4 and 3.11 suggest that most of the NICs on the MAB shelf were mode-1 waves. To provide a quantitative description of the modal structure of the near-inertial waves, empirical orthogonal analysis was performed. The NICs were decomposed to five orthogonal vertical modes. The shape of each mode $\frac{d\psi_n(z)}{dz}$ (n=1 to 5) is determined by the following equation:

$$\frac{\partial^2}{\partial z^2}\psi_n(z) = -[\frac{N^2(z)}{c_n^2}]\psi_n(z) \tag{3.6}$$

where $N(z)$ is buoyancy frequency, c_n is the eigen velocity of each mode, and $\psi_n(z)$=0 at both the ocean surface and the sea floor (e.g., MacKinnon and Gregg 2005; Alford and Zhao 2007). $N(z)$ was averaged between 2 and 12 July. The eigen value and eigen vector of Equation 3.6 are c_n and $\psi_n(z)$ for each vertical mode, respectively. The NICs velocity of each vertical mode was then obtained by fitting NICs vertical profiles to $\frac{d\psi_n(z)}{dz}$ of the first 5 modes with the least squares method, assuming no NICs at higher vertical modes. To assess the energy content in each mode, we calculate the percentage of the NICs kinetic energy in each mode (Figure 3.12):

$$P_n = \frac{<\int_{-H}^{0} KE_n>}{\sum_{n=1}^{5}<\int_{-H}^{0} KE_n>} \times 100\% \tag{3.7}$$

where < > denotes the time-averaging between 2 and 12 July, the numerator denotes the kinetic energy in mode n, and the denominator denotes the sum of the kinetic energy in all the five modes. Overall, mode-1 contained 76% of the total kinetic energy in the near-inertial waves on the MAB shelf, mode-2 accounted for 12% (Figure 3.12), and the remainder was split among the three higher modes (not shown). In the cross-shelf direction, P_1 increased from ~60% in the near-shore region to over 80% near the shelf-break. In the shelf area between the mouths of Chesapeake and Delaware Bays (between 37°N and

38.5°N), P_1 decreased to 50% and P_2 increased to 40%, consistent with previous vertical profiles at B3 and B4 (second row in Figure 3.11).

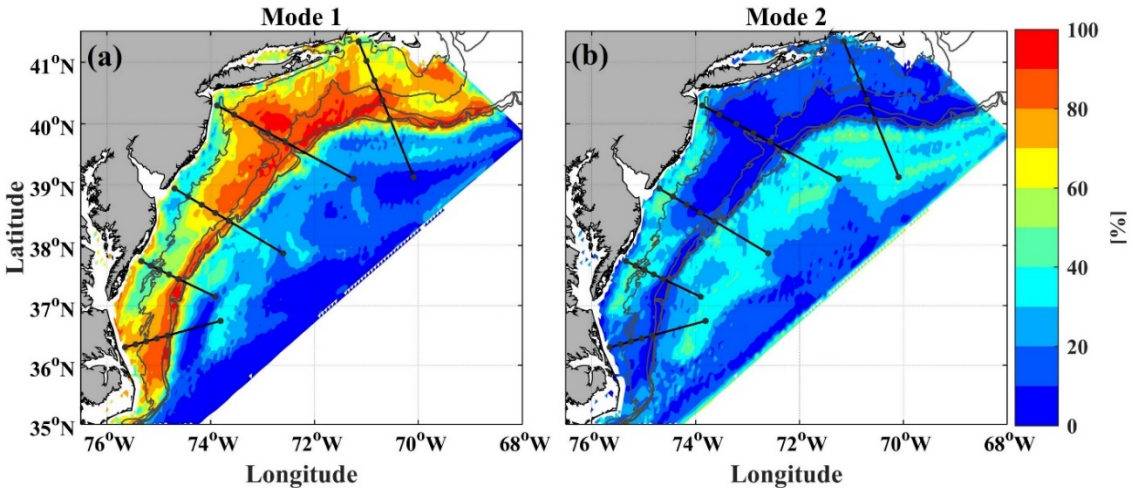

Figure 3.12 Percentage of the NICs kinetic energy in (a) mode-1 and (b) mode-2.

3.5 Conclusion and discussion

This paper presented a combined observational and modeling investigation into the near-inertial waves generated by Hurricane Arthur during its passage over the MAB. Both the HF radars and the numerical model showed that the NICs decreased substantially from the deep ocean to the MAB shelf. Due to the presence of a coastline as well as weaker wind stress away from the storm center, the NICs on the MAB shelf decreased onshore. The glider and the numerical model showed that the NICs had a two-layer baroclinic structure. The mode-1 near-inertial waves contained over 70% of the NICs kinetic energy over the MAB shelf.

Our findings of the mode-1 wave structure and onshore decrease of the NICs amplitude are consistent with previous observations (Shearman 2005; MacKinnon and Gregg 2005) and theoretical predictions (Millot and Crepon 1981; Pettigrew 1981; Kundu et al. 1983). In the mooring records collected in New England shelf, Shearman (2005) found that the mode-1 baroclinic structure was coherent across the entire shelf, with a magnitude that decreased onshore. Using a 2-dimensional linear model of a flat-bottomed shelf, Pettigrew (1981) obtained a solution for the near-inertial currents and found that the mode-1 vertical structure was a result of a surface mixed layer response and barotropic wave emanating from the coastline. He also predicted that the NICs were zero at the coast and increased in the offshore direction.

Most of the NICs differences between the MAB shelf and the deep ocean appear to be related to the asymmetry of the wind energy input between the left and right sides of the storm track. The wind energy input was relatively high in the mid-to-outer shelf region between the New Jersey Coast and New England Shelf, which corresponds to higher *KE* than other shelf areas. In the southern MAB, the time-averaged *KE* was weak even though the wind energy input was large. The analysis of the energy budget showed that the large wind work was quickly balanced by the energy dissipation, which led to the rapid damping of the NICs there. In the northern MAB, however, the energy dissipation lagged the wind energy input such that the NICs persisted. When analyzing the mooring data collected on the New England Shelf, MacKinnon and Gregg (2005) also found that the wave evolution was controlled by the balance among wind stress, bottom drag and turbulent dissipation.

With a predominant mode-1 vertical structure, the strongest shear in the NICs usually coincides with the pycnocline (see Figure 3.11), thus making NICs a potentially important mechanism for generating turbulent mixing on the shelf. We computed the depth-averaged shear spectra at two stations: station A2 in the inner shelf of southern MAB; station D4 in the mid-shelf (Figure 3.13). At A2 where the storm center was closest to the coast, the highest peak is found around 1 day^{-1} frequency and is probably related to the strong wind-driven longshore currents. However, at D4 the NICs were the largest contributor to the shear spectrum. Figure 3.14 shows the ratio of the NICs-induced shear to the total current shear over the entire model domain. In the deep ocean, the NICs-induced shear accounted for over 80% of the total shear. On the MAB shelf, the NICs accounted for 60-80% of the shear on the New England shelf and 30-50% farther south on the MAB. The NICs only contributed to about 20% of the total shear in the inner shelf region off the Outer Banks. Since turbulent mixing may cool the surface mixed layer and affect the storm intensity, it would be worthwhile to investigate the role of the NICs in generating mixing in a future study.

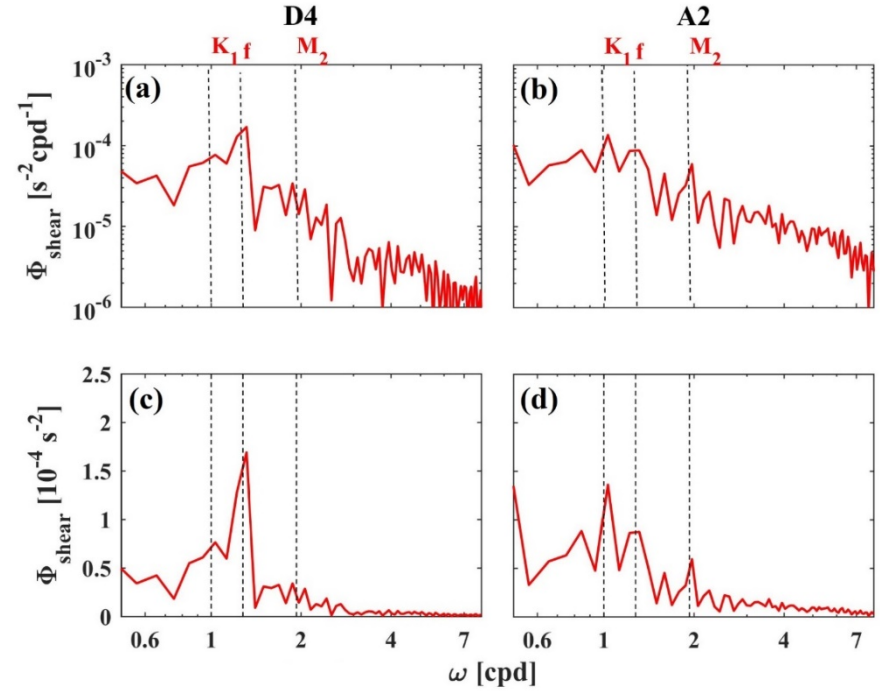

Figure 3.13 Depth-averaged shear spectra/variance-preserving spectra at (a)/(c) D4 and (b)/(d) A2.

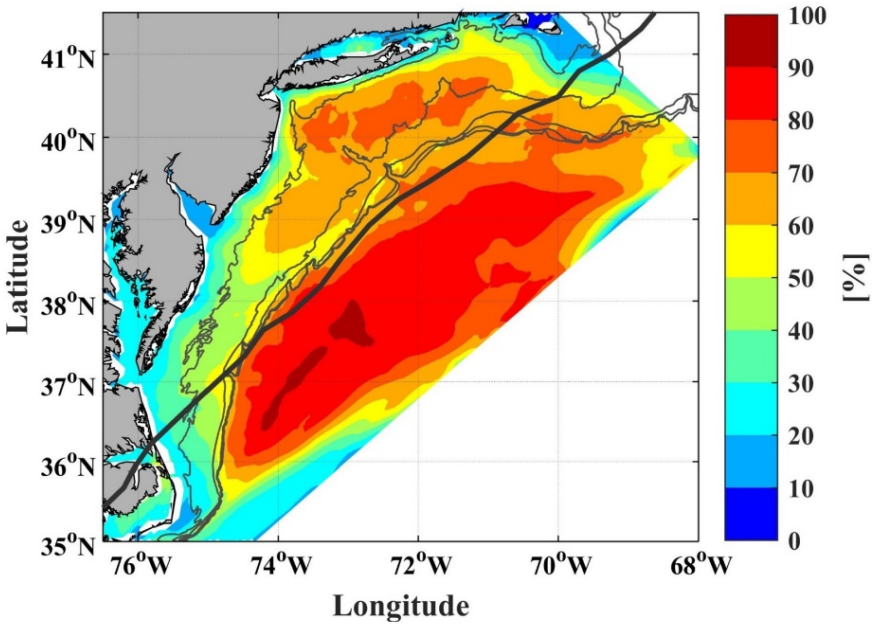

Figure 3.14 Percentage of the depth-averaged NICs-induced shear.

3.6 Acknowledgements

Funding support was provided by Maryland Sea Grant (NA14OAR4170090, SA75281450-H) and the NOAA Cooperative Institute for the North Atlantic Region (CINAR, NA13OAR4830233), Disaster Recovery Act. Fan Zhang is supported by Maryland Sea Grant Fellowship and Travis Miles was supported by Teledyne Webb Research Graduate Fellowship. Suggestions from Xiaohui Xie are greatly appreciated. We thank the two reviewers for their helpful comments. HF radar data can be downloaded from http://tds.marine.rutgers.edu/thredds/catalog/cool/codar/totals/5Mhz_6km_realtime_fmrc/catalog.html?dataset=cool/codar/totals/5Mhz_6km_realtime_fmrc/Maracoos_5MHz_6km_Totals-FMRC_best.ncd. The glider data and WRF-FVCOM model outputs are available at https://zenodo.org/record/1208153#.WrpnTYjwZPZ. This is UMCES contribution number 5484.

CHAPTER 4

IMPACT OF CLIMATE CHANGE ON STORM SURGE

Preface

This chapter is a reproduction of work published in the Journal of Geophysical Research: Oceans with coauthor Ming Li. The right to reuse this work was retained by the authors when publication rights and nonexclusive copyright were granted to the American Geophysical Union.

Zhang, F., and M. Li, (in prep): Impact of Climate Change on Storm Surge in Chesapeake Bay. Journal of Geophysical Research: Oceans.

4.1 Introduction

Storm surge induced by tropical cyclones poses great threats to densely populated coastal areas. Meanwhile, with predicted warmer ocean and storm intensification, and sea level rise in the future (e.g., Elsner et al. 2008; Rahmstorf 2012; Church et al. 2014; Jevrejeva et al. 2016), increased storm surge hazard is expected (e.g., Tebaldi et al. 2012; Reed et al. 2015; Lin et al. 2016).

The Intergovernmental Panel on Climate Change fifth assessment report (IPCC AR5) estimated 1-3^{o}C increase of globally-averaged sea surface temperature (SST) by the end of 21st century based on different representative concentration pathways (RCPs), with significant spatial variability among different basins (Collins et al. 2013). Tropical Atlantic Ocean, which nurtures most landfalling tropical cyclones in the U.S. east coast, is predicted to experience 1.6^{o}C warming under RCP 4.5, and 3.3^{o}C warming under RCP 8.5 by the end of this century based on the ensemble mean of 17 climate models (Villarini and Vecchi 2012). The warming climate suggests an increase in tropical cyclone intensity on the basis of both theories (e.g., Emanuel 1987; Holland 1997) and numerical evidences (e.g., Emanuel et al. 2008; Bender et al. 2010; Knutson et al. 2010; Villarini and Vecchi 2013). The warming ocean also leads to thermal expansion of seawater, which contributes to approximately 50% of global sea level rise according to IPCC AR5 (Church et al. 2013). In concert with other contributors inclusive of melting of glaciers and ice sheets, and changes in anthropogenic land water storage, the predicted global mean sea level rise by 2100 ranges from 0.53 m under RCP 4.5 and 0.74 m under RCP 8.5 (Church et al. 2013). Moreover, regional dynamics can affect local relative sea level rise as well. For instance,

in Chesapeake Bay region, the predicted weakening of Atlantic Meridional Overturning Current, of which the Gulf Stream is a crucial portion, and land subsidence associated with glacial isostatic adjustment can further increase 2100 sea level by 0.17 m and 0.15 m, respectively, amounting to ~1 m relative sea level rise (Yin et al. 2010; Engelhart et al. 2011; Ezer et al. 2013; Kopp 2013; Miller et al. 2013; Yin and Goddard 2013; Boesch et al. 2013; Rahmstorf et al. 2015).

Several studies have described how storm surge will change under these climate variabilities for different regions (e.g., Lowe et al. 2001; Lowe and Gregory 2005; Mousavi et al. 2011; Lin et al. 2012). Lowe et al. (2001) and Lowe and Gregory (2005) configured a regional hydrodynamic model for U.K. coast, which is continuously forced by Hadley Centre regional climate model from the beginning of industrial evolution to the end of 21st century. They found a sizeable proportion of U.K. coast will witness over 0.2 m higher 50-year return period surge by 2100. Given the computational expense for large model domain and century-long integration, the atmosphere and ocean model resolutions were limited to 35 and 50 km, respectively. Considering the size of the storm core (~5 km) and breadth of estuaries in U.K. (~ 20 km), storm dynamics and estuary scale surge were not well captured as indicated in their surge validation under present climate. To reconcile the computational cost and accuracy, a hybrid method was developed by Lin et al. (2012) to study changing surge in New York City. They coupled a parametric hurricane model which was driven by general circulation model (GCM) statistics (statistical/deterministic hurricane model, Emanuel et al. 2006; Emanuel et al. 2008) with a coarse resolution hydrodynamic model to identify the extreme surge events as a first step, then applied a high resolution (10-1000

m) hydrodynamic model to simulate the selected surge incidents more accurately. Depending on which GCM statistics was adopted, they found the surge height at Battery, New York City, will experience 3% reduction to 50% increase for the main range of the return period. Instead of investigating changes in surge height of specific return period, another approach to inspect the impact of climate change on surge height is to compare snapshots of storm surge between future and present. By downscaling climate model results at 2030/2080 to Corpus Christi Bay, Texas, Mousavi et al. (2011) prescribed 0.375/0.75 m sea level rise in the hydrodynamic model. Moreover, they hypothesized revisits of three historical tropical cyclones, and parameterized them with previous tracks, forward speeds, sizes, but stronger intensities increased linearly with $1^{o}/2.5^{o}$C higher SST. They found 17/26% increase in surge height in 2030/2080, and the increase in the downwind portion of the bay is significantly larger than that in the opposite side.

Idealized experiments were also performed to identify individual contribution of storm intensification and sea level rise to surge change (e.g., Lowe et al. 2001; Smith et al. 2010; Mousavi et al. 2011; Lin et al. 2012). While storm intensification leads to higher surge in all studies, diverse responses of surge height to sea level rise were observed. Along the U.K. coast and at Battery, New York City, sea level rise shows little impacts on surge height (Lowe et al., 2001; Lin et al., 2012). In Corpus Christi Bay, sea level rise results in 10% reduction in surge heights in shallow bay area (bathymetry: ~3.5 m), but has negligible effect in relatively deeper coastal region (bathymetry: ~30 m). By contrast, Smith et al. (2010) found substantial increase of peak surge height in Southeast Louisiana given 1 m sea level rise. The increase of surge height ranges from 1-3 m in wetland or wetland-fronted

areas to 5 m in isolated areas. These diverse responses of surge height to sea level rise imply the underlying physics is non-linear and caution that site-specific investigation is necessary when evaluating impacts of climate change on storm surge.

In this study, we investigate the impacts of climate change on storm surge in Chesapeake Bay. Following a similar approach as Mousavi et al. (2011), we use Hurricane Isabel (2003) as an example and compare the predicted surge in 2050/2100 with hindcast. Instead of using parametric winds, a high-resolution weather and research forecasting model (WRF; Skamarock et al. 2008) is used to resolve the storm intensification under warmer SST more realistically. Hurricane Isabel brought over 2 m storm surge to Chesapeake Bay on 18-19 September 2003, which is the highest in the recent decades, owing to its uncommon track west of the bay along with strong up-estuary winds (Pore 1965; Li et al. 2006; Shen et al. 2006). Thus, it is well-suited for worst-case scenario study.

Moreover, Chesapeake Bay borders the surrounding highly populated states including several metropolitan cities (e.g., Washington D.C., Baltimore, Maryland, Norfolk, Virginia) with vast low-lying areas. Hardened shoreline was built to protect diminishing lands in this region (Schulte et al. 2015). Given a sizable proportion of these low-lying areas have elevations lower than predicted 1 m relative sea level rise in 2100, more seawall construction is expected in this region. Despite the provided protection, hard shorelines can also reduce possible pathways for storm water and may enhance surge. A quantitative study is thus needed to evaluate the impact of hard shoreline to surge height in Chesapeake Bay.

This paper is organized as follows: Section 2 describes model configurations and experimental design; Section 3 summarizes model results; Section 4 explores the impact of each factor (i.e., warmer SST, sea level rise, and hard shoreline) on storm surge with energy budget equation; and the final section presents discussion and conclusion.

4.2 Methods

4.2.1 Model configuration

To examine storm surge variations in Chesapeake Bay under climate change, we use the Advanced Research WRF model to simulate tropical cyclone dynamics in the atmosphere, and Finite Volume Community Ocean Model (FVCOM; Chen et al. 2003) to simulate storm surge in Chesapeake Bay. In this atmosphere-ocean model system, FVCOM is forced by hourly surface winds from WRF. The inverse barometer effect was estimated to be negligible for Isabel-induced surge in Chesapeake Bay and is not considered in this study (Zhong et al. 2010).

We have configured triple-nested model domains for WRF (Figure 4.1a). The outermost domain has a resolution of 12 km and covers a significant proportion of western Atlantic to support ramping up of storm vortex before landfall. The 4-km middle domain and 1.33-km innermost domain are placed over Mid-Atlantic Bight and Chesapeake Bay, respectively, to provide high resolution wind forcing for the hydrodynamic model. In the vertical direction, 40 sigma levels are used. WRF is initialized on 1900 LST 16 September 2003, approximately 2 days before the landfall of Isabel in North Carolina, and ended on 1900 LST 20 September 2003, after Isabel exited the study area. The initial and lateral

boundary conditions are from 6-hourly Final (FNL) operational global analysis data with 1° resolution (https://rda.ucar.edu/datasets/ds083.2/), and the bottom boundary condition is from daily real-time global SST (RTG-SST, http://polar.ncep.noaa.gov/sst/rtg_low_res/) with 0.5° resolution. In terms of parameterization schemes for sub-grid scale physics, the Thompson scheme is used for microphysics (Thompson et al. 2008), the rapid radiative transfer model is used for both shortwave and longwave radiations (Iacono et al. 2008), the Yonsei University scheme is used for planetary boundary layer (Hong et al. 2006), the Kain-Fritsch scheme is used for cumulus parameterization (Kain 2004), and the MM5 similarity is used for surface layer physics (Fairall et al. 2003).

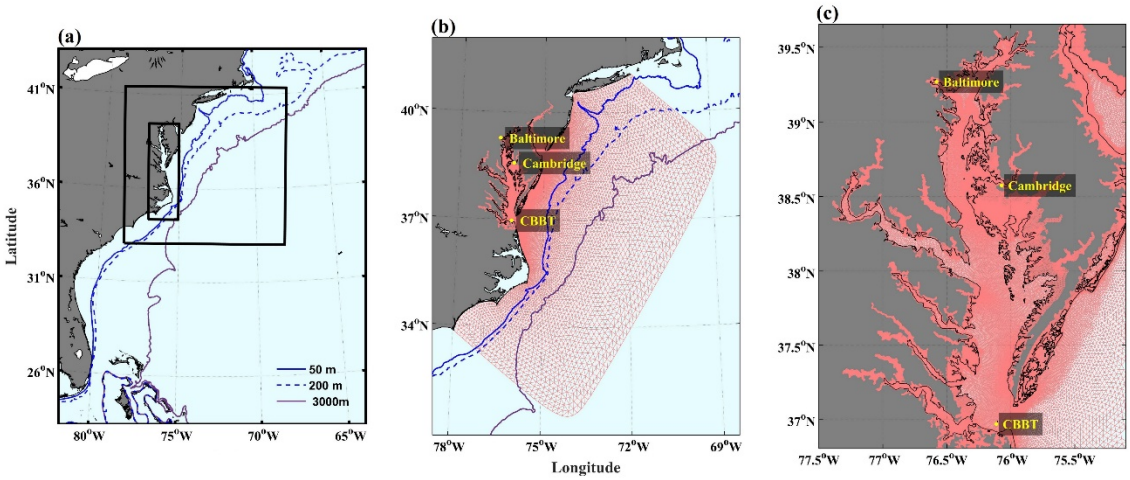

Figure 4.1 (a) Triple-nested WRF model domains with resolutions of 12, 4, and 1.33 km. (b) FVCOM model grids (red). (c) Zoomed-in view of FVCOM grids for Chesapeake Bay.

A 3-dimensional version of FVCOM is used to configure a coupled estuary-shelf model in this study. The model domain covers Chesapeake Bay, Delaware Bay, and adjacent shelf (Figure 4.1b). The open boundary is placed over 300 km away from Chesapeake Bay mouth to fully capture the incoming surge. Additional ~100,000 grids with resolution of 80-200 m are placed for low-lying areas around Chesapeake Bay (up to

5-m above the mean sea level) to capture flooding induced by relative sea level rise and storm surge (Figure 4.1c). In the vertical direction, 5 sigma layers are used. The bathymetry/elevation data is from National Oceanic and Atmospheric Administration (up to 3 arc second resolution) and U.S. Geological Survey (up to 10 m resolution), and a detailed description can be found in Lee et al. (2017). FVCOM simulation starts from 1900 LST 11 September and ends at 1900 LST 20 September. Uniform temperature (25^{o}C) and salinity (35 PSU) for the entire model domain are kept constant throughout the simulation. Bottom roughness height is set to be 10 mm for Chesapeake Bay and 20 mm for the adjacent shelf (Xu et al. 1994; Churchill et al. 1994). In the open boundary, the model is forced by 10 tidal constituents (M_2, S_2, N_2, K_2, K_1, O_1, P_1, Q_1, M_f, M_m) from the Oregon State University global tidal model TPXO 7.1 (Egbert and Erofeeva 2002). Preliminary experiment shows the impact of river discharge is small on storm surge during Isabel and thus neglected.

4.2.2 Experimental design

An estimation of regional climate change by 2050 and 2100 in Chesapeake Bay is summarized in Table 4.1. Two RCPs from IPCC AR5 are used here: the middle emission scenario RCP 4.5, and the high emission scenario RCP 8.5. The estimated SST increase is based on Villarini and Vecchi (2012) who summarize results of 17 climate models from fifth Coupled Model Intercomparison Project (CMIP5). The SST increase in tropical Atlantic Ocean ranges from 0.75 to 2.75^{o}C for 2050, and from 1.02 to 4.43^{o}C for 2100. The estimated relative sea level rise for Chesapeake Bay includes both global and regional

components as stated in preceding review. The predicted relative sea level rise spans from 0.33 to 0.57 m for 2050, and from 0.62 to 1.34 m for 2100.

Table 4.1 Projected SST increase in tropical Atlantic Ocean and relative sea level rise in Chesapeake Bay. The projected SST increase is based on Figure 1 of Villarini and Vecchi (2012) which summarizes 17 global climate models under CMIP5 scenarios. Estimation of relative sea level rise in Chesapeake Bay is based on global mean sea level rise from Table 13.5 of IPCC 2014 report, rates of sea level rise due to regional ocean dynamics from Yin et al. (2009), and regional vertical land movement data from Boesch et al. (2013).

	RCP 4.5			RCP 8.5		
2050	mean	min	max	mean	min	max
SST increase in North Atlantic Ocean (ºC)	1.15	0.75	1.97	1.45	0.98	2.75
Relative sea level rise (m)	0.43	0.33	0.52	0.47	0.36	0.57
2100						
SST increase in North Atlantic Ocean (ºC)	1.59	1.02	2.63	3.25	2.38	4.43
Relative sea level rise (m)	0.85	0.62	1.07	1.06	0.78	1.34

To account for storm intensification by warmer ocean in the future, the predicted SST increase is superimposed to RTG-SST. A total of 12 WRF simulations are set up with these warmer SSTs in representation of different future projections. In the ocean part, the predicted relative sea level rises are prescribed at the open boundary of FVCOM, surface winds from corresponding WRF simulations are used to prescribe surface momentum flux. To investigate the impact of hard shoreline on storm surge, two extreme conditions are considered: one with no hard shorelines and the other with hard shorelines along the entire Chesapeake Bay. Therefore, we run a total of 24 FVCOM storm tide simulations. Similar

to Lowe et al. (2001), additional 24 astronomical tidal simulations which include sea level rise and soft/hard shoreline are done, and storm surges in the following sections are the differences between these two sets of runs.

4.3 Results

In this section, we describe Hurricane Isabel, Isabel-induced storm surge, and Isabel-induced maximum water level in Chesapeake Bay in 2003, 2050, and 2100. The hindcast (i.e. 2003) results (Figures 4.2a and 4.2c, Figures A1 and A2, and Table A1) compare favorably with observations and suggest the model is robust. Comparisons between future predictions and hindcast are then made to discern the changes. While we focus on results from 'mean' projections, results from 'min' and 'max' projections provide useful lower and upper bounds (Table 4.1).

4.3.1 Hurricane Isabel under present and future climate

In 2003, Hurricane Isabel started to divert northwestward towards Mid-Atlantic on 17 September with a minimum sea level pressure (MSLP) of 957 mb and a maximum sustained wind speed (MSW) of 48 m s^{-1} (MSLP and MSW are used to indicate storm intensity). The intensity was held until its landfall at Drum Inlet, North Carolina, at 1200 LST 18 September. A rapid weakening process was observed after the landfall and the MSLP/MSW increased/decreased by 20 mb/30 m s^{-1} within 24 hours. Meanwhile, Isabel translated from North Carolina, U.S. to Canada, positioned Chesapeake Bay east of its track. Finally, at the beginning of 20 September, Isabel was absorbed by extratropical low (Beven and Cobb 2004).

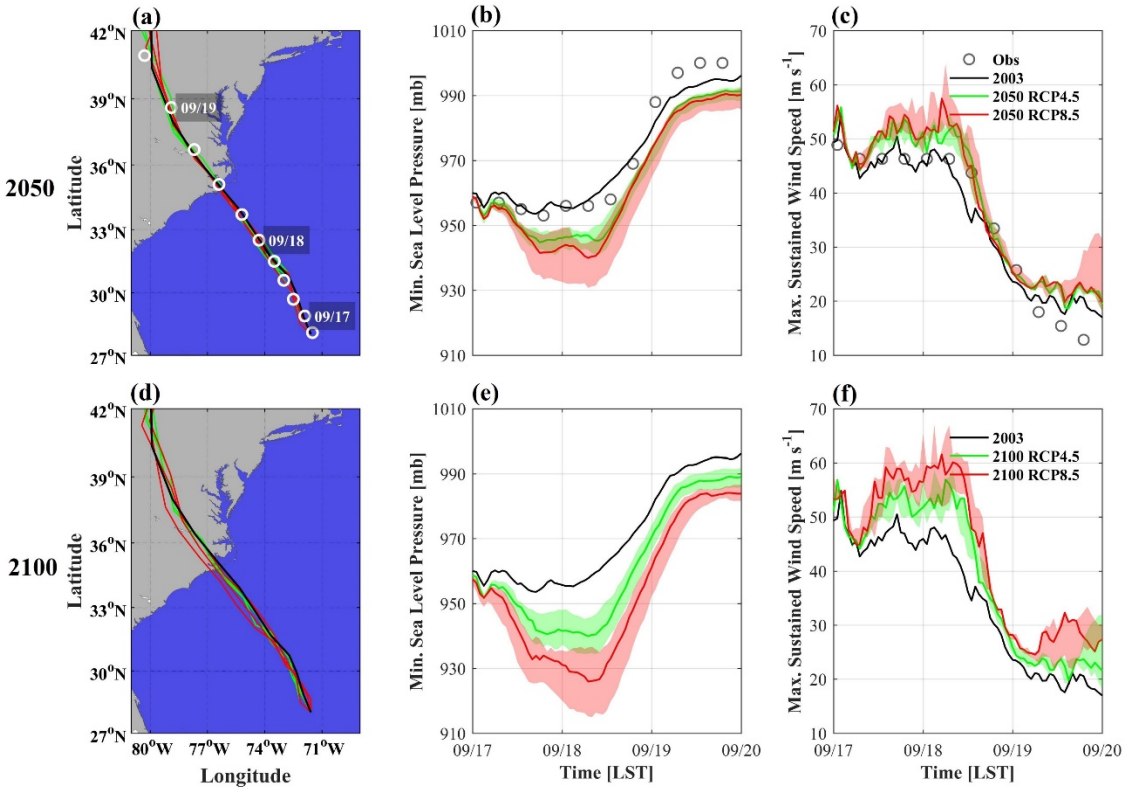

Figure 4.2 (a) Storm track, (b) minimum sea level pressure (MSLP), and (c) maximum sustained wind speed (MSW) for hindcasted Isabel in 2003 (black) and predicted Isabel in 2050 (green and red). (d)-(f), same as (a)-(c), but for Isabel in 2100. The shaded green (red) areas in the right two columns are the envelope of MSLP and MSW of Isabel from all RCP 4.5 (RCP 8.5) scenarios including min, mean, and max in Table 4.1. The solid green (red) lines are results from mean RCP 4.5 (RCP 8.5) scenarios.

In 2050, the storm track of Isabel shows very limited changes compared to hindcast given same initial and lateral boundary conditions (Figure 4.2a). Forced by SST of RCP 4.5, the decrease in minimum MSLP is 8 mb, and the increase in MSW is around 5 m s^{-1} compared to hindcast (Figures 4.2b and 4.2c). Conceivably, more pronounced intensification is observed in RCP 8.5 which has higher SST: the decrease in minimum MSLP is 13 mb and the increase in MSW is around 7 m s^{-1}. In 2100, with even higher SSTs, the storm tracks show slightly westward drift (Figure 4.2d). Compared with hindcast, in RCP 4.5, the decrease in minimum MSLP is 13 mb and increase in MSW is around 8 m s^{-}

^{1}; and in RCP 8.5, the decrease in minimum MSLP is 25 mb and the increase in MSW is around 12 m s^{-1} (Figures 4.2e and 4.2f).

4.3.2 Storm surge under present and future climate

To examine changes of storm surge in Chesapeake Bay under future climate and capture possible diverse responses in different parts of the bay, three tidal gauge stations are chosen: Chesapeake Bay Bridge Tunnel (CBBT), Virginia, for the lower bay, Cambridge, Maryland, for the middle bay, and Baltimore, Maryland, for the upper bay. Their locations are marked in Figure 4.1.

In 2003, Isabel made landfall south of Chesapeake Bay mouth around 1200 LST 18 September. Meanwhile, the westward winds ahead of the storm drove shelf water inside the bay and raise the water level in the lower bay. At CBBT, the storm surge peaked at 1.39 m at 1600 LST 18 September as a result of the continuous westward wind forcing (Figure 4.3). Following this peak surge, Isabel moved north of CBBT and winds became northward or northeastward in Chesapeake Bay. Concurrently, a rapid fall of storm surge was observed at CBBT which reduced the surge height from 1.39 m to zero within 6 hours. In tandem to the surge reduction in the lower bay, building surges were observed at Cambridge and Baltimore. The peak surge (1.63 m) at Cambridge occurred at 0500 LST 19 September, succeeded by a 2.25 m peak surge at Baltimore in 2 hours (Figures 4.4 and 4.5). After the peak surges, in contrast to the fast-falling surge at Baltimore, the surge at Cambridge experienced a slower decline. Particularly, the surge height stalled between

1100 and 1300 LST 19 September. This is due to eastward winds behind the storm drove water from main stem of the bay to the eastern shore where Cambridge situates.

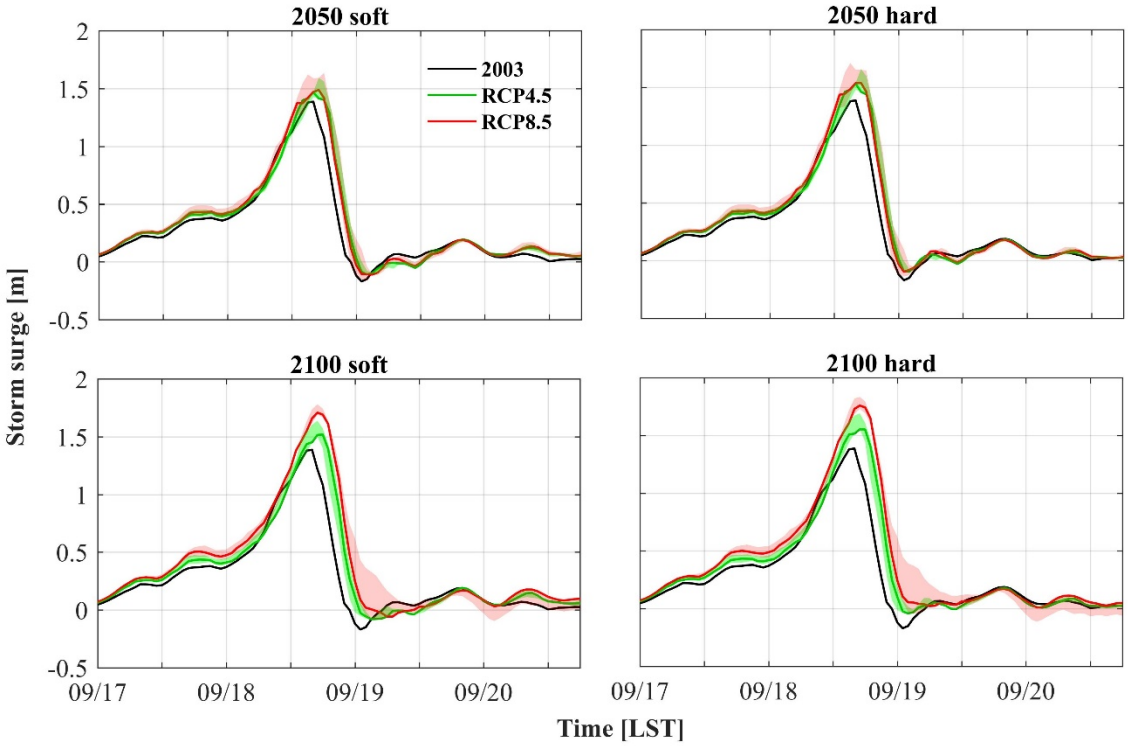

Figure 4.3 Storm surge (de-tided, referenced to the mean sea level in corresponding climate projection) time series for Chesapeake Bay Bridge Tunnel (CBBT), Virginia. The thick green and red lines represent 'mean' scenario and the shaded areas are bounded by results from 'min' and 'max' scenarios.

In 2050, two idealized shoreline protection scenarios are considered as aforementioned: one with no hard shoreline completely (hereafter: soft shoreline) and the other with hard shoreline for the entire bay (hereafter: hard shoreline). Compared to hindcast, with soft shoreline, the peak surge height increases by 0.08 m at CBBT, decreases by 0.06 m at Cambridge, and increases by 0.13 m at Baltimore for RCP 4.5; or increases by 0.1 m at CBBT, is the same at Cambridge, and increases by 0.13 m at Baltimore for RCP 8.5. With hard shoreline, the peak surge height increases by 0.14 m at CBBT, 0.22 m

at Cambridge, and 0.43 m at Baltimore for RCP 4.5; or increases by 0.15 m at CBBT, 0.28 m at Cambridge, and 0.45 m at Baltimore for RCP 8.5.

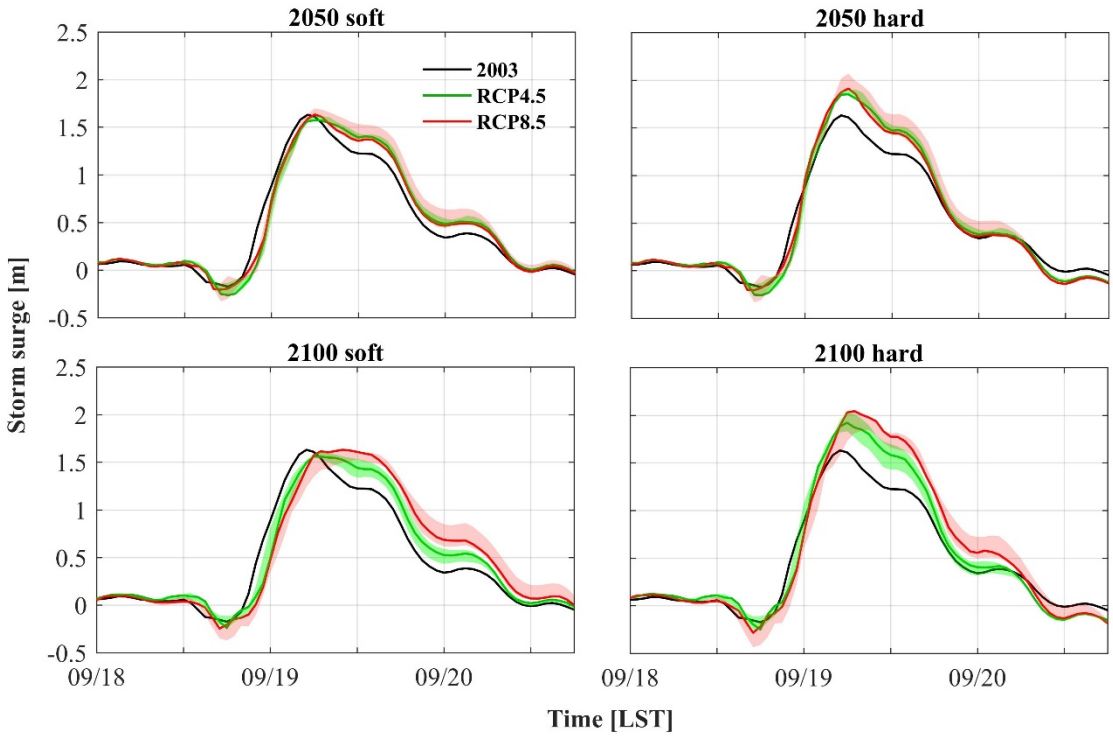

Figure 4.4 Same as Figure 4.3, but for Cambridge, MD.

The two idealized shoreline scenarios are considered for 2100 as well. Comparing 2100 to hindcast, with soft shoreline, the peak surge increases by 0.13 m at CBBT, decreases by 0.07 m at Cambridge, and increases by 0.14 m at Baltimore for RCP 4.5; or increases by 0.32 m at CBBT, is the same at Cambridge, and increases by 0.3 m at Baltimore for RCP 8.5. With hard shoreline, the peak surge increases by 0.16 m at CBBT, 0.29 m at Cambridge, and 0.58 m at Baltimore for RCP 4.5; or increases by 0.37 m at CBBT, 0.41 m at Cambridge, and 0.85 m at Baltimore for RCP 8.5.

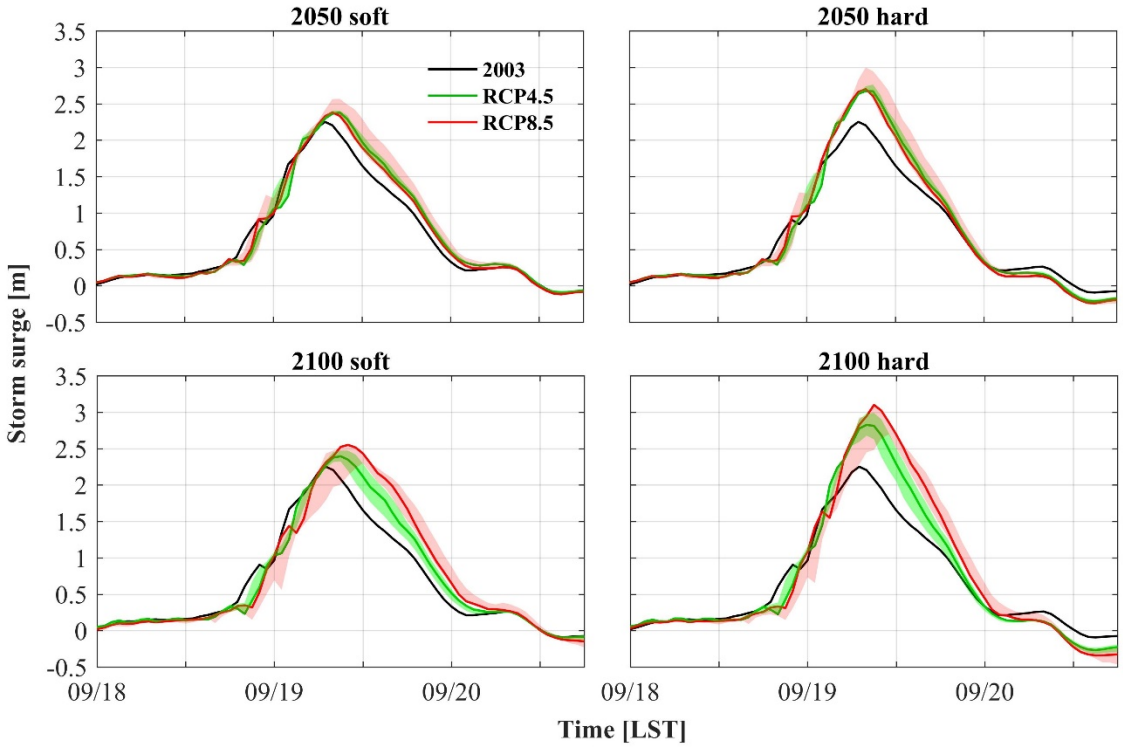

Figure 4.5 Same as Figure 4.3, but for Baltimore, MD.

In summary, with soft shoreline, both lower and upper bay have higher surges, but the middle bay has the same or lower surges compared to hindcast. On the other hand, with hard shoreline, future surges increase through the entire bay, and the increase in surge height grows larger towards upper bay. Overall, hard shoreline scenarios have higher surge than soft shoreline scenarios.

In addition to surge height variations, the timing for peak surge presents divergence among different scenarios as well. The peak surges in future scenarios generally lag those in the hindcast. This is due to the translation speed of Isabel is slower in future scenarios after landfall (Figure A3). Furthermore, the peak surges arrive later with soft shoreline than with hard shoreline in the middle and upper bay. The inclusion of vast inundated area in

soft shoreline scenarios leads to shallower averaged depth for Chesapeake Bay compared to hard shoreline scenarios. Thus, storm surge propagates slower with soft shoreline given the celerity is proportional to square root of water depth.

4.3.3 Maximum water level under climate change

In future scenarios, the aforementioned up to 0.85 m surge height increases are superimposed to relative sea level rise and changing tides. Therefore, total water levels, which include storm surges and tides and are referenced to present mean sea level, experience more increase. Here, we use the maximum value in total water level time series (i.e., maximum water level; MWL) at each location to describe this synthesized water level rise (Figure 4.6).

In 2003, the maximum MWL in Chesapeake Bay occurred in the lower bay tributaries (~3.5 m), given the proximity of this region to storm center. The MWLs between lower and middle bay were among the lowest, with higher west side (~1.2 m) and lower east side (~0.9 m). Such asymmetry coincides with the northwestward winds during Isabel's passage. Farther north, MWLs increased monotonically to ~2.4 m in the upper bay. The flooded area in the western shore of lower bay and eastern shore of middle bay had MWLs ranging from 0.5-1.5 m.

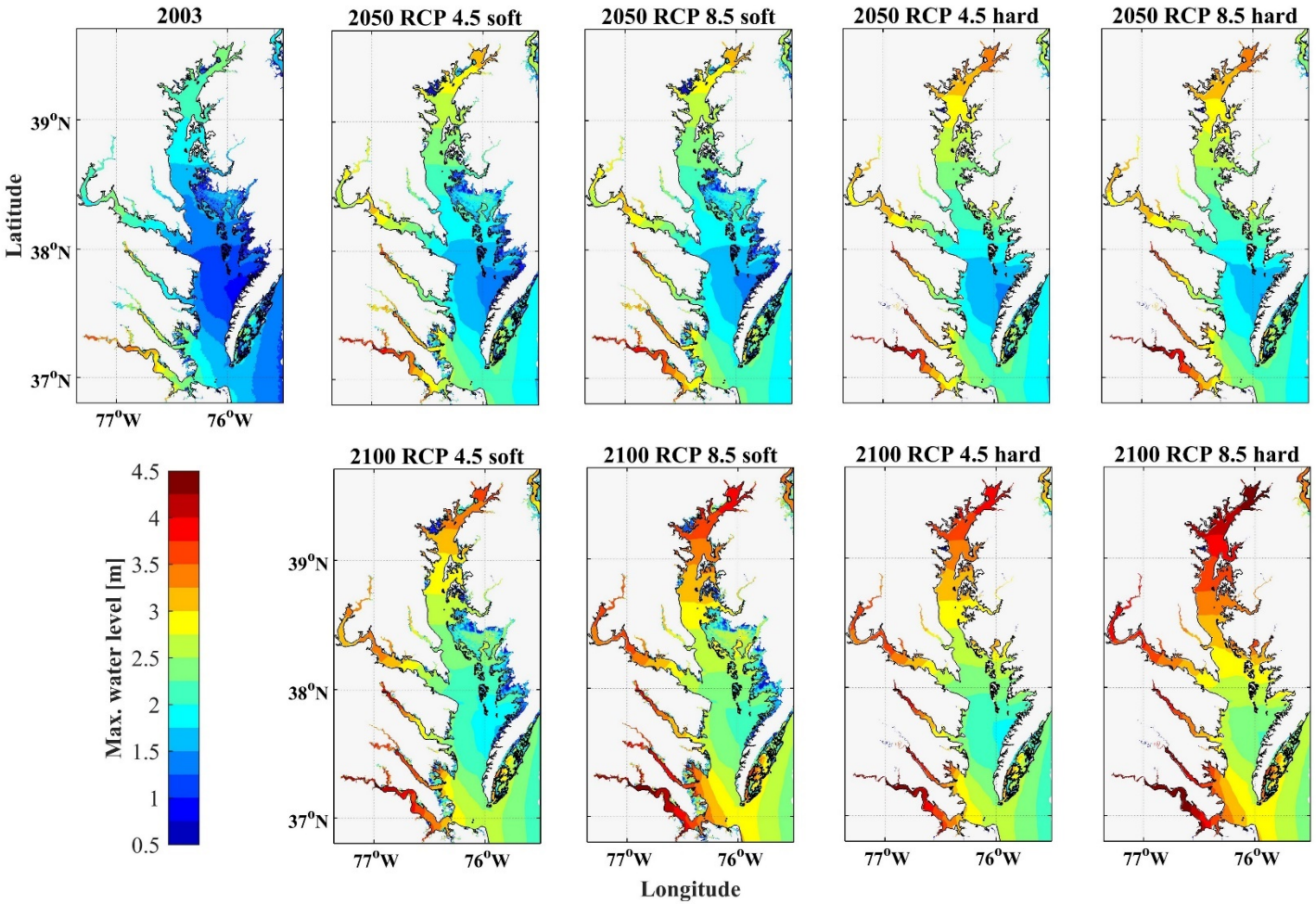

Figure 4.6 Maximum water levels (referenced to present mean sea level/land elevation) during Isabel-like storms from hindcast and future scenarios.

In 2050, the relative sea level rises in RCP 4.5 and RCP 8.5 are both around 0.45 m (Table 4.1). The departure in storm intensities between two scenarios after landfall is also subtle. Conceivably, the MWLs are very similar between these two RCP scenarios. With soft shoreline, the maximum MWL in lower bay tributaries reaches over 4.1 m; the MWLs between lower bay and middle bay increase to ~1.6 m in the west side and ~1.3 m in the east side; and the upper bay has MWLs over 3.1 m. The flooded area in the western shore of lower bay and eastern shore of middle bay are submerged by ~2 m deep water. With hard shoreline, MWLs have additional ~0.05 m increases in the lower bay and ~0.3 m increases in the middle and upper bay compared to soft shoreline scenarios.

In 2100, the relative sea level rise in RCP 8.5 is 0.2 m higher than that in RCP 4.5, and the storm intensity in RCP 8.5 is also significantly stronger. As such, MWLs in RCP 8.5 are ~0.35 m higher than those in RCP 4.5. The hard shoreline further increases MWL by ~0.15 m in the lower bay, and ~0.5 m in the middle and upper bay, compared to soft shoreline scenarios. Therefore, 2100 RCP 8.5 with hard shoreline has the highest MWL among all scenarios: the maximum MWL in the lower bay tributaries is ~5.2 m, MWLs between lower and middle bay ranges from 2.2-2.5 m, and the upper bay has MWLs up to 4.5 m. Moreover, in the soft shoreline scenario, the flooded areas are submerged by ~2.5 m and ~2.7 m depth of water in RCP 4.5 and RCP 8.5, respectively.

In summary, unlike storm surge which may experience reductions in the future (e.g., RCP 4.5 with soft shoreline at Cambridge), MWLs increase under all future scenarios for the entire bay. With soft and hard shoreline, at least 60% and 40% of MWL increases in

Chesapeake Bay are attributed to relative sea level rise, respectively, while changes in storm surge and astronomical tides may contribute to the rest increases.

4.4 Storm surge energetics

The preceding section shows that storm surge will change in the future given warmer SST and storm intensification, and relative sea level rise. Although warming climate and sea level rise have a causal relationship and happen simultaneously, they affect storm surge through different physical processes. To identify their individual contribution to storm surge change in Chesapeake Bay, two additional idealized runs: one with warmer SST only (labeled: 2100 RCP 8.5 soft SST only) and the other with sea level rise only (labeled: 2100 RCP 8.5 soft SLR only) are used. Moreover, the previous section has shown that implementation of hard shoreline can markedly increase storm surge. Therefore, we also compare 2100 RCP 8.5 soft and 2100 RCP 8.5 hard to investigate surge increase attributed to hard shoreline. Storm surge time series from these scenarios at the aforementioned three tidal gauge stations are plotted in Figure 4.7.

The comparison between 2100 RCP 8.5 soft SST only (solid green line) and hindcast (dashed black line) shows that the increase of surge in the future is mostly attributed to warmer SST. The increase in peak surge is substantial in the lower (CBBT) and upper (Baltimore) bay (~0.4 m), but less significant in the middle bay (Cambridge; ~0.1 m). In addition, the ebb of surge at Cambridge is slower compared to hindcast, because of stronger eastward wind behind the storm, and the peak surge level is held for ~12 hours. By comparing 2100 RCP 8.5 soft SLR only (solid blue line) with hindcast, we find the

contribution of sea level rise to surge change is relatively small. Especially, the storm surge time series at CBBT are almost identical between two scenarios. While at the middle and upper bay station, sea level rise reduces peak surge height by ~0.14 m (i.e. ~7% reduction). Finally, with comparison between 2100 RCP 8.5 hard (solid red line) and 2100 RCP 8.5 soft, we find hard shoreline increases peak surge height slightly at CBBT (0.05 m), but substantially at Cambridge (0.41 m) and Baltimore (0.55 m).

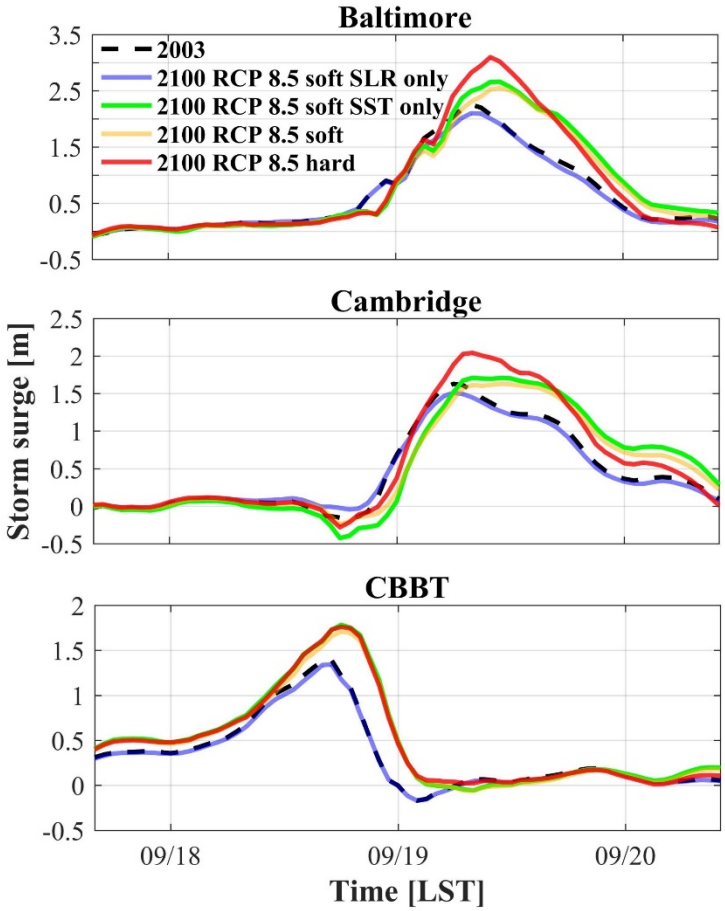

Figure 4.7 Storm surge time series for Baltimore, Cambridge, and CBBT from different scenarios. The black dashed lines represent results from hindcast, the blue lines are for 2100 RCP 8.5 soft SLR only, the green lines are for 2100 RCP 8.5 soft SST only, the yellow lines are for 2100 RCP 8.5 soft with both SLR and SST increase, and the red lines are for 2100 RCP 8.5 hard.

The above comparisons show that storm surge responds to warmer SST, sea level rise, and hard shoreline diversely. This may due to these factors affect storm surge via different physical processes. Here, we adopt the energy equation from Gill (1982) to investigate how each factor affect storm surge. Assuming incompressible fluid with uniform density ρ:

$$\frac{\partial KE}{\partial t} = -\vec{\nabla} \cdot \left[(p' + KE)\vec{u} - \mu \vec{\nabla} \left(\frac{1}{2} \vec{u}^2 \right) \right] - \mu \left[\left(\frac{\partial \vec{u}}{\partial x} \right)^2 + \left(\frac{\partial \vec{u}}{\partial y} \right)^2 + \left(\frac{\partial \vec{u}}{\partial z} \right)^2 \right] \quad (4.1)$$

where kinetic energy $KE = \frac{1}{2}\rho \vec{u}^2$, $\vec{\nabla} = (\frac{\partial}{\partial x}, \frac{\partial}{\partial y}, \frac{\partial}{\partial z})$, p' is pressure perturbation, $\vec{u} = (u, v, w)$ is velocity vector, and μ is viscosity. This equation states that kinetic energy is controlled by divergence of pressure work ($p'\vec{u}$), divergence of kinetic energy advection ($\vec{u}KE$), and viscosity terms. It can be further simplified given the following rationale: horizontal diffusion ($\mu \left(\frac{\partial \vec{u}}{\partial x} \right)^2 + \mu \left(\frac{\partial \vec{u}}{\partial y} \right)^2$) is neglectable compared to vertical diffusion ($\mu \left(\frac{\partial \vec{u}}{\partial z} \right)^2$), and advection of kinetic energy is neglectable compared to pressure work (Cummins and Oey 1997; Zhong and Li 2006). As such, Equation 4.1 becomes:

$$\frac{\partial KE}{\partial t} = -\vec{\nabla} \cdot \left[p'\vec{u} - \mu \vec{\nabla} \left(\frac{1}{2} \vec{u}^2 \right) \right] - \mu \left(\frac{\partial \vec{u}}{\partial z} \right)^2 \quad (4.2)$$

With Divergence Theorem and neglecting small terms which include horizontal shear, integrating Equation 4.2 over the control volume (V) bounded by present Chesapeake Bay shoreline, bay mouth, and corresponding mean sea level yields:

$$\iiint_V \frac{\partial KE}{\partial t} dV = \iint_{S1} p'(u, v) \cdot \overrightarrow{n_1} \, dS - \iint_{S2} p'(u, v) \cdot \overrightarrow{n_2} \, dS - \iint_{S3} p' w_0 dS +$$

$$\iint_{S3} \overrightarrow{u_s} \mu \left(\frac{\partial \overrightarrow{u_s}}{\partial z} \right) dS + \iint_{S3} \overrightarrow{u_b} \mu \left(\frac{\partial \overrightarrow{u_b}}{\partial z} \right) dS - \iiint_V \mu \left(\frac{\partial \vec{u}}{\partial z} \right)^2 dV \quad (4.3)$$

where S1 is the bay mouth cross-section and $\overrightarrow{n_1}$ is its normal vector pointing inside the bay, S2 is other lateral boundary along the present Chesapeake Bay shoreline and $\overrightarrow{n_2}$ is the

corresponding normal vectors pointing landward, S3 is present bay surface, w_0 is vertical velocity at surface, and $\overrightarrow{u_s}$ and $\overrightarrow{u_b}$ are surface and bottom velocities, respectively. The left-hand side describes the rate of change for kinetic energy within the control volume (*dKEdt*). On the right-hand side, the first term represents the incoming energy flux from adjacent shelf through bay mouth ($Flux_{mouth}$), and the second term represents energy flux through present shoreline towards flooded area ($Flux_{flood}$). The third term can be rewritten as $\oiint_{S3} \frac{\partial \frac{1}{2}\rho g \eta^2}{\partial t} dS$ given hydrostatic assumption $p' = \rho g \eta$, where η is free surface elevation, and $w_0 = \frac{\partial \eta}{\partial t}$ (small advection terms are neglected). Moreover, since potential energy $PE = \int_{-H}^{\eta} \rho g z \, dz$, where H is bathymetry, the third term can be interpreted as the rate of change for potential energy ($dPEdt = \oiint_{S3} \frac{\partial PE}{\partial t} dS$). Furthermore, given wind stress $\overrightarrow{\tau_s} = \mu \frac{\partial \overrightarrow{u_s}}{\partial z}$, and bottom stress $\overrightarrow{\tau_b} = -\mu \frac{\partial \overrightarrow{u_b}}{\partial z}$, the fourth term and fifth term represent wind energy input at surface ($Wind\ Input = \oiint_{S3} \overrightarrow{u_s} \cdot \overrightarrow{\tau_s} dS$) and energy dissipation within bottom log layer, respectively. The latter can be combined with the final term and represents total energy dissipation (*Dissipation*). As such, Equation 4.3 can be rewritten as:

$$dKEdt + dPEdt = Flux_{mouth} - Flux_{flood} + Wind\ Input - Dissipation + Residual \quad (4.4)$$

where *Residual* is the sum of all neglected terms. The time series of each term in Equation 4.4 are plotted in Figure 4.8.

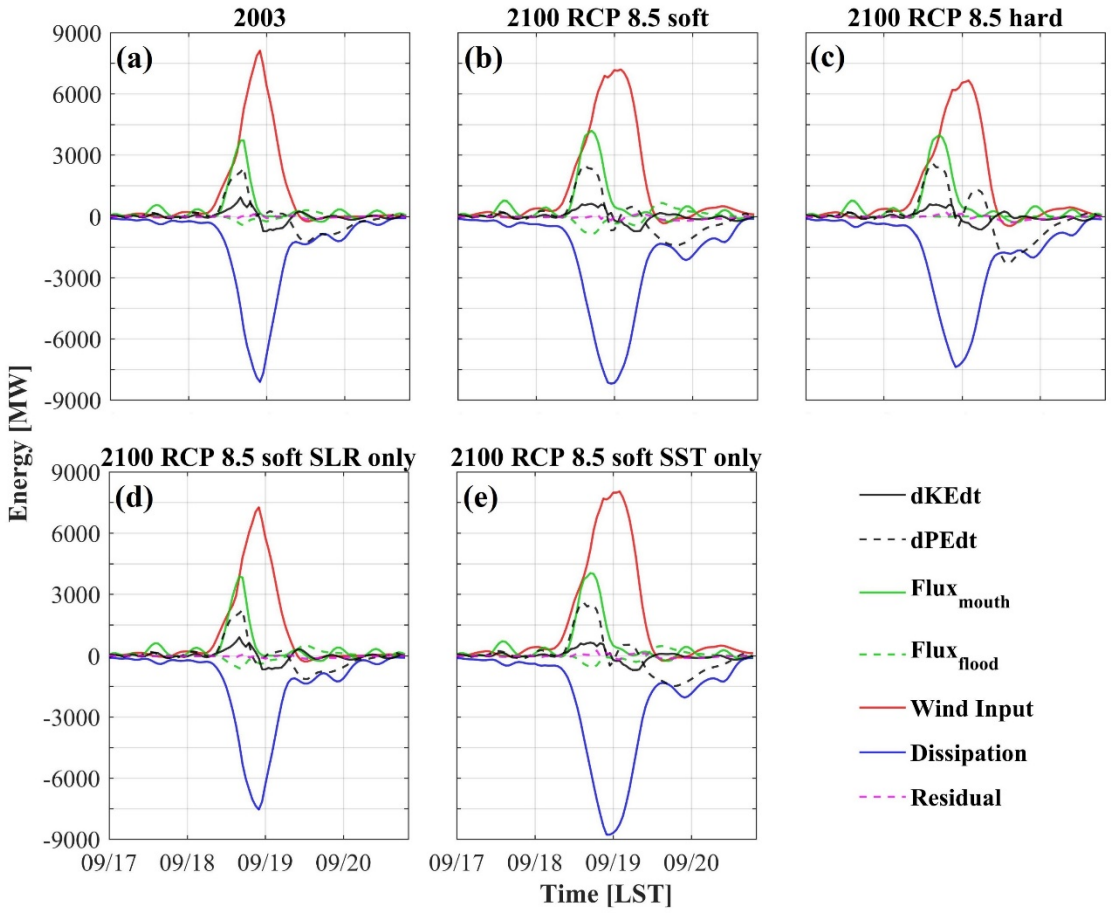

Figure 4.8 Volume-integrated energetics within present shoreline (i.e. control volume; see text for details) for different scenarios in Figure 4.7. 1 MW=10^6 W.

First, we use Figure 4.8a (hindcast) to elucidate the relationship between energetics and surge dynamics. *Flux*$_{mouth}$ (solid green line) is mostly attributed to incoming surges generated outside the bay mouth. The peak of *Flux*$_{mouth}$ coincided with the peak surge at CBBT, suggesting the surge in the lower bay was mainly driven by incoming energy flux. Once Isabel passed bay mouth and moved farther north, *Flux*$_{mouth}$ started to decline given reduced surge on the shelf under shore-parallel winds. However, *Flux*$_{mouth}$ stayed above zero, indicating the incoming energy propagated inside the bay instead of returning to the shelf. In the meanwhile, northward winds over the bay surface also input energy to the surge. The peak in *Wind Input* (solid red line) coincided with maximum kinetic energy (or

zero *dKEdt*; solid black line) given its linear relationship with surface current velocity ($\overrightarrow{\tau_s} \cdot \overrightarrow{u_s}$). After that, the fading winds and reduced surface current velocity resulted in a rapid decline of *Wind Input*, and *Wind Input* became zero around 0800 LST 19 September. Concurrently, potential energy began to decrease (*dPEdt*<0; dashed black line), corresponding to the falling surge at Baltimore (Figure 4.5). Eventually, both $Flux_{mouth}$ and *Wind Input* were dissipated within the bay, while the dissipation lagged behind energy input as indicated by the tail (solid blue line) after 0800 LST 19 September. $Flux_{flood}$ (dashed green line) was relatively small compared to other terms during Isabel in 2003.

To investigate the impact of warmer SST on storm surge, we compare Figures 4.8a and 4.8e. With stronger storm in 2100 RCP 8.5, $Flux_{mouth}$ in Figure 4.8e is 300 MW larger due to higher offshore surge. The peak values of *Wind Input* in Figures 4.8a and 4.8e are comparable, given the future Isabel has slightly higher intensity after landfall but more westward track. However, due to slower storm translation speed in the future (Figure A3), the peak of *Wind Input* in Figure 4.8e is wider, resulting in more wind energy input. With the same rationale, the peak of $Flux_{mouth}$ in Figure 4.8e is wider as well, leading to larger total incoming energy flux. The increased energy input through bay mouth and bay surface in Figure 4.8e lead to ~30 TJ higher potential energy in the bay (c.f. Figures 4.9a and 4.9e). This substantial increase in potential energy explains the higher surge with warmer SST, given potential energy is proportional to squared surge height.

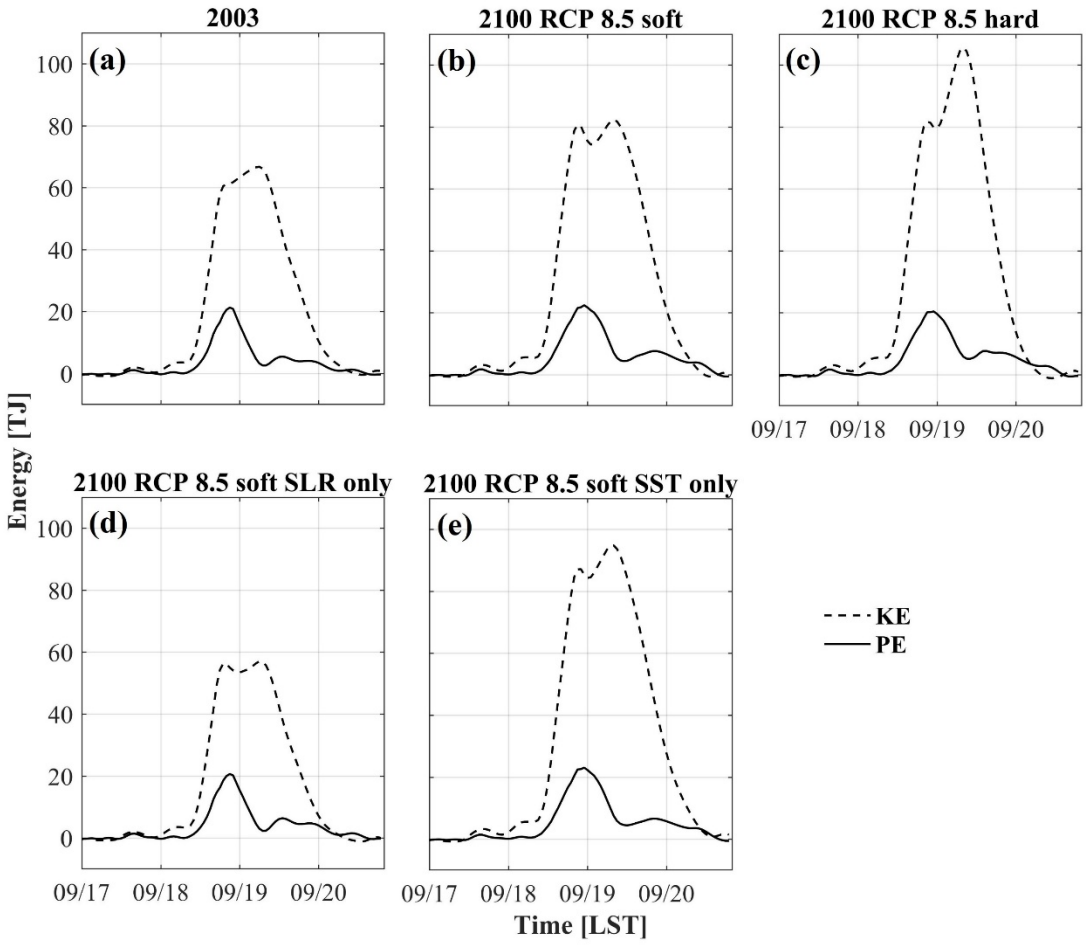

Figure 4.9 Volume-integrated kinetic energy and potential energy within present shoreline. 1 TJ=10^{12} J.

Next, we investigate how sea level rise affects storm surge in Chesapeake Bay. In the momentum equation, velocity follows $\frac{d\vec{u}}{dt} \propto \frac{\overrightarrow{\tau_s}-\overrightarrow{\tau_b}}{\rho H}$. Since bottom stress $\overrightarrow{\tau_b}$ is a function of velocity, the relationship between $\frac{d\vec{u}}{dt}$ and 1/*H* is non-linear. Numerical model results show that surface velocities are ~0.1 m s^{-1} smaller in the lower bay, east side of middle bay, and upper bay with increased *H* (Figure A4). Consequently, the peak of *Wind Input* ($\overrightarrow{\tau_s} \cdot \overrightarrow{u_s}$) in Figure 4.8d is 850 MW lower than that in Figure 4.8a. On the other hand, bottom friction and vertical shear are altered as well given changes in velocity with sea level rise,

and the peak value of *Dissipation* reduces by 550 MW in 2100 RCP 8.5 soft SLR only compared with hindcast. Moreover, the peaks of incoming energy $Flux_{mouth}$ and outgoing energy $Flux_{flood}$ increase by 150 and 200 MW, respectively, given larger lateral areas with increased *H*. In summary, the decrease in energy source exceeds the decrease in energy sink with sea level rise. As a result, potential energy is ~10 TJ lower in Figure 4.9d than in Figure 4.9a, and the surge height decreases with sea level rise.

Finally, we investigate how hard shoreline affects storm surge. Given the fundamental difference between soft and hard shoreline is whether landward energy flux ($Flux_{flood}$) is allowed, a zoomed-in view of Figures 4.8b and 4.8c for *dKEdt*, *dPEdt*, and $Flux_{flood}$ are presented in Figure 4.10 to provide clearer visual inspection. The stronger storm and higher mean sea level lead to significantly larger $Flux_{flood}$ in 2100 RCP 8.5 soft compared to that in hindcast (c.f. Figures 4.8a and 4.10a). In Figure 4.10a, a peak of 800 MW in $Flux_{flood}$ occurs around 1600 LST 18 September, which is corresponding to the flooding around lower bay tributaries; a second peak of 400 MW in $Flux_{flood}$ occurs around 0500 LST 19 September, which is corresponding to the flooding in middle-bay wetlands. The positive value of $Flux_{flood}$ during late 19 September represents returning energy from wetland to the control volume. Overall, energy flux towards wetland during flood stage is substantial in soft shoreline scenario: the wetlands receives up to 35 TJ energy, while potential energy integrated over the entire control volume is ~80 TJ (Figure 4.10c). Moreover, while 25 TJ energy returns to the control volume during ebb stage, 10 TJ energy is dissipated in the wetlands. On the other hand, the implementation of hard shoreline prohibits energy flux towards wetland (Figure 4.10b), leading to higher energy within the

present shoreline. Comparison between Figures 4.10c and 4.10d shows that although kinetic energy is almost the same, peak potential energy is ~30 TJ higher with hard shoreline than with soft shoreline, which matches the energy transferred to the wetlands in soft shoreline scenario. Therefore, higher surge with hard shoreline is mainly due to zero $Flux_{flood}$.

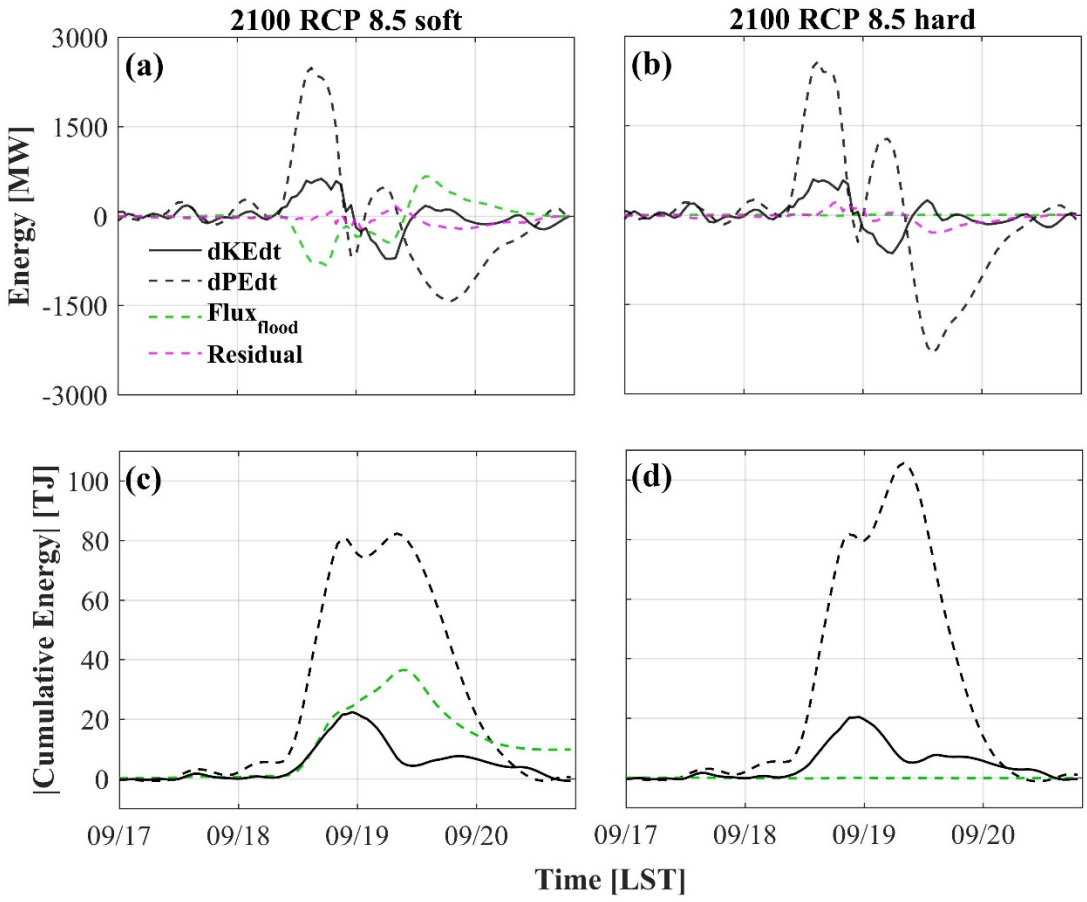

Figure 4.10 (a)-(b) Zoomed-in view of Figures 4.8b and 4.8c for selected energetics. (c)-(d) Time-integrated energetics (absolute value).

4.5 Conclusion and discussion

This study has investigated storm surges in Chesapeake Bay induced by Isabel-like tropical cyclones under future climate projections with an atmosphere-ocean model. In the

atmosphere, the projected warmer SST leads to stronger tropical cyclones. In the estuary, without shoreline protection, the increased surface momentum flux and sea level rise result in increased surge height in the lower and upper bay, but same or decreased surge height in the middle bay. Furthermore, with the addition of hard shoreline, future storm surge height increases substantially throughout the entire bay, especially in the upper portion.

Previous studies have shown that storm intensification can increase surge heights (Lowe et al. 2001; Mousavi et al. 2011; Lin et al. 2012), however, diverse responses of surge heights to sea level rise have been reported (Lowe et al. 2001; Smith et al. 2010; Mousavi et al. 2011; Lin et al. 2012). With two idealized runs: one with warmer SST only and the other with sea level rise only, we have identified that while storm intensification increases storm surge height significantly in the lower and upper bay, sea level rise reduces storm surge height slightly throughout the entire bay. The reduction of surge height due to sea level rise is consistent with Mousavi et al. (2011) who found ~10% decrease in surge height within Corpus Christi Bay given 0.75 m relative sea level rise, but in contrast to Smith et al. (2010) who identified substantial increase (up to 5 m) in surge height in southeast Louisiana due to 1 m sea level rise. On the other hand, both Mousavi et al. (2011) and Smith et al. (2010) found that the impact of sea level rise to storm surge is most significant in shallow areas where the sea level rise is a significant portion of bathymetry. Given the bathymetry of Chesapeake Bay (mean depth ~8 m) is generally deeper than both Corpus Christi Bay (~3.5 m) and southeast Louisiana wetlands (less than 5 m), the response of storm surge to sea level rise in Chesapeake Bay is less significant (~7% reduction).

Moreover, the comparison between soft and hard shoreline scenarios has shown that hard shoreline increases storm surge slightly in the lower bay, but significantly in the middle and upper bay. A similar spatial pattern was observed by Lee et al. (2017) in Chesapeake Bay tides. They found the tidal ranges with hard shoreline are 2% smaller in the lower bay, but 20% larger in the middle and upper bay compared to those with soft shoreline. This implies hard shoreline increases storm surge height and tidal amplitude through similar physics processes.

Limited discussion of the underlying physics for the impact of climate change on storm surge was provided in preceding literature. In this study, we have applied energy budget equation to help identify how each climate factor affect storm surge in Chesapeake Bay. With warmer SST, both wind energy input over bay surface and incoming energy flux through bay mouth are larger compared to hindcast, leading to higher potential energy and higher storm surge. Sea level rise reduces current velocity in most part of the bay and results in smaller wind energy input and smaller dissipation. However, the decrease in dissipation is smaller than decrease in wind energy input. Consequently, the potential energy is lower compared to hindcast, leading to reduced storm surge. Moreover, the impact of hard shoreline on storm surge has also been investigated with the same equation: with zero landward energy flux, the potential energy within the main stem of the bay increases by over 40%, leading to substantial increase in surge height. In a future study, it would be worthwhile to investigate how other shoreline management plans affect storm surge in Chesapeake Bay in addition to the two extreme cases discussed here.

4.6 Acknowledgements

Funding support was provided by Maryland Sea Grant (NA14OAR4170090, SA75281450-H) and the NOAA Cooperative Institute for the North Atlantic Region (CINAR, NA13OAR4830233), Disaster Recovery Act. Fan Zhang is supported by Maryland Sea Grant Fellowship. Model output is available upon request. This is UMCES contribution number xxxx.

CHAPTER 5

CONCLUSIONS

In this dissertation, a high-resolution atmosphere-ocean model is used to investigate the response of the coastal ocean and estuaries to tropical cyclones, with support of observational data. While we focus on MAB and Chesapeake Bay, the findings of this study are applicable to many other coastal oceans where the water column is dominated by two-layer stratification during hurricane season and semi-enclosed bays which are surrounded by low-lying lands. A summary of major findings is provided in this section.

During Hurricane Arthur (2014), HF-radar observed ~ 0.4 m s^{-1} surface NICs on the MAB shelf, and glider ADCP observed mode-1 NICs around 30-m isobath off the New Jersey coast. The atmosphere-ocean model results compare favorably with these observations and enables the investigation of spatial variabilities of coastal NICs. In the cross-shore direction, the NICs were stronger offshore and weaker inshore; in the alongshore direction, NICs were strongest near Hudson Shelf Valley. With energy budget analysis, we find this horizontal spatial variability is mostly controlled by wind energy input. Moreover, these shelf NICs were dominated by mode-1 vertical structure, with comparable velocity magnitudes but opposite velocity directions between surface and bottom water column. As such, NICs accounted for 60-80% of the shear on the New England shelf and 30-50% farther south on the MAB.

Several tidal gauge stations along the MAB coast and in Chesapeake Bay also observed significant storm surge during Hurricane Arthur. Therefore, Arthur is used as a case study to investigate the impact of WRF physics parameterization schemes and model configurations on storm surge prediction. The turbulence closure scheme in the planetary

boundary layer affects the prediction of the storm intensity: the local closure scheme produces lower equivalent potential temperature than the non-local closure schemes, leading to significant reductions in the maximum surface wind speed and surge heights. On the other hand, higher-class cloud microphysics schemes over-predict the wind speed, resulting in large over-prediction of storm surge at some coastal locations. Without cumulus parameterization in the outermost domain, both the wind speed and storm surge are grossly under-predicted due to large precipitation decreases in the storm center. None of the choices for the WRF physics parameterization schemes significantly affect the prediction of Arthur's track. Sea surface temperature affects the latent heat release from the ocean surface and thus storm intensity and storm surge predictions. The large-scale atmospheric circulation models provide the initial and boundary conditions for WRF, and influence both the track and intensity predictions, thereby changing the spatial distribution of storm surge along the coastline. Despite significant divergence in these storm surge predictions, their ensemble mean provides the best surge forecast.

In the future, warmer ocean and storm intensification, relative sea level rise, and implementation of hard shoreline can affect storm surge. By downscaling future climate to the regional atmosphere-ocean model, we find the revisits of Hurricane Isabel to Chesapeake Bay in 2050 and 2100 can induce increased storm surge in the lower and upper bay, but same or decreased storm surge in the middle bay compared to the hindcast. With the addition of hard shoreline, future storm surge height increases substantially throughout the entire bay, especially in the upper portion. To understand how each factor affects storm surge, energy budget equation is used. We find with warmer SST, both wind energy input

over bay surface and incoming energy flux through bay mouth are increased compared to hindcast, leading to higher storm surge. On the other hand, sea level rise reduces both wind energy input and dissipation. Nevertheless, the decrease in dissipation is less than decrease in wind energy input. As such, storm surge is lower with sea level rise. Moreover, with hard shoreline implemented, landward energy flux is prohibited, and potential energy within the main stem of the bay increases by over 40%, leading to substantial higher storm surge.

For future studies, as a step towards improving storm intensity prediction, it would be worthwhile to quantify how much surface cooling in the coastal ocean during tropical cyclones is caused by NICs-induced mixing. Meanwhile, a more sophisticated selection of ensemble members is needed for better storm surge prediction, which may require more sensitivity analysis. Furthermore, given the dilemma between the demand of protecting low-lying areas under sea level rise and the risk of increasing storm surge with hard shoreline, it would be beneficial to future shoreline management by examining storm surge under more hybrid shoreline scenarios (e.g., hard shoreline for metropolitan areas and soft shoreline for rural areas).

APPENDIX A

VALIDATION OF STORM SURGE SIMULATION AND OTHER DIAGNOSTIC FIGURES

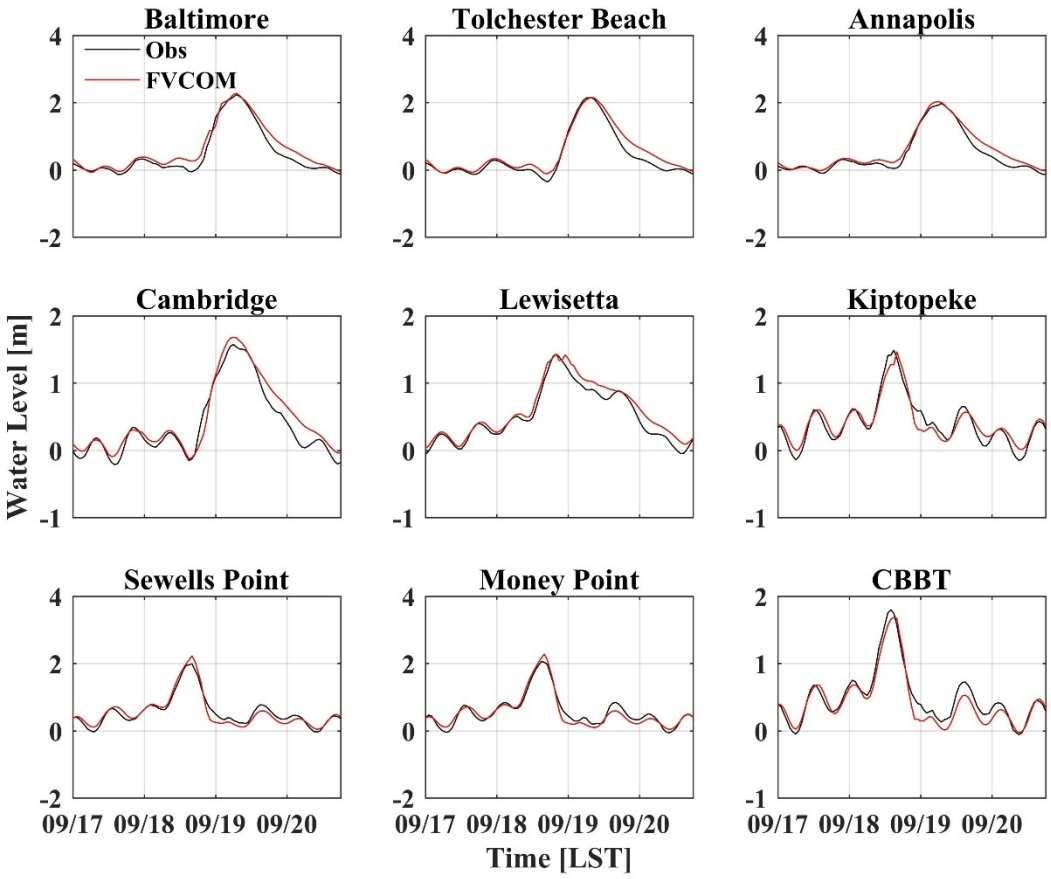

Figure A1 Storm tide at nine tidal gauge stations in Chesapeake Bay during Hurricane Isabel (2003). The black lines represent observational data and the red lines are results from FVCOM.

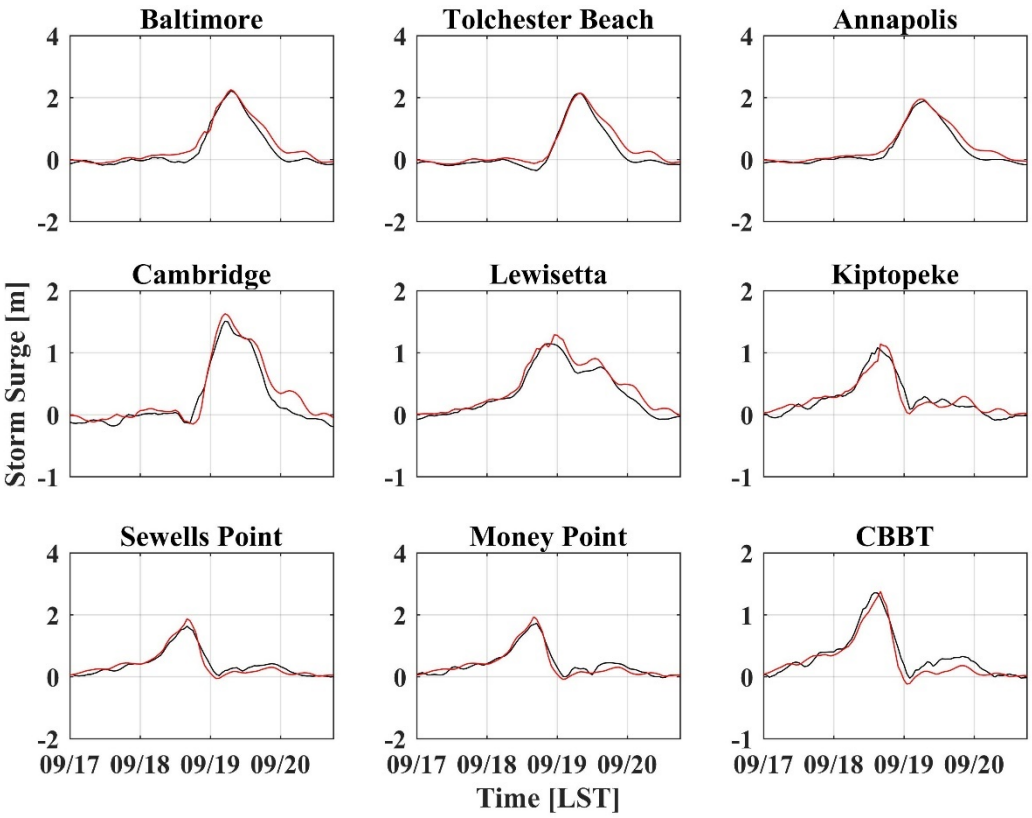

Figure A2 Same as Figure A1, but for storm surge.

Table A1 Statistical analyses of storm tide and storm surge from hindcast.

		Baltimore	Tolchester Beach	Annapolis	Cambridge	Lewisetta	Kiptopeke	Sewells Point	Money Point	CBBT
Storm Tide	Root-mean-square error [m]	0.18	0.18	0.15	0.15	0.10	0.10	0.12	0.12	0.11
	Relative average error	0.03	0.03	0.03	0.04	0.03	0.05	0.03	0.03	0.04
	Correlation coefficient	0.98	0.98	0.99	0.97	0.99	0.96	0.97	0.97	0.97
	Skill	0.98	0.98	0.98	0.97	0.98	0.96	0.98	0.98	0.97
Storm Surge	Root-mean-square error [m]	0.18	0.18	0.15	0.15	0.10	0.10	0.12	0.12	0.11
	Relative average error	0.04	0.03	0.03	0.04	0.04	0.07	0.04	0.04	0.05
	Correlation coefficient	0.98	0.98	0.99	0.97	0.99	0.94	0.97	0.97	0.96
	Skill	0.98	0.98	0.98	0.97	0.97	0.96	0.97	0.98	0.96

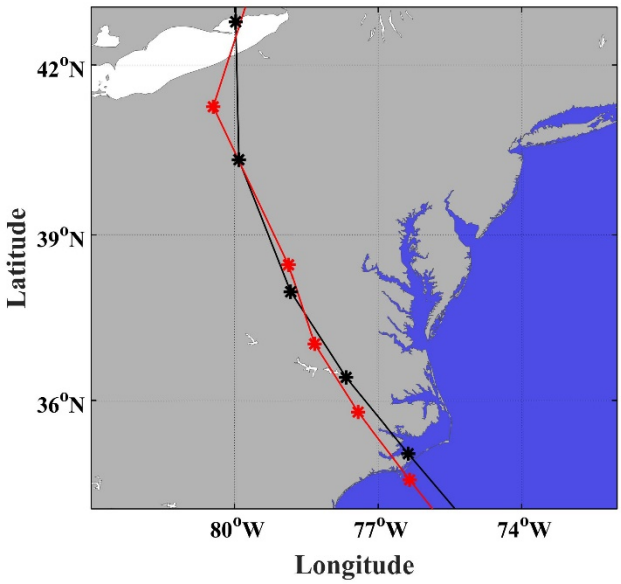

Figure A3 Strom tracks of Isabel in hindcast (black) and 2100 RCP 8.5 (red). The star signs are plotted every six hours. The landfalling time for both scenarios are around 1200 LST 18 September.

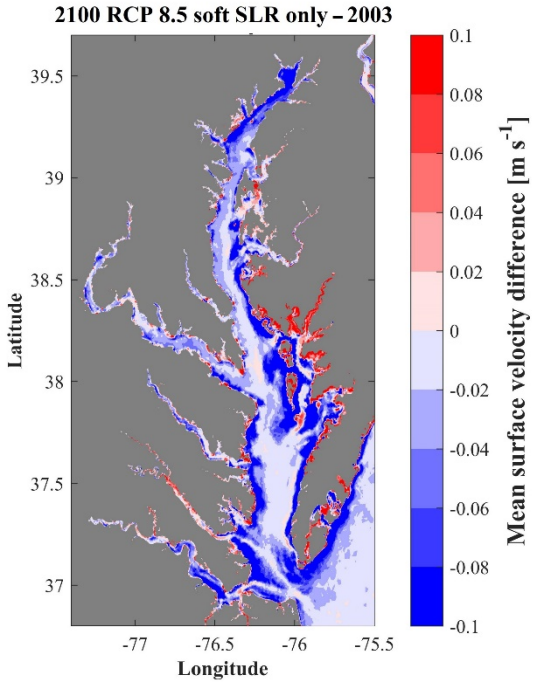

Figure A4 Differences of time-averaged surface velocity between 2100 RCP 8.5 soft SLR only and hindcast. The velocities are averaged over the flood stage of the storm surge.

BIBLIOGRAPHY

Alford, M. H., MacKinnon, J. A., Simmons, H. L., & Nash, J. D. (2016). Near-inertial internal gravity waves in the ocean. *Annual Review of Marine Science, 8*, 95-123.

Alford, M. H., & Zhao, Z. (2007). Global patterns of low-mode internal-wave propagation. Part I: Energy and energy flux. *Journal of Physical Oceanography, 37*(7), 1829-1848.

Amante, C., & Eakins, B. W. (2009). ETOPO1 Global Relief Model converted to PanMap layer format, NOAA-National Geophysical Data Center, Boulder, Colorado.

Arcement, G. J. Jr., and V. R. Schneider, 1989: Guide for selecting Manning's roughness coefficients for natural channels and flood plains, U.S. Geological Survey Water Supply Papers, 2339.

Barrick, D. E. (1971a). Theory of HF and VHF Propagation Across the Rough Sea, 1, The Effective Surface Impedance for a Slightly Rough Highly Conducting Medium at Grazing Incidence, *Radio Science*, *6*(5), 517–526.

Barrick, D. E. (1971b). Theory of HF and VHF Propagation Across the Rough Sea, 2, Application to HF and VHF Propagation Above the Sea, *Radio Science*, *6*(5), 527–533.

Beardsley, R. C., Chen, C., & Xu, Q. (2013). Coastal flooding in Scituate (MA): A FVCOM study of the 27 December 2010 nor'easter. *Journal of Geophysical Research: Oceans*, *118*(11), 6030-6045.

Belcher, S. E., Grant, A. L., Hanley, K. E., Fox-Kemper, B., Van Roekel, L., Sullivan, P. P., ... & Rutgersson, A. (2012). A global perspective on Langmuir turbulence in the ocean surface boundary layer. *Geophysical Research Letters*, *39*(18).

Bender, M. A., Knutson, T. R., Tuleya, R. E., Sirutis, J. J., Vecchi, G. A., Garner, S. T., & Held, I. M. (2010). Modeled impact of anthropogenic warming on the frequency of intense Atlantic hurricanes. *Science*, *327*(5964), 454-458.

Berg, R., 2015: Tropical Cyclone Report: Hurricane Arthur (AL012014). National Hurricane Center Tropical Cyclone Report, 43 pp.

Beven, J., & Cobb, H. (2004). Tropical Cyclone Report Hurricane Isabel. National Hurricane Center. National Weather Service.

Boesch, D. F., Atkinson, L. P., Boicourt, W. C., Boon, J. D., Cahoon, D. R., Dalrymple, R. A., ... & Li, M. (2013). Updating Maryland's sea-level rise projections: Special report of the scientific and technical working group to the Maryland Climate Change Commission. University of Maryland Center for Environmental Science: Cambridge, MD, USA.

Braun, S. A., & Tao, W. K. (2000). Sensitivity of high-resolution simulations of Hurricane Bob (1991) to planetary boundary layer parameterizations. *Monthly Weather Review*, *128*(12), 3941-3961.

Brooks, D. A. (1983). The wake of Hurricane Allen in the western Gulf of Mexico. *Journal of Physical Oceanography*, *13*(1), 117-129.

Bunya, S., Dietrich, J. C., Westerink, J. J., Ebersole, B. A., Smith, J. M., Atkinson, J. H., ... & Cardone, V. J. (2010). A high-resolution coupled riverine flow, tide, wind, wind wave, and storm surge model for southern Louisiana and Mississippi. Part I: Model development and validation. *Monthly Weather Review*, *138*(2), 345-377.

Burchard, H. (2002). Applied Turbulence Modelling in Marine Waters. Berlin, Germany: Springer.

Burchard, H., & Bolding, K. (2001). Comparative analysis of four second-moment turbulence closure models for the oceanic mixed layer. *Journal of Physical Oceanography*, *31*(8), 1943-1968.

Castelao, R., Glenn, S., & Schofield, O. (2010). Temperature, salinity, and density variability in the central Middle Atlantic Bight. *Journal of Geophysical Research: Oceans*, *115*(C10).

Chant, R. J. (2001). Evolution of near-inertial waves during an upwelling event on the New Jersey inner shelf. *Journal of Physical Oceanography*, *31*(3), 746-764.

Chen, C., Liu, H., & Beardsley, R. C. (2003). An unstructured grid, finite-volume, three-dimensional, primitive equations ocean model: application to coastal ocean and estuaries. *Journal of Atmospheric and Oceanic Technology*, *20*, 159-186.

Chen, C., Beardsley, R. C., Luettich, R. A., Westerink, J. J., Wang, H., Perrie, W., ... & Zhao, L. (2013). Extratropical storm inundation testbed: Intermodel comparisons in Scituate, Massachusetts. *Journal of Geophysical Research: Oceans*, *118*(10), 5054-5073.

Chen, C., Reid, R. O., & Nowlin, W. D. (1996). Near-inertial oscillations over the Texas-Louisiana shelf. *Journal of Geophysical Research: Oceans*, *101*(C2), 3509-3524.

Chen, S. S., Price, J. F., Zhao, W., Donelan, M. A., & Walsh, E. J. (2007). The CBLAST-Hurricane program and the next-generation fully coupled atmosphere–wave–ocean models for hurricane research and prediction. *Bulletin of the American Meteorological Society*, *88*(3), 311-318.

Church, J. A., Clark, P. U., Cazenave, A., Gregory, J. M., Jevrejeva, S., Levermann, A., ... & Payne, A. J. (2013). Sea level change, in *Climate Change 2013: The Physical*

Science Basis Contribution of Working Group I to the Fifth Assessment Report of the Intergovernmental Panel on Climate Change, edited by T. F. Stocker, D. Qin, G.-K. Plattner, M. Tignor, S. K. Allen, J. Boschung, A. Nauels, Y. Xia, V. Bex, and P. M. Midgley, pp. 1137–1216, Cambridge University Press, U. K.

Churchill, J. H., Wirick, C. D., Flagg, C. N., & Pietrafesa, L. J. (1994). Sediment resuspension over the continental shelf east of the Delmarva Peninsula. *Deep Sea Research Part II: Topical Studies in Oceanography*, *41*(2-3), 341-363.

Colle, B. A., Bowman, M. J., Roberts, K. J., Bowman, M. H., Flagg, C. N., Kuang, J., ... & Zhang, F. (2015). Exploring water level sensitivity for metropolitan New York during Sandy (2012) using ensemble storm surge simulations. *Journal of Marine Science and Engineering*, *3*(2), 428-443.

Collins, M., and R. Knutti (2013), Chapter 12: Long-term climate change: Projections, commitments and irreversibility, in *Climate Change 2013. Contribution of Working Group 1 to the Fifth Assessment Report of the Intergovernmental Panel on Climate Change*, pp. 1029–1136, Cambridge University Press, U. K., and New York.

Cummins, P. F., & Oey, L. Y. (1997). Simulation of barotropic and baroclinic tides off northern British Columbia. *Journal of Physical Oceanography*, *27*(5), 762-781.

Cuypers, Y., Le Vaillant, X., Bouruet-Aubertot, P., Vialard, J., & Mcphaden, M. J. (2013). Tropical storm-induced near-inertial internal waves during the Cirene experiment: Energy fluxes and impact on vertical mixing. *Journal of Geophysical Research: Oceans*, *118*(1), 358-380.

D'Asaro, E. A. (1985). The energy flux from the wind to near-inertial motions in the surface mixed layer. *Journal of Physical Oceanography*, *15*(8), 1043-1059.

D'Asaro, E. A. (1995a). Upper-ocean inertial currents forced by a strong storm. Part II: Modeling. *Journal of Physical Oceanography*, *25*(11), 2937-2952.

D'Asaro, E. A. (1995b). Upper-ocean inertial currents forced by a strong storm. Part III: Interaction of inertial currents and mesoscale eddies. *Journal of Physical Oceanography*, *25*(11), 2953-2958.

D'Asaro, E. A., Eriksen, C. C., Levine, M. D., Paulson, C. A., Niiler, P., & Van Meurs, P. (1995). Upper-ocean inertial currents forced by a strong storm. Part I: Data and comparisons with linear theory. *Journal of Physical Oceanography*, *25*(11), 2909-2936.

D'Asaro, E. A., Sanford, T. B., Niiler, P. P., & Terrill, E. J. (2007). Cold wake of hurricane Frances. Geophysical Research Letters, *34*(15).

Davis, C., Wang, W., Chen, S. S., Chen, Y., Corbosiero, K., DeMaria, M., ... & Reeves, H. (2008). Prediction of landfalling hurricanes with the advanced hurricane WRF model. *Monthly Weather Review*, *136*(6), 1990-2005.

Dietrich, J. C., Bunya, S., Westerink, J. J., Ebersole, B. A., Smith, J. M., Atkinson, J. H., ... & Cardone, V. J. (2010). A high-resolution coupled riverine flow, tide, wind, wind wave, and storm surge model for southern Louisiana and Mississippi. Part II: Synoptic description and analysis of Hurricanes Katrina and Rita. *Monthly Weather Review*, *138*(2), 378-404.

Di Liberto, T., Colle, B. A., Georgas, N., Blumberg, A. F., & Taylor, A. A. (2011). Verification of a multimodel storm surge ensemble around New York City and Long Island for the cool season. *Weather and Forecasting*, *26*(6), 922-939.

Egbert, G. D., & Erofeeva, S. Y. (2002). Efficient inverse modeling of barotropic ocean tides. *Journal of Atmospheric and Oceanic Technology, 19*(2), 183-204.

Elsner, J. B., Kossin, J. P., & Jagger, T. H. (2008). The increasing intensity of the strongest tropical cyclones. *Nature, 455*(7209), 92-95.

Emanuel, K. A. (1987). The dependence of hurricane intensity on climate. *Nature, 326*(6112), 483-485.

Emanuel, K. A. (1999). Thermodynamic control of hurricane intensity. *Nature, 401*(6754), 665-669.

Emanuel, K., Ravela, S., Vivant, E., & Risi, C. (2006). A statistical deterministic approach to hurricane risk assessment. *Bulletin of the American Meteorological Society, 87*(3), 299-314.

Emanuel, K. A., Sundararajan, R., & Williams, J. (2008). Hurricanes and global warming: Results from downscaling IPCC AR4 simulations. *Bulletin of the American Meteorological Society, 89*(3), 347-367.

Engelhart, S. E., Horton, B. P., & Kemp, A. C. (2011). Holocene sea level changes along the United States' Atlantic Coast. *Oceanography, 24*(2), 70-79.

Ezer, T., L. P. Atkinson, W. B. Corlett, & J. L. Blanco (2013), Gulf Stream's induced sea level rise and variability along the U.S. mid-Atlantic coast, *Journal of Geophysical Research: Oceans*, *118*, 685–697.

Fairall, C. W., Bradley, E. F., Hare, J. E., Grachev, A. A., & Edson, J. B. (2003). Bulk parameterization of air–sea fluxes: Updates and verification for the COARE algorithm. *Journal of Climate, 16*(4), 571-591.

Fleming, N. E. (2016). Seasonal and spatial variability in temperature, salinity and

circulation of the Middle Atlantic Bight, (Ph.D. thesis). Rutgers The State University of New Jersey-New Brunswick.

Georgas, N., Orton, P., Blumberg, A., Cohen, L., Zarrilli, D., & Yin, L. (2014). The impact of tidal phase on Hurricane Sandy's flooding around New York City and Long Island Sound. *Journal of Extreme Events*, *1*(01), 1450006.

Gill, A. E., 1982: *Atmosphere–Ocean Dynamics*. Academic Press, 662 pp.

Gill, A. E. (1984). On the behavior of internal waves in the wakes of storms. *Journal of Physical Oceanography*, *14*(7), 1129-1151.

Glenn, S. M., Miles, T. N., Seroka, G. N., Xu, Y., Forney, R. K., Yu, F., ... Kohut, J. (2016). Stratified coastal ocean interactions with tropical cyclones. *Nature Communications*, *7*, 10887.

Grell, G. A., J. Dudhia, and D. Stauffer, 1994: A description of the fifth-generation PENN State/NCAR Mesoscale Model (MM5). NCAR Tech. Note NCAR/TN-398STR, 138 pp.

Holland, G. J. (1980). An analytic model of the wind and pressure profiles in hurricanes. *Monthly weather review*, *108*(8), 1212-1218.

Holland, G. J. (1997). The maximum potential intensity of tropical cyclones. *Journal of the atmospheric sciences*, *54*(21), 2519-2541.

Hong, S. Y., Dudhia, J., & Chen, S. H. (2004). A revised approach to ice microphysical processes for the bulk parameterization of clouds and precipitation. *Monthly Weather Review*, *132*(1), 103-120.

Hong, S. Y., and S. W. Kim, 2008: Stable boundary layer mixing in a vertical diffusion scheme. In *18th Symposium on Boundary Layers and Turbulence B* (Vol. 16).

Hong, S. Y., & Lim, J. O. J. (2006). The WRF single-moment 6-class microphysics scheme (WSM6). *Journal of Korean Meteorology Society*, *42*(2), 129-151.

Hong, S. Y., Noh, Y., & Dudhia, J. (2006). A new vertical diffusion package with an explicit treatment of entrainment processes. *Monthly Weather Review*, *134*(9), 2318-2341.

Hong, S. Y., & Pan, H. L. (1996). Nonlocal boundary layer vertical diffusion in a medium-range forecast model. *Monthly Weather Review*, *124*(10), 2322-2339.

Houghton, R. W., Schlitz, R., Beardsley, R. C., Butman, B., & Chamberlin, J. L. (1982). The Middle Atlantic Bight cold pool: Evolution of the temperature structure during summer 1979. *Journal of Physical Oceanography*, *12*(10), 1019-1029.

Iacono, M. J., Delamere, J. S., Mlawer, E. J., Shephard, M. W., Clough, S. A., & Collins, W. D. (2008). Radiative forcing by long-lived greenhouse gases: Calculations with the AER radiative transfer models. *Journal of Geophysical Research: Atmospheres*, *113*(D13).

Irish, J. L., Resio, D. T., & Ratcliff, J. J. (2008). The influence of storm size on hurricane surge. *Journal of Physical Oceanography*, *38*(9), 2003-2013.

Jaimes, B., & Shay, L. K. (2010). Near-inertial wave wake of Hurricanes Katrina and Rita over mesoscale oceanic eddies. *Journal of Physical Oceanography*, *40*(6), 1320-1337

Janjic, Z. I. (1994). The step-mountain eta coordinate model: Further developments of the convection, viscous sublayer, and turbulence closure schemes. *Monthly Weather Review*, *122*(5), 927-945.

Janjic, Z. I., 1996: The surface layer in the NCEP Eta model. Preprints, 11th Conf. on Numerical Weather Prediction, Norfolk, VA, *American Meteorology Society*, 354–

355.

Jevrejeva, S., Jackson, L. P., Riva, R. E., Grinsted, A., & Moore, J. C. (2016). Coastal sea level rise with warming above 2 C. *Proceedings of the National Academy of Sciences*, *113*(47), 13342-13347.

Jimenez, P. A., Dudhia, J., González-Rouco, J. F., Navarro, J., Montávez, J. P., & García-Bustamante, E. (2012). A revised scheme for the WRF surface layer formulation. *Monthly Weather Review*, *140*(3), 898-918.

Jolliff, J. K., Kindle, J. C., Shulman, I., Penta, B., Friedrichs, M. A., Helber, R., & Arnone, R. A. (2009). Summary diagrams for coupled hydrodynamic-ecosystem model skill assessment. *Journal of Marine Systems*, *76*(1-2), 64-82.

Kain, J. S. (2004). The Kain–Fritsch convective parameterization: an update. *Journal of Applied Meteorology*, *43*(1), 170-181.

Kepert, J. D. (2012). Choosing a boundary layer parameterization for tropical cyclone modeling. *Monthly Weather Review*, *140*(5), 1427-1445.

Kerr, P. C., Donahue, A. S., Westerink, J. J., Luettich, R. A., Zheng, L. Y., Weisberg, R. H., ... & Roland, A. (2013a). US IOOS coastal and ocean modeling testbed: Inter-model evaluation of tides, waves, and hurricane surge in the Gulf of Mexico. *Journal of Geophysical Research: Oceans*, *118*(10), 5129-5172.

Kerr, P. C., Martyr, R. C., Donahue, A. S., Hope, M. E., Westerink, J. J., Luettich, R. A., ... & Westerink, H. J. (2013b). US IOOS coastal and ocean modeling testbed: Evaluation of tide, wave, and hurricane surge response sensitivities to mesh resolution and friction in the Gulf of Mexico. *Journal of Geophysical Research: Oceans*, *118*(9), 4633-4661.

Kilic, C., & Raible, C. C. (2013). Investigating the sensitivity of hurricane intensity and trajectory to sea surface temperatures using the regional model WRF. *Meteorologische Zeitschrift*, *22*(6), 685-698.

Kohut, J., Roarty, H., Randall-Goodwin, E., Glenn, S., & Lichtenwalner, C. S. (2012). Evaluation of two algorithms for a network of coastal HF radars in the Mid-Atlantic Bight. *Ocean Dynamics*, *62*(6), 953-968.

Kopp, R. E. (2013). Does the mid-Atlantic United States sea level acceleration hot spot reflect ocean dynamic variability? *Geophysical Research Letters*, *40*(15), 3981-3985.

Knutson, T. R., McBride, J. L., Chan, J., Emanuel, K., Holland, G., Landsea, C., ... & Sugi, M. (2010). Tropical cyclones and climate change. *Nature Geoscience*, *3*(3), 157-163.

Kundu, P. K., Chao, S. Y., & McCreary, J. P. (1983). Transient coastal currents and inertio-gravity waves. *Deep Sea Research Part A. Oceanographic Research Papers*, *30*(10), 1059-1082.

Kunze, E. (1985). Near-inertial wave propagation in geostrophic shear. *Journal of Physical Oceanography*, *15*(5), 544-565.

Lee, S. B., Li, M., & Zhang, F. (2017). Impact of sea level rise on tidal range in Chesapeake and Delaware Bays. *Journal of Geophysical Research: Oceans*, *122*(5), 3917-3938.

Lentz, S. J. (2017). Seasonal warming of the Middle Atlantic Bight Cold Pool. *Journal of Geophysical Research: Oceans*, *122*(2), 941-954.

Lentz, S., Carr, M., & Herbers, T. H. C. (2001). Barotropic tides on the North Carolina shelf. *Journal of Physical Oceanography*, *31*(7), 1843-1859.

Li, X., & Pu, Z. (2008). Sensitivity of numerical simulation of early rapid intensification of Hurricane Emily (2005) to cloud microphysical and planetary boundary layer

parameterizations. *Monthly Weather Review*, *136*(12), 4819-4838.

Li, M., Zhong, L., Boicourt, W. C., Zhang, S., & Zhang, D. L. (2006). Hurricane-induced storm surges, currents and destratification in a semi-enclosed bay. *Geophysical Research Letters*, *33*(2).

Lim, K. S. S., & Hong, S. Y. (2010). Development of an effective double-moment cloud microphysics scheme with prognostic cloud condensation nuclei (CCN) for weather and climate models. *Monthly Weather Review*, *138*(5), 1587-1612.

Lin, N., Emanuel, K., Oppenheimer, M., & Vanmarcke, E. (2012). Physically based assessment of hurricane surge threat under climate change. *Nature Climate Change*, *2*(6), 462.

Lin, N., Kopp, R. E., Horton, B. P., & Donnelly, J. P. (2016). Hurricane Sandy's flood frequency increasing from year 1800 to 2100. *Proceedings of the National Academy of Sciences*, *113*(43), 12071-12075.

Lin, N., Smith, J. A., Villarini, G., Marchok, T. P., & Baeck, M. L. (2010). Modeling extreme rainfall, winds, and surge from Hurricane Isabel (2003). *Weather and Forecasting*, *25*(5), 1342-1361.

Liu, Y., Zhang, D. L., & Yau, M. K. (1997). A multiscale numerical study of Hurricane Andrew (1992). Part I: Explicit simulation and verification. *Monthly Weather Review*, *125*(12), 3073-3093.

Lowe, J. A., Gregory, J. M., & Flather, R. A. (2001). Changes in the occurrence of storm surges around the United Kingdom under a future climate scenario using a dynamic storm surge model driven by the Hadley Centre climate models. *Climate dynamics*, *18*(3-4), 179-188.

Lowe, J. A., & Gregory, J. M. (2005). The effects of climate change on storm surges around the United Kingdom. *Philosophical Transactions of the Royal Society of London A: Mathematical, Physical and Engineering Sciences*, *363*(1831), 1313-1328.

Luettich, R., Jr., J. Westerink, and N. W. Scheffner, 1992: ADCIRC: An advanced three-dimensional circulation model for shelves, coasts, and estuaries. Report 1. Theory and methodology of ADCIRC-2DDI and ADCIRC-3DL, Tech. Rep. DRP-92-6, U.S. Army Corps of Engineers, 137 pp.

Ma, Z., Han, G., & Young, B. (2015). Oceanic responses to Hurricane Igor over the Grand Banks: A modeling study. *Journal of Geophysical Research: Oceans*, *120*(2), 1276-1295.

MacKinnon, J. A., & Gregg, M. C. (2005). Near-inertial waves on the New England shelf: The role of evolving stratification, turbulent dissipation, and bottom drag. *Journal of physical oceanography*, *35*(12), 2408-2424.

Malkus, J. S., & Riehl, H. (1960). On the dynamics and energy transformations in steady-state hurricanes. *Tellus*, *12*(1), 1-20.

Mellor, G. L. (2001). One-dimensional, ocean surface layer modeling: a problem and a solution. *Journal of Physical Oceanography*, *31*(3), 790-809.

Mellor, G. L., & Yamada, T. (1982). Development of a turbulence closure model for geophysical fluid problems. *Reviews of Geophysics*, *20*(4), 851-875.

Miles, T., Glenn, S. M., & Schofield, O. (2013). Temporal and spatial variability in fall storm induced sediment resuspension on the Mid-Atlantic Bight. *Continental Shelf Research*, *63*, S36-S49.

Miles, T., Seroka, G., & Glenn, S. (2017). Coastal ocean circulation during Hurricane

Sandy. *Journal of Geophysical Research: Oceans*, *122*(9), 7095-7114.

Miles, T., Seroka, G., Kohut, J., Schofield, O., & Glenn, S. (2015). Glider observations and modeling of sediment transport in Hurricane Sandy. *Journal of Geophysical Research: Oceans*, *120*(3), 1771-1791.

Miller, K. G., Kopp, R. E., Horton, B. P., Browning, J. V., & Kemp, A. C. (2013). A geological perspective on sea-level rise and its impacts along the US mid-Atlantic coast. *Earth's Future*, *1*(1), 3-18.

Millot, C., & Crépon, M. (1981). Inertial oscillations on the continental shelf of the Gulf of Lions-Observations and theory. *Journal of Physical Oceanography*, *11*(5), 639-657.

Molinari, J., & Dudek, M. (1992). Parameterization of convective precipitation in mesoscale numerical models: A critical review. *Monthly Weather Review*, *120*(2), 326-344.

Mooers, C. N. (1975). Several effects of a baroclinic current on the cross-stream propagation of inertial-internal waves. *Geophysical and Astrophysical Fluid Dynamics*, *6*(3), 245-275.

Mousavi, M. E., Irish, J. L., Frey, A. E., Olivera, F., & Edge, B. L. (2011). Global warming and hurricanes: the potential impact of hurricane intensification and sea level rise on coastal flooding. *Climatic Change*, *104*(3-4), 575-597.

Nolan, D. S., Zhang, J. A., & Stern, D. P. (2009a). Evaluation of planetary boundary layer parameterizations in tropical cyclones by comparison of in situ observations and high-resolution simulations of Hurricane Isabel (2003). Part I: Initialization, maximum winds, and the outer-core boundary layer. *Monthly Weather Review*, *137*(11), 3651-

3674.

Nolan, D. S., Zhang, J. A., & Stern, D. P. (2009b). Evaluation of planetary boundary layer parameterizations in tropical cyclones by comparison of in situ observations and high-resolution simulations of Hurricane Isabel (2003). Part I: Initialization, maximum winds, and the outer-core boundary layer. *Monthly Weather Review*, *137*(11), 3651-3674.

Peng, M., Xie, L., & Pietrafesa, L. J. (2004). A numerical study of storm surge and inundation in the Croatan–Albemarle–Pamlico Estuary System. *Estuarine, Coastal and Shelf Science*, *59*(1), 121-137.

Penny, A. B., Harr, P. A., & Doyle, J. D. (2016). Sensitivity to the representation of microphysical processes in numerical simulations during tropical storm formation. *Monthly Weather Review*, *144*(10), 3611-3630.

Pettigrew, N. R. (1981), T*he dynamics and kinematics of the coastal boundary layer off Long Island*, (Ph.D. thesis). Woods Hole, MA: Woods Hole Oceanography Institution.

Pleim, J. E. (2006). A simple, efficient solution of flux–profile relationships in the atmospheric surface layer. *Journal of Applied Meteorology and Climatology*, *45*(2), 341-347.

Pleim, J. E. (2007). A combined local and nonlocal closure model for the atmospheric boundary layer. Part I: Model description and testing. *Journal of Applied Meteorology and Climatology*, *46*(9), 1383-1395.

Pollard, R. T. (1980). Properties of near-surface inertial oscillations. *Journal of Physical Oceanography*, *10*(3), 385-398.

Pollard, R. T., & Millard, R. C. (1970). Comparison between observed and simulated wind-

generated inertial oscillations. *Deep Sea Research, 17*(4), 153-175.

Powell, M. D., Houston, S. H., Amat, L. R., & Morisseau-Leroy, N. (1998). The HRD real-time hurricane wind analysis system. *Journal of Wind Engineering and Industrial Aerodynamics, 77*, 53-64.

Pore, N. A. (1965). Chesapeake Bay extratropical storm surges. *Chesapeake Science, 6*(3), 172-182.

Price, J. F. (1981). Upper ocean response to a hurricane. *Journal of Physical Oceanography, 11*(2), 153-175.

Price, J. F. (1983). Internal wave wake of a moving storm. Part I. Scales, energy budget and observations. *Journal of Physical Oceanography, 13*(6), 949-965.

Price, J. F., Sanford, T. B., & Forristall, G. Z. (1994). Forced stage response to a moving hurricane. *Journal of Physical Oceanography, 24*(2), 233-260.

Rahmstorf, S. (2012). Sea-level rise: towards understanding local vulnerability. *Environmental Research Letters, 7*(2), 021001.

Rahmstorf, S., Box, J. E., Feulner, G., Mann, M. E., Robinson, A., Rutherford, S., & Schaffernicht, E. J. (2015). Exceptional twentieth-century slowdown in Atlantic Ocean overturning circulation. *Nature Climate Change, 5*(5), 475-480.

Reed, A. J., Mann, M. E., Emanuel, K. A., Lin, N., Horton, B. P., Kemp, A. C., & Donnelly, J. P. (2015). Increased threat of tropical cyclones and coastal flooding to New York City during the anthropogenic era. *Proceedings of the National Academy of Sciences, 112*(41), 12610-12615.

Rego, J. L., & Li, C. (2009). On the importance of the forward speed of hurricanes in storm surge forecasting: A numerical study. *Geophysical Research Letters, 36*(7).

Roarty, H., Glenn, S., Kohut, J., Gong, D., Handel, E., Rivera, E., ... & Muglia, M. (2010). Operation and application of a regional high-frequency radar network in the Mid-Atlantic Bight. *Marine Technology Society Journal*, *44*(6), 133-145.

Sanford, T. B., Price, J. F., & Girton, J. B. (2011). Upper-ocean response to Hurricane Frances (2004) observed by profiling EM-APEX floats. *Journal of Physical Oceanography*, *41*(6), 1041-1056.

Sanford, T. B., Price, J. F., Girton, J. B., & Webb, D. C. (2007). Highly resolved observations and simulations of the ocean response to a hurricane. *Geophysical Research Letters*, *34*(13).

Scheffner, N. W., and P. J. Fitzpatrick, 1997: Real-time predictions of surge propagation. In *Estuarine and Coastal Modeling,* M. L. Spaulding, and A. F. Blumberg, ED., American Society of Civil Engineer, 374-388.

Schulte, D. M., Dridge, K. M., & Hudgins, M. H. (2015). Climate Change and the Evolution and Fate of the Tangier Islands of Chesapeake Bay, USA. *Scientific Reports*, *5*, 17890.

Seroka, G., Miles, T., Xu, Y., Kohut, J., Schofield, O., & Glenn, S. (2016). Hurricane Irene Sensitivity to Stratified Coastal Ocean Cooling. *Monthly Weather Review*, *144*(9), 3507-3530.

Seroka, G., Miles, T., Xu, Y., Kohut, J., Schofield, O., & Glenn, S. (2017). Rapid shelf-wide cooling response of a stratified coastal ocean to hurricanes. *Journal of Geophysical Research: Oceans*, *122*(6), 4845-4867.

Shay, L. K., & Elsberry, R. L. (1987). Near-inertial ocean current response to Hurricane Frederic. *Journal of Physical Oceanography*, *17*(8), 1249-1269.

Shay, L. K., Elsberry, R. L., & Black, P. G. (1989). Vertical structure of the ocean current response to a hurricane. *Journal of Physical Oceanography*, *19*(5), 649-669.

Shay, L. K., Mariano, A. J., Jacob, S. D., & Ryan, E. H. (1998). Mean and near-inertial ocean current response to Hurricane Gilbert. *Journal of Physical Oceanography*, *28*(5), 858-889.

Shearman, R. K. (2005). Observations of near-inertial current variability on the New England shelf. *Journal of Geophysical Research: Oceans*, *110*(C2).

Shen, J., Wang, H., Sisson, M., & Gong, W. (2006). Storm tide simulation in the Chesapeake Bay using an unstructured grid model. *Estuarine, Coastal and Shelf Science*, *68*(1-2), 1-16.

Skamarock, W. C., Klemp, J., Dudhia, J., Gill, D. O., Barker, D., Duda, M. G., ... & Powers, J. G. (2008). A Description of the Advanced Research WRF Version 3. NCAR Technical Note NCAR/TN-475+ STR.

Smith, R. K. (2000). The role of cumulus convection in hurricanes and its representation in hurricane models. *Reviews of Geophysics*, *38*(4), 465-489.

Smith, J. M., Cialone, M. A., Wamsley, T. V., & McAlpin, T. O. (2010). Potential impact of sea level rise on coastal surges in southeast Louisiana. *Ocean Engineering*, *37*(1), 37-47.

Staneva, J., Wahle, K., Koch, W., Behrens, A., Fenoglio-Marc, L., & Stanev, E. V. (2016). Coastal flooding: impact of waves on storm surge during extremes-a case study for the German Bight. *Natural Hazards and Earth System Sciences*, *16*(11), 2373.

Taylor, K. E. (2001). Summarizing multiple aspects of model performance in a single diagram. *Journal of Geophysical Research: Atmospheres*, *106*(D7), 7183-7192.

Teague, C. C. (1971). *High Frequency Resonant Scattering Techniques for the Observation of Directional Ocean Wave Spectra*, Department of Electrical Engineering, Stanford University.

Tebaldi, C., Strauss, B. H., & Zervas, C. E. (2012). Modelling sea level rise impacts on storm surges along US coasts. *Environmental Research Letters*, *7*(1), 014032.

Thompson, G., Field, P. R., Rasmussen, R. M., & Hall, W. D. (2008). Explicit forecasts of winter precipitation using an improved bulk microphysics scheme. Part II: Implementation of a new snow parameterization. *Monthly Weather Review*, *136*(12), 5095-5115.

Villarini, G., & Vecchi, G. A. (2012). Twenty-first-century projections of North Atlantic tropical storms from CMIP5 models. *Nature Climate Change*, *2*(8), 604-607.

Villarini, G., & Vecchi, G. A. (2013). Multiseason lead forecast of the North Atlantic power dissipation index (PDI) and accumulated cyclone energy (ACE). *Journal of Climate*, *26*(11), 3631-3643.

Wang, H. V., Loftis, J. D., Liu, Z., Forrest, D., & Zhang, J. (2014). The storm surge and sub-grid inundation modeling in New York City during Hurricane Sandy. *Journal of Marine Science and Engineering*, *2*(1), 226-246.

Warner, J. C., Sherwood, C. R., Arango, H. G., & Signell, R. P. (2005). Performance of four turbulence closure models implemented using a generic length scale method. *Ocean Modelling*, *8*(1), 81-113.

Weisberg, R. H., & Zheng, L. (2006). Hurricane storm surge simulations for Tampa Bay. *Estuaries and Coasts*, *29*(6), 899-913.

Weisman, M. L., Skamarock, W. C., & Klemp, J. B. (1997). The resolution dependence of

explicitly modeled convective systems. *Monthly Weather Review*, *125*(4), 527-548.

Woodruff, J. D., Irish, J. L., & Camargo, S. J. (2013). Coastal flooding by tropical cyclones and sea-level rise. *Nature*, *504*(7478), 44-52.

Xu, J. P., Wright, L. D., & Boon, J. D. (1994). Estimation of bottom stress and roughness in Lower Chesapeake Bay by the inertial dissipation method. *Journal of Coastal Research*, 329-338.

Yin, J., & Goddard, P. B. (2013). Oceanic control of sea level rise patterns along the East Coast of the United States. *Geophysical Research Letters*, *40*(20), 5514-5520.

Yin, J., S. M. Griffies, & R. J. Stouffer (2010), Spatial variability of sea level rise in twenty-first century projections, *Journal of Climate*, *23*(17), 4585–4607.

Zambon, J. B., He, R., & Warner, J. C. (2014). Tropical to extratropical: Marine environmental changes associated with Superstorm Sandy prior to its landfall. *Geophysical Research Letters*, *41*(24), 8935-8943.

Zhai, X., Greatbatch, R. J., Eden, C., & Hibiya, T. (2009). On the loss of wind-induced near-inertial energy to turbulent mixing in the upper ocean. *Journal of Physical Oceanography*, *39*(11), 3040-3045.

Zhang, D.-L., & Anthes, R. A. (1982). A high-resolution model of the planetary boundary layer—Sensitivity tests and comparisons with SESAME-79 data. *Journal of Applied Meteorology*, *21*(11), 1594-1609.

Zhang, Y., & Baptista, A. M. (2008). SELFE: a semi-implicit Eulerian–Lagrangian finite-element model for cross-scale ocean circulation. *Ocean Modelling*, *21*(3-4), 71-96.

Zhang, D.-L., Hsie, E. Y., & Moncrieff, M. W. (1988). A comparison of explicit and implicit predictions of convective and stratiform precipitating weather systems with a

meso-β-scale numerical model. *Quarterly Journal of the Royal Meteorological Society*, *114*(479), 31-60.

Zhang, F., Li, M., Ross, A. C., Lee, S. B., & Zhang, D.-L. (2017). Sensitivity Analysis of Hurricane Arthur (2014) Storm Surge Forecasts to WRF Physics Parameterizations and Model Configurations. *Weather and Forecasting*, *32*(5), 1745-1764.

Zhang, J. A., & Marks, F. D. (2015). Effects of horizontal diffusion on tropical cyclone intensity change and structure in idealized three-dimensional numerical simulations. *Monthly Weather Review*, *143*(10), 3981-3995.

Zhang, J. A., Nolan, D. S., Rogers, R. F., & Tallapragada, V. (2015). Evaluating the impact of improvements in the boundary layer parameterization on hurricane intensity and structure forecasts in HWRF. *Monthly Weather Review*, *143*(8), 3136-3155.

Zhang, D.-L., & Zheng, W. Z. (2004). Diurnal cycles of surface winds and temperatures as simulated by five boundary layer parameterizations. *Journal of Applied Meteorology*, *43*(1), 157-169.

Zhong, L., & Li, M. (2006). Tidal energy fluxes and dissipation in the Chesapeake Bay. *Continental Shelf Research*, *26*(6), 752-770.

Zhong, L., Li, M., & Zhang, D. L. (2010). How do uncertainties in hurricane model forecasts affect storm surge predictions in a semi-enclosed bay? *Estuarine, Coastal and Shelf Science*, *90*(2), 61-72.

Zhu, P., Menelaou, K., & Zhu, Z. (2014). Impact of subgrid-scale vertical turbulent mixing on eyewall asymmetric structures and mesovortices of hurricanes. *Quarterly Journal of the Royal Meteorological Society*, *140*(679), 416-438.

Zhu, T., & Zhang, D.-L. (2006). Numerical simulation of Hurricane Bonnie (1998). Part

II: Sensitivity to varying cloud microphysical processes. *Journal of the Atmospheric Sciences*, *63*(1), 109-126.

Zhu, T., & Zhang, D.-L. (2006). The impact of the storm-induced SST cooling on hurricane intensity. *Advances in Atmospheric Sciences*, *23*(1), 14-22.

Zhu, Z., & Zhu, P. (2015). Sensitivities of eyewall replacement cycle to model physics, vortex structure, and background winds in numerical simulations of tropical cyclones. *Journal of Geophysical Research: Atmospheres*, *120*(2), 590-622.

Zou, Q. P., Chen, Y., Cluckie, I., Hewston, R., Pan, S., Peng, Z., & Reeve, D. (2013). Ensemble prediction of coastal flood risk arising from overtopping by linking meteorological, ocean, coastal and surf zone models. *Quarterly Journal of the Royal Meteorological Society*, *139*(671), 298-313.